

THE ROLE OF THE Y-COMPONENT OF THE INTERPLANETARY MAGNETIC FIELD
IN TRANSPOLAR SATURATION AND RING CURRENT RESPONSE
AS FOUND IN DATA AND SIMULATION

by

ELIZABETH JOY MITCHELL

Presented to the Faculty of the Graduate School of
The University of Texas at Arlington in Partial Fulfillment
of the Requirements
for the Degree of

DOCTOR OF PHILOSOPHY

THE UNIVERSITY OF TEXAS AT ARLINGTON
May 2010

Copyright © by Elizabeth Mitchell 2010

All Rights Reserved

ACKNOWLEDGEMENTS

Funding for my research has been provided by NASA grants NNX09AI63G (GSRP) and 4200254162ESAX22008D, NSF grant ATM-0900920 and ATM-0120950 (CISM).

With heart-felt gratitude, I thank my advisor, Dr. Ramon Lopez. Since I was an undergraduate at the University of Texas at El Paso, his encouragement and sincerity have guided me through many struggles. Thank you, Ray, for seeing the scientist in me before I could and for encouraging me to do all things well. Thank you also for speaking directly and not allowing my fears to color your answers. Many are the lessons I have learned in group management as well as space science under your direction.

I thank my committee: Dr. Ramon Lopez, Dr. Yue Deng, Dr. Zdzislaw Musielak, Dr. Manfred Cuntz, and Dr. Ali Koymen. I have enjoyed the privilege of sharing my research with you all. I am encouraged by your words of praise and constructive criticism. I thank you for helping prepare me as a scientist. I look forward to defending my work before you and answering your questions.

I thank all of my lab mates and undergraduates through the years of graduate school. I would not be the scientist and person I am today without their shaping influences. I especially thank Ximena Cid and Robert Bruntz, you both have been rocks in my life.

Finally, I thank my father, Stuart Mitchell. As Ray was my advisor in research and academics, so you have been my advisor in life. Dad, I could not have written this without you. I only wish you could be here to see me defend and add your questions to the mix. Thank you for preparing me for life.

April 19, 2010

ABSTRACT

THE ROLE OF THE Y-COMPONENT OF THE INTERPLANETARY MAGNETIC FIELD IN TRANSPOLAR SATURATION AND RING CURRENT RESPONSE AS FOUND IN DATA AND SIMULATION

Elizabeth Joy Mitchell, PhD

The University of Texas at Arlington, 2010

Supervising Professor: Ramon E. Lopez

Energy is transferred into the magnetosphere of Earth through merging of magnetic fields (Dungey cycle and lobe cell convection) and through momentum transfer across the magnetopause (viscous interactions). These processes cause enhanced plasma convection in the inner magnetosphere and ionosphere, which in turn form the ring current and the transpolar potential, respectively. These processes have been studied extensively with regard to the role of the north-south component of the interplanetary magnetic field (IMF). The role of the dawn-dusk IMF is less well known.

We use the LFM global MHD simulation, the CRCM, and data to quantify the transpolar potential and ring current responses to the dawn-dusk IMF (B_y). As with the north-south IMF (B_z), we find the transpolar potential saturates for large values of B_y . Furthermore, the transpolar potential saturates at approximately the same magnitude of the magnetic field, but with a much smaller transpolar potential value. This suggests the saturation of the transpolar potential depends on the balance of the forces in the magnetosheath rather than the region 1

current. Unlike with B_z , we find the ring current does not respond to changes in B_y . This indicates a decoupling of the plasma convection in the ionosphere from convection in the inner magnetosphere. We discuss the implications of these results for space physics.

TABLE OF CONTENTS

ACKNOWLEDGEMENTS	iii
ABSTRACT	iv
LIST OF ILLUSTRATIONS.....	ix
LIST OF TABLES	xii
Chapter	Page
1. INTRODUCTION.....	1
1.1 The Sun-Earth System.....	1
1.1.1 Properties of the Solar Wind	2
1.1.1.1 Interplanetary Magnetic Field.....	3
1.1.2 The Bow Shock and Magnetosheath	5
1.1.3 The Magnetosphere	6
1.1.3.1 Ring Current.....	9
1.1.4 The Ionosphere	12
1.1.4.1 Polar Cap	13
1.1.4.2 Auroral Oval	14
1.2 Methods of Generating Magnetospheric and Ionospheric Convection	14
1.2.1 Viscous Interactions	14
1.2.2 Dungey Cycle.....	15
1.2.3 Lobe Cell Convection	17
1.3 Theories of Transpolar Saturation	18
1.3.1 Region 1 Current Theory.....	19
1.3.2 Alfvén Wing Theory.....	19

1.3.3 Magnetosheath Force Balance Theory	20
1.4 Outline for Dissertation.....	21
2. SIMULATIONS	23
2.1 Ideal MHD Equations	23
2.2 The Lyon-Fedder-Mobarry Global Magneto-Hydro-Dynamic Simulation	25
2.2.1 An Overview of the LFM.....	25
2.2.2 Six Considerations of Modelers in Creating LFM	26
2.2.2.1 Resolution of Features	26
2.2.2.2 $\nabla \cdot \mathbf{B} = 0$	27
2.2.2.3 Time Step	28
2.2.2.4 Truncation Errors	29
2.2.2.5 Ionosphere	29
2.2.3 Modifications of Ideal MHD Equations	30
2.2.4 Boundary Conditions.....	31
2.2.5 Format of Input and Output of Simulation	32
2.2.6 Method of Visualization of Simulation Results	33
2.3 The Comprehensive Ring Current Model	33
2.3.1 An Overview of CRCM.....	33
2.3.2 Coupling of the LFM and CRCM	35
3. OBSERVATION-BASED DATA	37
3.1 Solar Wind Data	37
3.2 DMSP Data	38
3.3 AMIE Data	39
3.4 Ground-based Magnetometer Data	40
3.5 Pressure Correction	41
3.6 Ring Current Injection Rate.....	41

4. RESULTS AND DISCUSSION.....	44
4.1 Saturation of the Transpolar Potential	44
4.1.1 Simulated Response to Large B_z	45
4.1.2 Simulated Response to Large B_y	47
4.1.3 Observational Estimates of the Potential During Periods of Large B_y	50
4.1.4 Discussion.....	54
4.1.5 Conclusions about Transpolar Potential Saturation.....	61
4.2 Lack of Ring Current Response	61
4.2.1 Observational Estimates of Ring Current Injection Rate During Periods of Large B_z	61
4.2.2 Simulated Ring Current Response to Large B_z	63
4.2.3 Observational Estimates of Ring Current Injection Rate During Periods of Large B_y	67
4.2.4 Simulated Ring Current Response to Large B_y	68
4.2.5 Three Case Studies	69
4.2.6 Discussion.....	74
4.2.7 Conclusions about the Lack of Ring Current Response	75
5. CONCLUSIONS AND FUTURE WORK	77
APPENDIX	
A. LIST OF EVENTS FOR LARGE B_y AND B_z	80
REFERENCES.....	85
BIOGRAPHICAL INFORMATION	91

LIST OF ILLUSTRATIONS

Figure	Page
1. Diagram of the Geocentric Solar Ecliptic coordinate system (red), Geocentric Solar Magnetospheric coordinate system (maroon), and the Solar Magnetic coordinate system (pink). The rotational axis of Earth is black and the magnetic dipole is blue. Not to scale.	1
2. Illustration of <i>Frozen-in</i> flux from C.J. Owen's Lecture Notes. (http://www.mssl.ucl.ac.uk/~cjo/STMP/Lecture_16_18/MHD_Section_Figure1.jpg)	4
3. Parker Spiral for 400 km/s and 2000 km/s at the orbits of Earth and Mars. Provided by NASA through http://commons.wikimedia.org/wiki/File:Parker_spiral.png	4
4. Cartoon of Magnetosphere currents. From public domain at http://en.wikipedia.org/wiki/File:Currents.jpg	8
5. Three motions executed by particles in the inner magnetosphere. (http://www-ssc.igpp.ucla.edu/personnel/russell/papers/magsphere/msphere07.gif)	8
6. The typical location of the auroral latitudes. Image has a GNU Free Documentation License by Eric Donovan and is found at http://commons.wikimedia.org/wiki/Aurora	13
7. The northern and southern magnetotail lobes for southward IMF ((A) looking from the Sun and (B) looking from the dusk side of Earth) and for downward IMF ((C) looking from the Sun and (D) looking from the dusk side of Earth) created from LFM runs of $u_x = -400$ km/s, $n = 5 \text{ cm}^{-3}$, and $ B = 5 \text{ nT}$ in CISM-DX.	16
8. Contours (blue and red) of northern polar cap potential for LFM run of $u_x = -400$ km/s, $n = 5 \text{ cm}^{-3}$, and $B_y = -20 \text{ nT}$. The open-closed boundary (thick black line) is hypothetical, and placed to show how closed convection can be within the open field line region. The noon is at the top of the picture.	17
9. Equatorial plane for LFM simulation run with a density of 5 cm-3. The bow shock and magnetosheath are visible as the high density region. The red line marks the $B_z = 0$ contour.	25
10. The equatorial and cross-sectional planes of the LFM simulation grid. The grid is a cylinder with higher density of cells near the Earth.	27
11. LFM simulated transpolar potential versus IEF (for exclusively southward IMF) for 5.0 mho conductivity. The dash line is an extrapolation of the linear regression calculated between 0.4 and 1.6 mV/m.	45

12. Panel A is LFM simulated transpolar potential versus IEF (for exclusively dawn-dusk IMF) for 5.0, 10.0, and 20.0 mho conductivities. The three broken lines are extrapolations of the linear regressions calculated for each run between 0.8 and 2.0 mV/m. Panel B is the difference between the prediction from the linear fit and the actual LFM simulated transpolar potential versus IEF (for exclusively dawn-dusk IMF) for 5.0, 10.0, and 20.0 mho conductivities.....	47
13. Three SuperDARN convection maps with DMSP satellite passes superimposed. The maximum (+) and minimum (-) polar cap potentials are marked on each map. Panel A is the SuperDARN convection map for September 1, 2003, between 1520 and 1522. It has an F-13 pass superimposed, with its position between 1520 and 1522 marked in yellow. Panel B is the SuperDARN convection map for May 2, 2000, between 1450 and 1452. It has an F-13 and an F-15 pass superimposed, with each satellite position between 1450 and 1452 marked in yellow. Panel C is the SuperDARN convection map for December 20, 2003, between 1630 and 1632. It has an F-13 and an F-15 pass superimposed, with each satellite position between 1630 and 1632 marked in yellow.	51
14. Maximum AMIE transpolar potential (diamonds) for each 1 mV/m bin versus 1 mV/m bins of B_y -dominant transverse IEF and DMSP transpolar potentials (dashes) versus B_y -dominant transverse IEF.....	53
15. LFM simulated β for 5.0 mho conductivity mapped to a plane tilted 45 degrees from the North Pole toward dusk and perpendicular to the expected merging line. The scale is from 0 to 1; gray indicates β greater than 1. Panel A has solar wind $B_y = -7.5$ nT and IEF = 3.0 mV/m. Panel B has solar wind $B_y = -10.0$ nT and IEF = 4.0 mV/m. Panel C has solar wind $B_y = -12.5$ nT and IEF = 5.0 mV/m.....	55
16. LFM simulated β for 20 mho conductivity mapped to a plane tilted 45 degrees from the North Pole toward dusk and perpendicular to the expected merging line. The scale is from 0 to 1; gray indicates β greater than 1. Panel A has solar wind $B_y = -7.5$ nT and IEF = 3.0 mV/m. Panel B has solar wind $B_y = -10.0$ nT and IEF = 4.0 mV/m. Panel C has solar wind $B_y = -12.5$ nT and IEF = 5.0 mV/m.	56
17. LFM simulated transpolar potential versus exclusively B_y -dominant IEF for 5.0 mho conductivity and solar wind $u_x = -400.0$ km/s and -800.0 km/s. The broken lines are extrapolations of the linear regression calculated between 0.4 and 1.6 mV/m for $u_x = -400.0$ km/s and between 3.2 and 8.0 mV/m for $u_x = -800.0$ km/s.	59
18. LFM simulated β for 5.0 mho conductivity and solar wind $u_x = -800.0$ km/s mapped to a plane tilted 45 degrees from the North Pole toward dusk and perpendicular to the expected merging line. The scale is from 0 to 1; gray indicates β greater than 1. Panel A has solar wind $B_y = -15.0$ nT and IEF = 12.0 mV/m. Panel B has solar wind $B_y = -17.5$ nT and IEF = 14.0 mV/m. Panel C has solar wind $B_y = -20.0$ nT and	

IEF = 16.0 mV/m.	60
19. The RCIR for periods of B_z -dominant IMF versus the IEF E_y . The least-square fit is plotted in the dashed line with the equation in the bottom right hand corner of the plot.	62
20. CRCM simulated RCIR versus IEF E_y for exclusively southward B_z LFM simulations. The least-square fit is plotted in the dashed line with the equation in the bottom right hand corner of the plot.	64
21. Solar Wind data, Sym-H*, and AMIE transpolar potential on March 20, 2001	65
22 Idealized Solar Wind used as LFM input, CRCM simulated Sym-H, and simulated Transpolar Potential for $B_z=-20$ nT	66
23. The RCIR for periods of B_y -dominant IMF versus the IEF $ E_z $. The least-square fit is plotted in the dashed line with the equation in the bottom right hand corner of the plot.	67
24. CRCM simulated RCIR versus IEF $ E_z $ for exclusively dawn-dusk IMF LFM simulations. The least-square fit is plotted in the dashed line with the equation in the bottom right hand corner of the plot	68
25. Solar wind data, Sym-H*, and AMIE transpolar potential on August 1-2, 2002.....	71
26. Solar wind data, Sym-H*, and AMIE transpolar potential on October 21-22, 1999	72
27. Idealized Solar Wind used as LFM input, CRCM simulated Sym-H, and simulated Transpolar Potential for $B_y=-17.5$ nT	73

LIST OF TABLES

Table	Page
1. Measurements by DMSP satellites during selected intervals of B_y -dominant IMF. Average AMIE, B_y , and $ E_t $ for the same selected intervals.	52
2. Date, Start Time, and End Time of Large B_y Events in 1999 and 2000.	81
3. Date, Start Time, and End Time of Large B_y Events in 2001 and First Half of 2002.	82
4. Date, Start Time, and End Time for Large B_y Events in Second Half of 2002 and 2003.....	83
5. Date, Start Time, and End Time for Large B_z Events for 1999 to 2003..	84

CHAPTER 1

INTRODUCTION

1.1 The Sun-Earth System

Space plasma physics is the study of the interactions of space plasmas and magnetized bodies. One concentration of space plasma physics is the interactions between the magnetized plasma flowing from the Sun (the solar wind) and the region in which the magnetic field of the Earth is the dominant magnetic field (Earth's magnetosphere). This work examines the interactions of the dawn-dusk component of the interplanetary magnetic field (IMF) with the magnetic field and ionosphere of Earth in terms of the effect on the ionospheric transpolar potential as well as the effect on the injection of energy into the ring current.

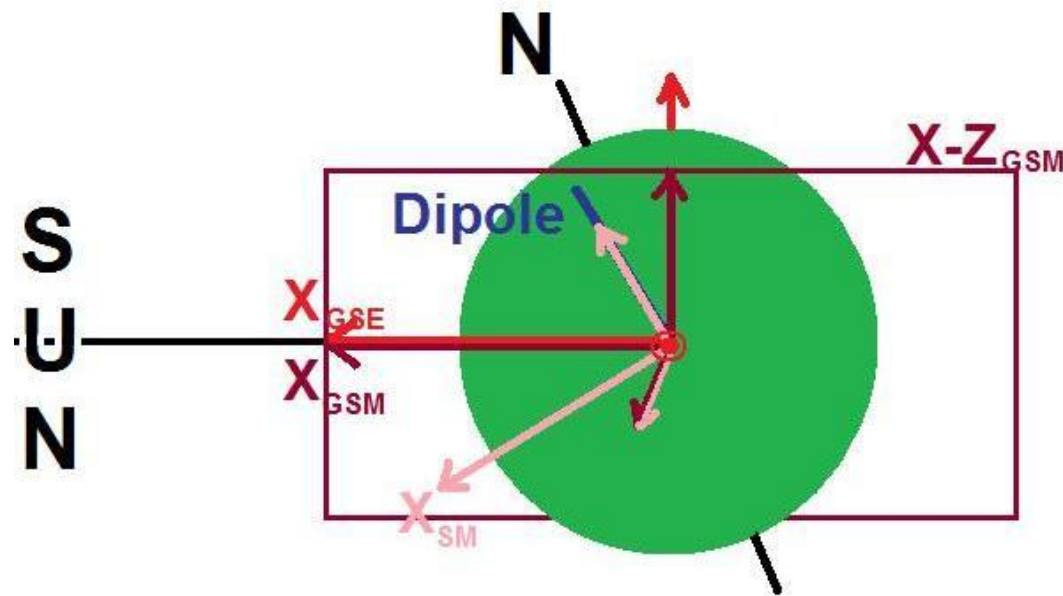


Figure 1. Diagram of the Geocentric Solar Ecliptic coordinate system (red), Geocentric Solar Magnetospheric coordinate system (maroon), and the Solar Magnetic coordinate system (pink). The rotational axis of Earth is black and the magnetic dipole is blue. Not to scale.

Three coordinate systems are used throughout this work. Figure 1 illustrates the axes of the coordinate systems in relation to the Sun, Earth, and magnetic dipole. The x-axis of the Geocentric Solar Ecliptic (GSE) coordinate system points from the Earth to the Sun (this is also known as the Sun-Earth line). The GSE system is illustrated in Figure 1 in red. The y-axis of the GSE lies in the ecliptic plane pointing toward dusk. The z-axis of the GSE completes the right hand rule and is parallel to the ecliptic pole. The Geocentric Solar Magnetospheric (GSM) coordinate system can be calculated by rotating the GSE system about its x-axis. The GSM system is illustrated in Figure 1 in maroon. The x-axis is the same in GSE and GSM. The y-axis of the GSM is perpendicular to the magnetic dipole of the Earth and points toward dusk. This convention makes the x-z plane of the GSM contain the magnetic dipole of the Earth with the z-axis completing the right hand rule. The Solar Magnetic (SM) coordinate system can be calculated by rotating the GSM system about its y-axis. The SM system is illustrated in Figure 1 in pink. The y-axis is the same in GSM and SM. The z-axis of the SM is parallel to the north magnetic dipole. The x-axis of the SM completes the right hand rule, and does not point directly to the Sun. It should be noted that when there is no dipole tilt (as in simulations), the GSM and SM coordinates are the same. Unless otherwise noted, when the component of a vector is discussed in this work its direction will be given in GSM coordinates.

1.1.1 Properties of the Solar Wind

The upper atmosphere of the Sun is called the corona and it extends from the visible surface of the Sun (photosphere) to the heliopause (the boundary between intergalactic space and the space dominated by the sun-regulated interactions space) [Priest, 1995]. The region of space the corona occupies is sometimes referred to as the heliosphere or interplanetary space. The expanding plasma is referred to as the solar wind when the flow is supersonic.

The solar wind is quasi-neutral, fully ionized plasma which is collisionless, highly conductive, and continuously expanding outward [Hundhausen, 1995]. Hydrogen ions (H^+), Helium ions (He^{2+}), and electrons are ejected into the corona, where hydrodynamic expansion

accelerates the plasma [Hundhausen, 1995]. At 1 AU, the solar wind has a nominal (or median) speed of 450 kilometers per second (km/s) in mainly the negative X-direction (anti-sunward) [Hundhausen, 1995]. The solar wind speed (u) at 1 AU can range from 300 to 800 km/s with a few incidents of speeds exceeding 1200 km/s.

At 1 AU, the solar wind has a nominal density of 6.6 hydrogen ions per cubic centimeter (cm^{-3}) [Hundhausen, 1995]. The solar wind density (n) ranges from 0.1 to 100 cm^{-3} , though density spikes of greater than 30 cm^{-3} are unusual. Along with the hydrogen ions (90% of ion composition), the solar wind composition contains approximately 9% helium ions [Bochsler, 2000] and the electrons to make it a quasi-neutral plasma.

1.1.1.1 Interplanetary Magnetic Field

At 1 AU, the solar wind has a nominal magnetic field strength of 5 nanoTesla (nT) [Hundhausen, 1995]. The solar wind magnetic field (also known as the interplanetary magnetic field or IMF) strength ranges from almost 0 nT to 10s of nanoTesla, with larger values occurring during transient solar disruptions. The average orientation of the IMF is at a 45 degree angle to the Y-axis in the XY-plane ($-\hat{x} + \hat{y}$). While the orientation may be in any direction at a specific moment, the average orientation at 1 AU is a direct result of the radial dispersion of the solar wind and its condition of *frozen in* flux. First described by Parker [1958], the plasma flowing out of the Sun is threaded by magnetic field lines with footpoints in the Sun. Because the plasma is collisionless, low-density, and highly conductive, the magnetic field lines and the area over which their element of plasma spreads are related such that the magnetic flux through the area is constant. This is known as *frozen in* flux, see Figure 2. As the plasma continues to flow radially away from the Sun, the Sun continues to rotate, taking the footpoints of the magnetic field lines with it. Figure 3 illustrates the resulting spiral, known as the Parker spiral [Parker, 1958]. The orbit of Earth, plotted in blue at 1 AU in Figure 3, intersects the red 400 km/s spiral lines at approximately a 45 degree angle. If the solar wind speed increases, the IMF becomes more radial increasing its angle to the y-axis, as shown by the solar wind speed of 2000 km/s.

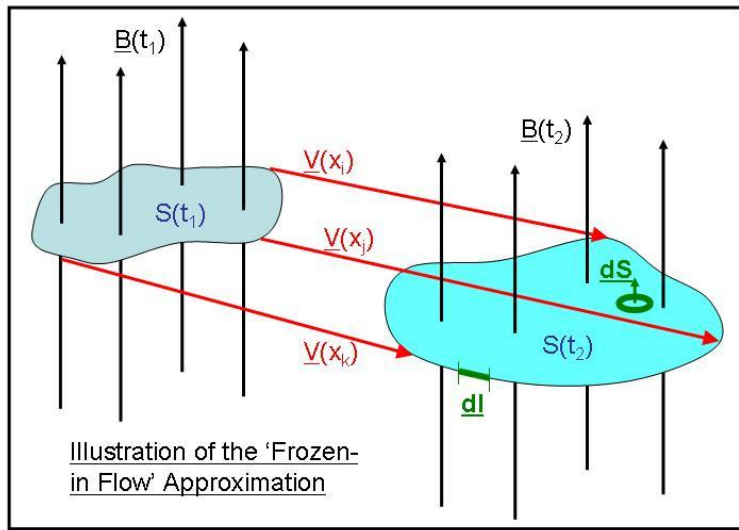


Figure 2. Illustration of *Frozen-in* flux from C.J. Owen's Lecture Notes.
[\(http://www.mssl.ucl.ac.uk/~cjo/STMP/Lecture_16_18/MHD_Section_Figure1.jpg\)](http://www.mssl.ucl.ac.uk/~cjo/STMP/Lecture_16_18/MHD_Section_Figure1.jpg)

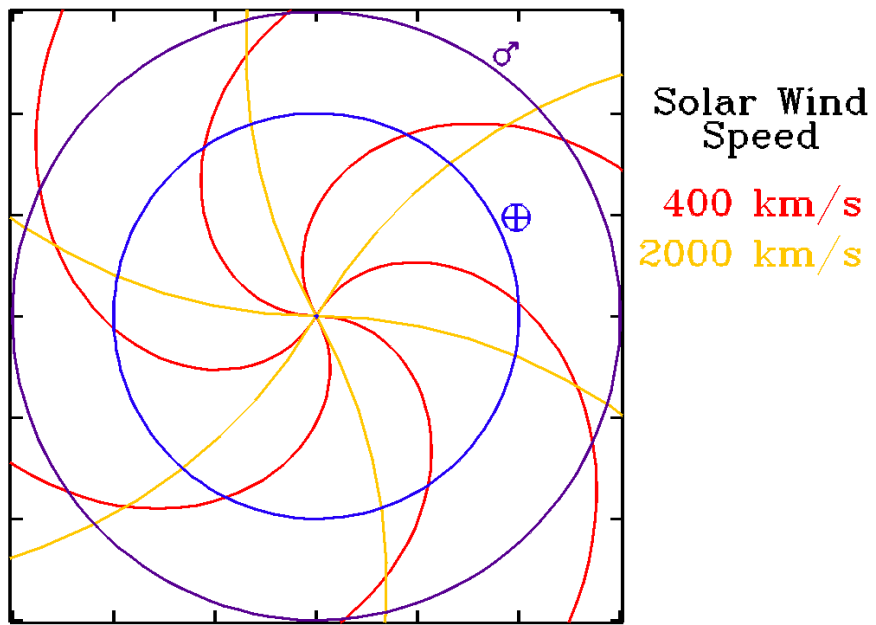


Figure 3. Parker Spiral for 400 km/s and 2000 km/s at the orbits of Earth and Mars. Provided by NASA through http://commons.wikimedia.org/wiki/File:Parker_spiral.png

1.1.2 The Bow Shock and Magnetosheath

The solar wind speed at 1 AU is typically much larger than the speed with which information can travel in collisionless plasma, which makes the solar wind flow “supersonic.” In space plasma physics, a flow is described as “supersonic” when the flow speed exceeds the speed of any of the MHD wave mode speeds; the Alfvén speed (1), sound speed (2), fast magnetosonic speed (3), and slow magnetosonic speed (not shown) [Burgess, 1995].

$$v_A = \frac{B_{sw}}{\sqrt{\mu_0 \rho_{sw}}} \quad (\text{Alfvén speed}) \quad (1)$$

$$c_s = \sqrt{\frac{\gamma p_{sw}}{\rho_{sw}}} \quad (\text{sound speed}) \quad (2)$$

$$v_{MS} = \sqrt{v_A^2 + c_s^2} \quad (\text{Fast magnetosonic speed}) \quad (3)$$

where B_{sw} is the magnitude of the IMF, ρ_{sw} is the mass density of the solar wind, μ_0 is the permeability of free space, γ is the ratio of specific heats, and p_{sw} is the plasma pressure of the solar wind. The ratio of the solar wind flow speed to any of these speeds is its corresponding Mach number, thus the ratio of the solar wind flow to the Alfvén speed is the Alfvén Mach number.

The solar wind is flowing at supersonic and superalfvénic speeds as it approaches the Earth. As with all supersonic flows, the solar wind passing Earth must slow down in order to divert around the Earth. The slowing of a supersonic flow creates a shock wave, the bow shock for Earth. The location of the bow shock is determined by the magnetosonic mach number of the solar wind. Under nominal solar wind conditions, the bow shock is located approximately 15 earth radii (R_E) in front of the Earth.

The bow shock slows, heats, and compresses the solar wind passing through it. The exact amount of slowing, heating, and compression depends on the local solar wind conditions. Then the solar wind that passes through the bow shock enters the magnetosheath. The magnetosheath is the region between the bow shock and magnetosphere. Approximately 5 R_E across at the subsolar point during nominal conditions, the shape and size of the

magnetosheath are determined by many factors including the solar wind magnetosonic mach number, the conductivity of the ionosphere, and the ram pressure of the solar wind.

The IMF is still imbedded in the magnetosheath plasma. At the inner boundary of the magnetosheath (the magnetopause), the solar wind/magnetosheath plasma and imbedded magnetic field may interact with the magnetosphere and the ionosphere. Magnetosheath-magnetosphere and magnetosphere-ionosphere interactions include the Dungey cycle (dayside merging, night side reconnection, and magnetospheric convection) and viscous interactions. Magnetosheath-ionosphere interactions also include dayside merging and night side reconnection as well as lobe cell convection. All of these interactions are discussed section 1.2.

1.1.3 *The Magnetosphere*

The magnetosphere is the region of space around the Earth where the magnetic field of the Earth is the dominant magnetic field. Bounded by the magnetopause, the magnetosphere has dimensions of $10 R_E > X > -200 R_E$, $16 R_E > Y$ (at $X=0$) $> -16 R_E$, and $15 R_E > Z$ (at $X=0$) $> -15 R_E$ for nominal solar wind conditions [Sibeck et al., 1991]. The exact location of the magnetopause is dependent upon the currents flowing in and around the magnetosphere together with the dynamic equilibrium between the solar wind ram pressure and the magnetic pressure of the magnetosphere [Walker and Russell, 1995].

A first-order approximation for the location of the magnetopause may be derived from pressure balance, ignoring the current systems. The basic premise is the total pressure is constant on either side of a boundary layer. Thus, the total solar wind pressure at the bow shock is equivalent to the total pressure of the magnetosheath at the bow shock; and, the total pressure of the magnetosheath at the magnetopause is equivalent to the total magnetospheric pressure at the magnetopause. Between the bow shock and the magnetopause the total pressure decreases slightly with the divergence of plasma flow around the magnetosphere (this idea is discussed in more detail in section 1.3.3). Therefore, the total solar wind pressure is proportional to the total magnetospheric pressure.

Solar wind pressure is almost all dynamic pressure ($\rho_{sw} u_{sw}^2$) with less than 1% magnetic and thermal pressure [Walker and Russell, 1995]. Magnetospheric pressure is approximated to be all magnetic pressure ($B^2/2\mu_0$). Using a scaling constant to indicate the diminishing pressure due to divergence in the magnetosheath, the solar wind dynamic pressure and the magnetospheric pressure are equated in equation (4).

$$K\rho_{sw} u_{sw}^2 = \frac{B^2}{2\mu_0} \quad (4)$$

where K is the scaling constant, ρ_{sw} is the mass density of the solar wind, u_{sw} is the solar wind bulk flow speed, and B is the magnetic field strength at the subsolar point of the magnetopause [Walker and Russell, 1995]. The magnetic field strength at the subsolar point depends on the compression of the dipole field by the solar wind flow, and can be rewritten in terms of a compression factor (a) and the dipole field ($B_o r_{mp}^{-3}$).

$$K\rho_{sw} u_{sw}^2 = \frac{a^2 B_o^2}{2\mu_0 r_{mp}^6} \quad (4')$$

$$r_{mp} [R_E] = \left(\frac{a^2 B_o^2}{2\mu_0 K\rho_{sw} u_{sw}^2} \right)^{1/6} \quad (\text{Chapman-Ferraro Scaling}) \quad (5)$$

where B_o is the strength of the magnetic dipole at the equator. Thus, the location of the subsolar point of the magnetopause (r_{mp}) scales as $(\rho_{sw} u_{sw}^2)^{-1/6}$, also known as the Chapman-Ferraro scaling. Under nominal conditions, Chapman-Ferraro scaling predicts the nose of the magnetopause is at $10 R_E$. When the solar wind dynamic pressure grows, the magnetosphere shrinks to remain in equilibrium. In some extreme solar wind conditions, the dayside magnetosphere has been shown to have shrunk to less than $6.6 R_E$ [e.g., Thomsen et al., 1998].

Through the magnetosheath-magnetosphere interactions at the magnetopause, energy is transferred into the magnetosphere. The energy is stored in current systems. There are numerous current systems in the magnetosphere as illustrated in Figure 4. This work focuses on the ring current.

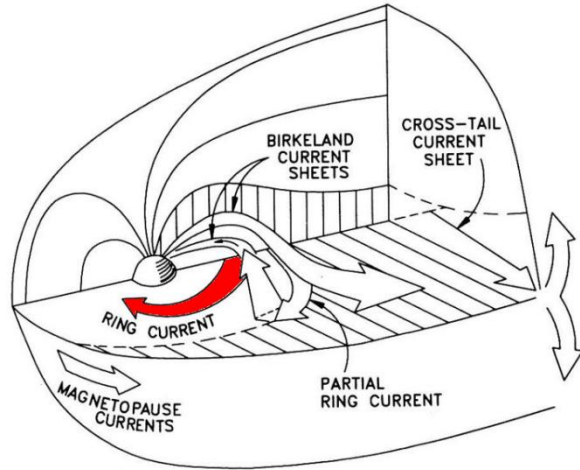


Figure 4. Cartoon of Magnetosphere currents. From public domain at
<http://en.wikipedia.org/wiki/File:Currents.jpg>.

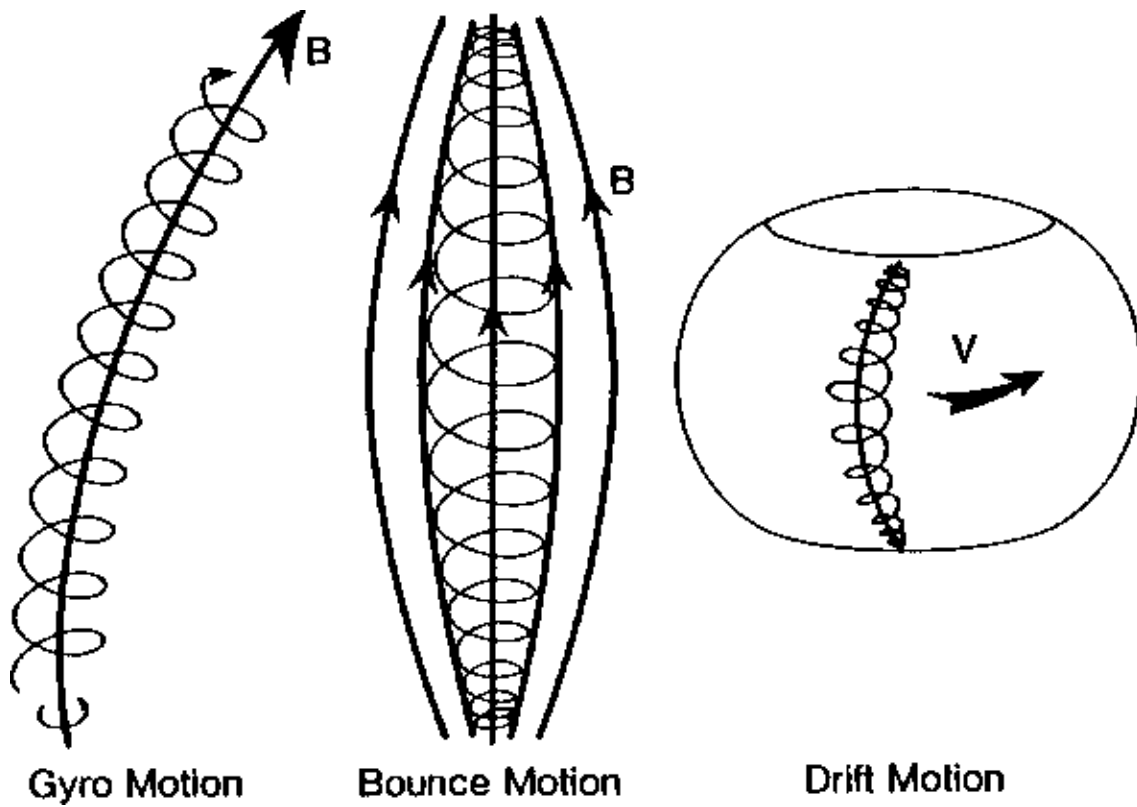


Figure 5. Three motions executed by particles in the inner magnetosphere.
<http://www-ssc.igpp.ucla.edu/personnel/russell/papers/magsphere/msphere07.gif>

1.1.3.1 Ring Current

Occupying the inner magnetosphere between 2 and 9 R_E, the ring current is a toroidal-shaped population of high energy ions and electrons (1-300 kilo electron-Volts (keV)) [Daglis et al., 1999]. To form the toroidal shape in the inner magnetosphere, the particles execute 3 types of motion: gyromotion around a magnetic field line; bounce motion along a magnetic field line; and, drift motion perpendicular to the magnetic field [Walker and Russell, 1995].

Gyromotion, or cyclotron motion, exists because the particle is charged, moving, and in the presence of a magnetic field, see the left-hand panel of Figure 5. From the Lorentz force equation, the radius and period of the cyclotron motion are $r_c = (mv_\perp/|q|B)$ and $T_c = (2\pi m/|q|B)$, respectively, where m is the mass of the particle, v_\perp is the velocity of the particle perpendicular to the direction of the magnetic field, $|q|$ is the magnitude of the charge, and B is the local magnetic field. If changes in the magnetic field occur slowly compared to the cyclotron period ($1ms < T_c < 2s$), then the position of the particle is periodic and the magnetic moment of the particle's cyclotron motion is conserved. The magnetic moment is known as the first adiabatic invariant, $\mu = (mv_\perp^2/2B)$ [Walker and Russell, 1995].

Bounce motion along the magnetic field line is a result of a narrowing of the magnetic field at the poles, see the center panel of Figure 5. Splitting the motion of the particle into components aligned with the magnetic field (field-aligned) and components perpendicular to the magnetic field, the kinetic energy of the particle due to the perpendicular motion of the particle is the product of the first adiabatic invariant and the magnetic field strength. Since the magnetic field strength increases at the poles, to conserve the first adiabatic invariant, the perpendicular velocity of the particle increases as well. Because the total kinetic energy is conserved except in the presence of a field-aligned electric field, the field-aligned velocity must decrease as the perpendicular velocity increases [Walker and Russell, 1995]. When the field-aligned velocity reaches zero, the particle stops moving into the pole and mirrors, returning to the equatorial plane.

If the field-aligned velocity does not reach zero before the particle interacts with the ionosphere, the particle is defined as being in the loss cone. To determine if a particle will mirror before reaching the loss cone, the particle's pitch angle is calculated, $\alpha = \tan^{-1}(v_{\perp}/v_{\parallel})$ where v_{\parallel} is the particle velocity parallel to the magnetic field [Walker and Russell, 1995]. The closer the pitch angle is to zero, the more likely it will be lost. The exact pitch angle for the edge of the loss cone depends on ionospheric and magnetospheric conditions.

Except for particles lost to the loss cone, the bounce motion of a particle is periodic, thus there is a second adiabatic invariant associated with the bounce motion, $J = 2\sqrt{2m\mu} \int_{m_1}^{m_2} \sqrt{B_m - B(s)} ds$. J depends on the first adiabatic invariant, the mirror points (B_m , m_1 & m_2), and the magnetic field line being considered [Walker and Russell, 1995]. The second adiabatic invariant also requires the magnetic field to change slower than the bounce period of the particle, $\tau_b \sim 2(m_2 - m_1)/\langle v_{\parallel} \rangle$.

The drift motion of the particle perpendicular to the magnetic field is generated by the gradient of the magnetic field and the curvature of the magnetic field as well as electric fields. When the first and second adiabatic invariants are conserved, the bounce-averaged gradient-curvature drift depends on the gradient of the particle's kinetic energy, which can be defined in terms of the first and second adiabatic invariants. Equation (6) is the drift velocity of a particle, with the first term on the right hand side coming from the bounce-averaged gradient-curvature drift, the second term from electric fields, and the final term from any other external forces being applied to the particle.

$$\mathbf{v}_D = \mathbf{v}_{GC} + \mathbf{v}_{E \times \mathbf{B}} + \mathbf{v}_{ext} = \frac{\mathbf{B} \times \nabla W(\mu, J, \mathbf{x})}{qB^2} + \frac{\mathbf{E} \times \mathbf{B}}{B^2} + \frac{\mathbf{F}_{ext} \times \mathbf{B}}{qB^2} \quad (\text{drift velocity}) \quad (6)$$

where \mathbf{B} is the local magnetic field, $W(\mu, J, \mathbf{x})$ is the particle's kinetic energy as a function of the first and second adiabatic invariants and the particle's position, q is the charge of the particle, \mathbf{E} is the local electric field, and \mathbf{F}_{ext} is any additional forces. The sum of these drifts result in a circulation of the particles around the Earth, as pictured in the right-hand panel of Figure 5. The

period associated with this motion, $\tau_D = (2\pi r/v_{GC})$ where r is the radius of the drift shell, is much larger than both the cyclotron period and the bounce motion period, which makes drift motion much more susceptible to changes in the magnetic field [Walker and Russell, 1995]. The adiabatic invariant which can be derived from this motion has too large a time step compared to changes in the magnetic field in this work, and so will be ignored here.

As the particle population in the inner magnetosphere executes these 3 types of motion, currents are generated through differential drifts. The gradient-curvature drift is charge dependent and therefore causes a separation of the charged particles with electrons moving eastward and ions moving westward. The separation of charge allows for the formation of a drift current while retaining the quasi-neutral property of the plasma. Along with the gradient-curvature current, there is a magnetization current due to the cyclotron motion of the particles. Equation (7) is the combination of the gradient-curvature current and the magnetization current that are perpendicular to the magnetic field.

$$\mathbf{J}_\perp = \frac{\mathbf{B}}{B^2} \times \nabla p_\perp + (p_\parallel - p_\perp) \frac{\mathbf{B} \times (\mathbf{B} \cdot \nabla) \mathbf{B}}{B^4} \quad (7)$$

where p_\parallel and p_\perp are the pressures parallel and perpendicular to the magnetic field, respectively. If the pressure of the particle population was isotropic ($p_\parallel = p_\perp$), the second term would disappear, and the current would be due only to the cyclotron motion of the particles (the diamagnetic current). Therefore, any keV or greater particle population trapped in the inner magnetosphere generates current and adds to the strength of the ring current.

The formation of the ring current requires particles to be moved into the inner magnetosphere from the magnetotail. Two processes are thought to move the particles inward, energizing them along the way through the conservation of the first and second adiabatic invariants: enhanced magnetospheric convection [e.g., Zhou et al., 2003]; and, the interchange instability [Lemon et al., 2004].

Enhanced magnetospheric convection is generated through viscous interactions and the Dungey cycle (discussed in sections 1.2.1 and 1.2.2, respectively). The motion of the

plasma on closed field lines generates a large dawn-dusk electric field across the tail, creating an $E \times B$ drift which moves the plasma earthward. This motion is known as convection and brings plasma from the tail into the inner magnetosphere, building up the pressure and currents in the inner magnetosphere.

The interchange instability is a process by which low PV^γ flux tubes convect into the inner magnetosphere [Lemon et al., 2004]. Similar to the Rayleigh-Taylor instability, the interchange instability occurs when newly formed flux tubes in the tail have lower densities and energies than the surrounding plasma. The new flux tube has a lower pressure as well, and this pressure anisotropy creates field-aligned currents. The resulting electric field across the low pressure flux tube convects it earthward, interchanging it with flux tubes of greater pressure. As the flux tube convects earthward, the transport is adiabatic, so PV^γ is conserved where V is the volume per unit flux ($V = \int ds/B$) (also known as the flux tube volume). Since $B \sim r^{-3}$ as the flux tube convects toward Earth, V decreases, at the same time the pressure increases, and the plasma is energized. Once the low PV^γ flux tube reaches an area of similar pressure, it stops interchanging, and the accelerated plasma adds to the ring current strength.

The enhanced magnetospheric convection and interchange instability are not independent. Enhanced magnetospheric convection provides increased pressures in the inner magnetosphere that allow for deeper penetration of the low PV^γ flux tubes resulting in a more geoeffective injection into the ring current [Lopez et al., 2009]. Both processes are needed for a moderate to large geomagnetic storm.

1.1.4 The Ionosphere

The ionosphere coexists with the top layer of the atmosphere. Above 90 km altitude, the neutral atmosphere of Earth encounters several sources of ionization, e.g., photoionization and particle precipitation. The ionized particle population above 90 km is called the ionosphere. Because neutrals and charged particles coexist, the physics of the ionosphere is very different from the physics of the magnetosphere.

Within the ionosphere, the plasma is not collisionless due to the resistance of the neutral atmosphere. This means the neutrals and charged particles interact on a very short time scale and the magnetic field is not frozen to the plasma. Thus the plasma may flow and change without the magnetic field moving. The electromagnetic forces acting on the plasma do still exist though, and moving charged particles still create electric fields/currents and changes to the magnetic field.

When discussing the ionosphere in this work, we are mainly concerned with the portion of the ionosphere above the poles of the Earth. Centered on the magnetic dipole axis in the northern and southern hemispheres, the polar cap and auroral ovals have contact with both the magnetosheath and the magnetosphere via magnetic field lines. Figure 6 illustrates the location of the typical auroral oval imposed on a map of the North Pole. The polar cap would be considered the region poleward of the red grid in Figure 6.

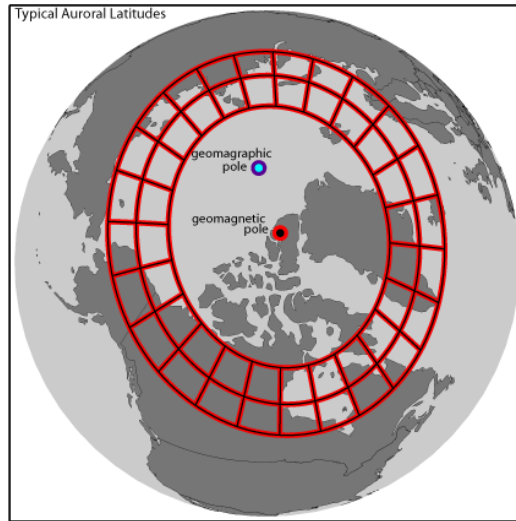


Figure 6. The typical location of the auroral latitudes. Image has a GNU Free Documentation License by Eric Donovan and is found at <http://commons.wikimedia.org/wiki/Aurora>.

1.1.4.1 Polar Cap

The polar cap is the region of the ionosphere where the magnetic field lines are interconnected with the IMF. Typically above ± 70 degrees magnetic latitude (MLAT), the polar

cap area grows and shrinks through dayside merging and night side reconnection (to be discussed in 1.2.2). Within the polar cap, the ionosphere is connected directly to the magnetosheath and solar wind.

1.1.4.2 Auroral Oval

The Auroral Oval is the region of the ionosphere where the footpoints of the outermost magnetospheric field lines map. Typically between ± 70 and ± 55 degrees MLAT, the auroral oval responds to dayside merging, night side reconnection, and viscous interaction.

In both the polar cap and the auroral oval, the convection of ionospheric plasma will generate an electric field in the ionosphere. The difference in the minimum and maximum potential of the electric field is called the transpolar potential. The transpolar potential is used to measure the convection in the ionosphere, and the ionospheric response to the solar wind. In this work, most of the results will be presented for the northern polar cap because the trends in both polar caps were about the same and discussion of the southern polar cap would be redundant.

1.2 Methods of Generating Magnetospheric and Ionospheric Convection

Three interactions between the magnetosheath and the magnetic field of the Earth generate convection in either the ionosphere and magnetosphere or in only the ionosphere. These interactions are at the center of the arguments presented in Chapter 4, where the difference between reconnection potential and lobe cell convection explains the difference between north-south interplanetary magnetic field (IMF) interactions and dawn-dusk IMF interactions.

1.2.1 Viscous Interaction

Viscous interaction [Axford & Hines, 1961] generates magnetospheric and ionospheric plasma convection on closed field lines via the transfer of solar wind momentum across the magnetopause to magnetospheric plasma. This generates anti-sunward plasma convection on closed field lines along the magnetopause and sunward flow deeper in the magnetosphere.

Magnetospheric stress is communicated on the field lines threading the flow to the ionosphere. The ionospheric convection is a mirror of the magnetospheric convection with anti-sunward on the poleward edge and sunward flow on the equatorward side of the auroral oval. This convection generates ionospheric electric fields. Newell et al. [2008], based on a multi-parameter study of magnetospheric state variables, concluded that the amount of viscous-generated transpolar potential is best represented by a factor proportional to the square of the solar wind speed and the square root of the solar wind density. A velocity-squared dependence was also suggested by Boyle et al. [1997]. The viscous interaction generates approximately 20-30 kV across the ionosphere for normal solar wind conditions [Reiff et al., 1981; Cowley, 1982; Boyle et al., 1997; Sonnerup et al., 2001; Newell et al., 2008].

1.2.2 Dungey Cycle

The Dungey cycle is a three-step process [Dungey, 1961]. Dayside merging generates ionospheric plasma convection on open field lines. Night side reconnection closes the open field lines, adding flux and energy to the magnetosphere. Magnetospheric convection occurs as the magnetic field returns to its initial position and the cycle can begin again. The magnetospheric convection from the Dungey cycle adds to the viscous interaction, generating more magnetospheric convection overall. This cycle is typically described using a southward IMF.

When the IMF in the magnetosheath is southward, the magnetosheath magnetic field merges with the magnetospheric field. The solar wind plasma flow draws the merged fields and plasma anti-sunward over the polar cap. The ionospheric plasma attached to the open field lines is also drawn anti-sunward. When the open field lines reconnect in the tail, the return flow in the ionosphere occurs at lower latitudes. The return flow in the magnetosphere is up the center of the magnetotail.

The Dungey cycle creates a two-cell convection pattern in the ionosphere for southward IMF. For dawn-dusk IMF orientations, dayside merging creates lopsided convection patterns [Heppner, 1977] and the role of the Dungey cycle is unclear.

For southward IMF, the ionospheric potential generated by the dayside merging is equal to the projection of the interplanetary electric field ($\text{IEF} = -VB_z$) on the extent of the flow that intersects the dayside merging line [Burke et al., 1999; Lopez et al., 2010]. For an IMF at an arbitrary clock angle (θ), one expects an additional $\sin^2(\theta/2)$ dependence of the potential [Kan & Lee, 1979; Hu et al., 2009]. Dayside merging may produce up to 200 kV of the total transpolar potential [Reiff & Luhmann, 1986; Boyle et al., 1997; Hairston et al., 2003; Ober et al., 2003].

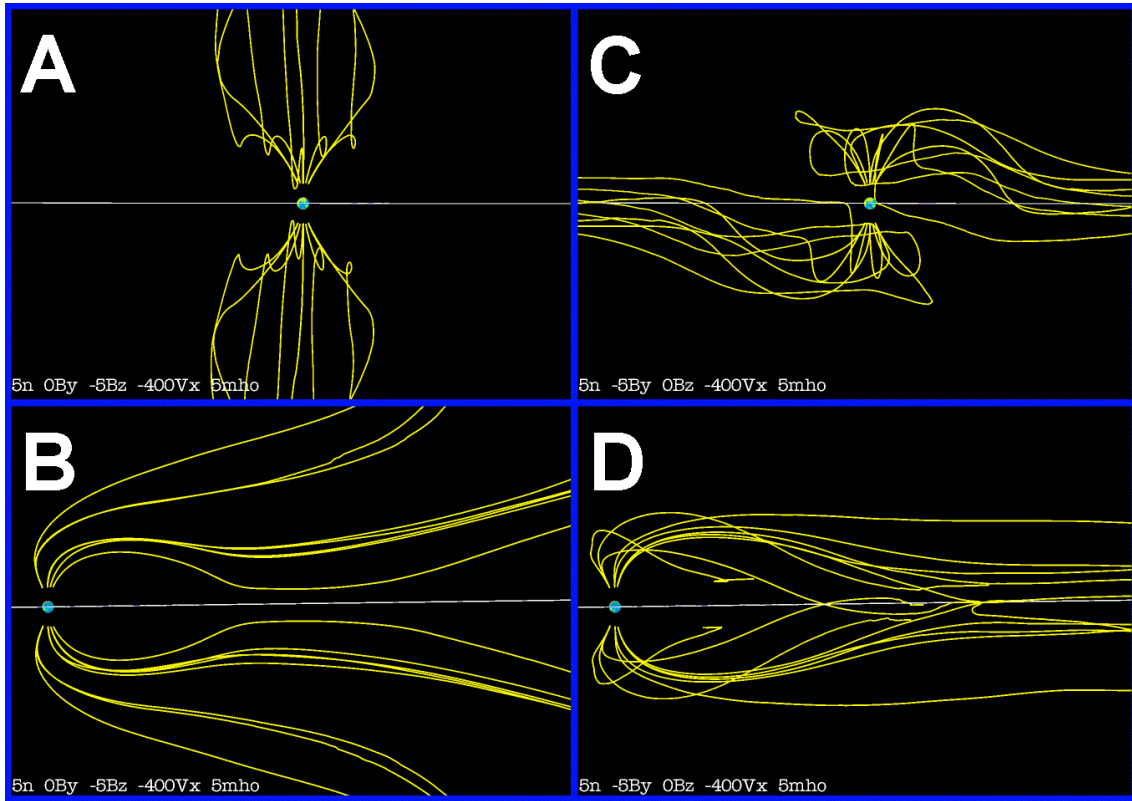


Figure 7. The northern and southern magnetotail lobes for southward IMF ((A) looking from the Sun and (B) looking from the dusk side of Earth) and for downward IMF ((C) looking from the Sun and (D) looking from the dusk side of Earth) created from LFM runs of $u_x = -400 \text{ km/s}$, $n = 5 \text{ cm}^{-3}$, and $|B| = 5 \text{ nT}$ in CISIM-DX.

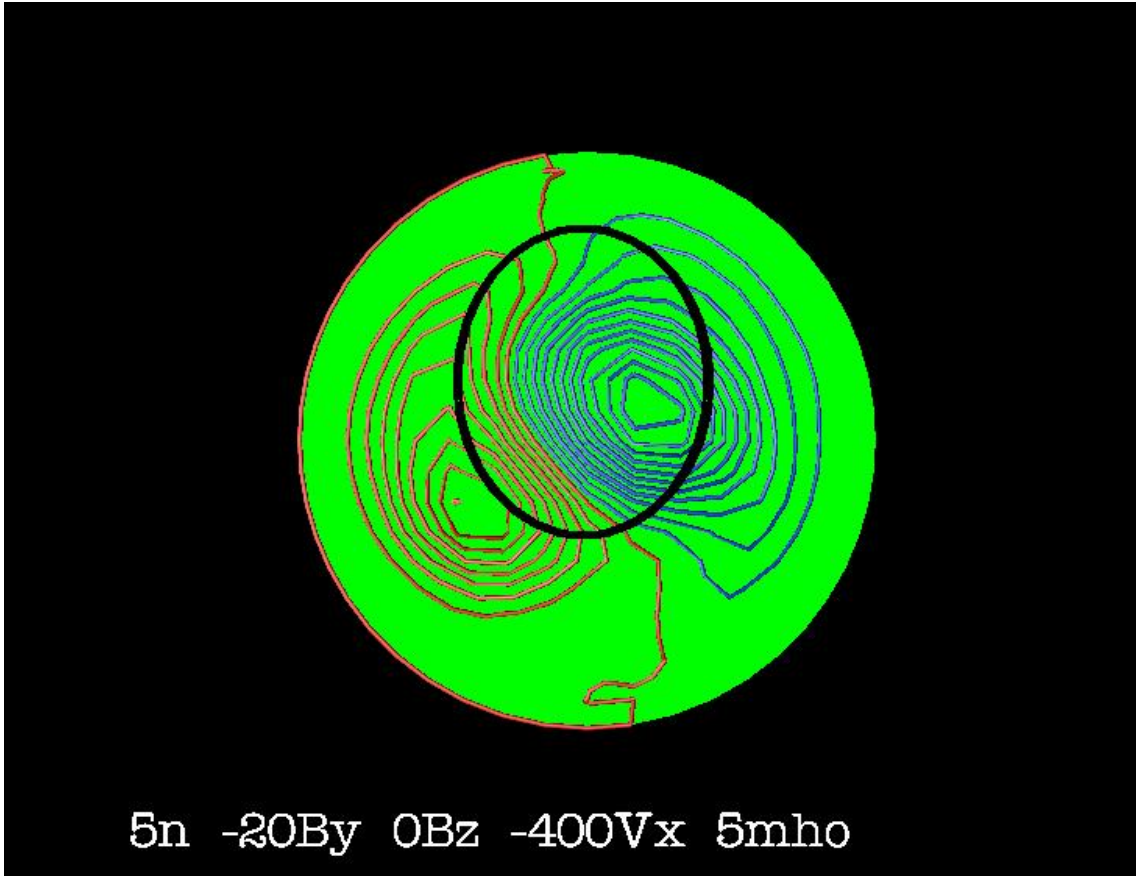


Figure 8. Contours (blue and red) of northern polar cap potential for LFM run of $u_x = -400$ km/s, $n = 5 \text{ cm}^{-3}$, and $B_y = -20$ nT. The open-closed boundary (thick black line) is hypothetical, and placed to show how closed convection can be within the open field line region. The noon is at the top of the picture.

1.2.3 Lobe Cell Convection

A lobe cell is the region in the polar cap to which the magnetotail lobe for that hemisphere maps magnetically. All of the field lines in the lobe are open. Figure 7 illustrates the magnetotail lobes for southward IMF (Panel A and B) and dawn-dusk IMF (Panel C and D).

Lobe cell convection is ionospheric convection within the lobe cell in which some closed convection (convection which completes a full circle) occurs. This closed convection in the lobe cell is entirely in the open field line region during periods of large dawn-dusk IMF [e.g., Eriksson et al., 2003] (see Figure 8). While there are theoretical arguments to question whether

ionospheric sunward convection is actually possible on open field lines [Hill, 1994], MHD simulations [Crooker et al., 1998] suggest that this is the case. The MHD simulations suggest that the sunward ionospheric convection is decoupled from anti-sunward, high-altitude flow as the field lines nominally connecting the two regions encounter the merging line diffusion region (region of polar cap near open-close field line boundary) and lose their identity. Thus lobe cell convection could be driven by the solar wind and, at least the sunward component, would have no magnetospheric counterpart. Discussion and proof of this are shown in section 4.2.6.

Another feature of ionospheric convection driven by dawn-dusk IMF is asymmetric convection cells with the potential across one cell being larger than the potential across the other (see Figure 8). The asymmetry comes from the lobe cell being located in one of the two convection cells. Only one lobe cell occurs in an ionosphere at a given time. Crooker et al. [1998] showed that the potential disparity was located in the lobe cell. The convection represented by this potential is then entirely on open field lines, and at least some of the ionospheric flow has no high-altitude counterpart. Such ionospheric convection is not expected to produce any magnetospheric flow into the inner magnetosphere since all of the convection is on open field lines.

1.3 Theories of Transpolar Saturation

The total transpolar potential (the sum of potential produced by viscous interaction, dayside merging, and lobe cell convection) varies with the magnitude and clock angle of the IMF, solar wind speed, and density [Kan & Lee, 1979; Reiff et al., 1981; Cowley, 1982; Reiff & Luhmann, 1986; Boyle et al., 1997; Crooker et al., 1998; Sonnerup et al., 2001; Hairston et al., 2003; Ober et al., 2003; Lopez et al., 2004; Newell et al., 2008; Hu et al., 2009; Mitchell et al., 2010]. For low values of southward IMF and solar wind speed, the transpolar potential responds linearly to increases in the IMF [Lopez et al., 2009 & references therein]. For larger values of IMF, the extrapolated linear transpolar potential over-predicts the observations; the transpolar potential saturates [Russell et al., 2001; Siscoe et al., 2002a&b; Ridley, 2007;

Kivelson & Ridley, 2008; Lopez et al., 2010]. Transpolar potential saturation is currently explained by three models: the Region 1 Current (R1) model [Siscoe et al., 2002 a&b]; the Alfvén Wing (AW) model [Ridley, 2007; Kivelson & Ridley, 2008]; and, the Magnetosheath Force Balance (MFB) model [Lopez et al., 2010].

1.3.1 *Region 1 Current Theory*

The Region 1 Current (R1) model suggests the dayside merging portion of transpolar potential (reconnection potential) saturates because the R1 current reduces the dayside magnetic field [Siscoe et al., 2002a&b]. This reduction limits the rate of dayside merging [Siscoe et al., 2002a&b]. If the merging rate is limited, then the reconnection potential is limited. Once the reconnection potential saturates, Siscoe et al. [2002b] suggest that the R1 current closes on the bow shock, replacing the Chapman-Ferraro current in balancing the pressure of the solar wind on the magnetosphere. The magnitude of the R1 current is limited to the amount necessary to balance the solar wind [Siscoe et al., 2002b]. Thus the amount of current in the system cannot exceed the value needed to stand off the solar wind and once the reconnection potential saturates the amount of potential will be directly proportional to the amount of R1 current needed to stand off the solar wind. Via Ohm's law, the amount of current is proportional to the product of the reconnection potential and the conductivity of the ionosphere. Thus for the R1 model to be valid, the reconnection potential must saturate at the same value for any given IEF if the conductivity and the solar wind dynamic pressure are constant.

1.3.2 *Alfvén Wing Theory*

The Alfvén Wing (AW) model suggests the generation of Alfvén wings controls the saturation of the reconnection potential [Ridley, 2007; Kivelson & Ridley, 2008]. Alfvén wings are created by Alfvén waves traveling along a magnetic field [Ridley, 2007 & references therein]. The bending of a magnetic field as it flows around an object in space creates an Alfvén wave, producing a cavity at an angle to the object. This angle is defined by the Alfvén Mach number, or the ratio of solar wind velocity to Alfvén wave velocity. This cavity is called an

Alfvén wing. The Alfvén velocity is proportional to the magnitude of the IMF, so increasing the Alfvén velocity increases the Alfvén wing angle. The larger the angle in an Alfvén wing, the lower its internal electric field. The Alfvén wing electric field, which is considered to be the driver of the ionospheric field, correlates with the behavior of the reconnection potential in the simulations run by Ridley [2007].

Ridley [2007] also notes that this method operates irrespective of the orientation of the IMF, and further states the Alfvén velocity must be more than a quarter of the value of the solar wind velocity for any effects to occur. Full formation of Alfvén wings and full saturation effects are found when the Alfvén velocity is greater than the solar wind velocity [Ridley, 2007]. For $u_{sw} = 400 \text{ km/s}$ and $n_{sw} = 5 \text{ cm}^{-3}$, full formation of Alfvén wings (Alfvén Mach number ≤ 1) would require an IMF of greater than 41 nT. These conditions rarely occur in the solar wind, and transpolar saturation is seen in several studies at lower IMF values [Hairston et al., 2003; MacDougall & Jayachandran, 2006; Lopez et al., 2009]. Some effects could be expected for $u_{sw} = 400 \text{ km/s}$, $n_{sw} = 5 \text{ cm}^{-3}$, and an IMF of 10.25 nT or greater (Alfvén Mach number ≤ 4). The only further requirement for Alfvén wings is the time necessary to develop. Ridley [2007] estimates it takes roughly an hour for the Alfvén wave to propagate along the Alfvén wing for $u_{sw} = 400 \text{ km/s}$, $n_{sw} = 5 \text{ cm}^{-3}$, and an IMF of 20.5 nT. Thus for the AW model to be valid, the reconnection potential cannot saturate within an hour of the Alfvén Mach number decreasing below 4. Further, the Alfvén Mach number must remain less than 4 during saturation.

1.3.3 Magnetosheath Force Balance Theory

The Magnetosheath Force Balance (MFB) model explains both the linear response of the transpolar potential to the IEF for small IMF and the saturation of the transpolar potential in a single conceptual model. The MFB model treats the viscous portion of the transpolar potential as a function of solar wind speed and density, decoupling the viscous interaction from changes in the IMF. The MFB model suggests the saturation of the reconnection potential is controlled by the relative importance of the $j \times B$ force in the magnetosheath [Lopez et al., 2010]. From

the momentum equation (8), it is seen that the $\mathbf{j} \times \mathbf{B}$ force and the gradient of the plasma pressure are the total force exerted on plasma.

$$\rho \left(\frac{\partial \mathbf{u}}{\partial t} + \mathbf{u} \cdot \nabla \mathbf{u} \right) = -\nabla \cdot \mathbf{p} + \mathbf{j} \times \mathbf{B} \quad (\text{momentum equation}) \quad (8)$$

where ρ is the mass density of the plasma, \mathbf{u} is the plasma velocity, \mathbf{p} is the local pressure tensor, \mathbf{j} is the local current density, and \mathbf{B} is the local magnetic field. The relative importance of either force can be determined from the ratio of plasma pressure to magnetic pressure ($\beta_{ms} = \frac{p}{(B^2/2\mu_0)}$). During nominal solar wind conditions, the plasma pressure gradient is the dominant force in the magnetosheath ($\beta_{ms} \gg 1$). It diverts the flow around the magnetosphere producing a geoeffective length in the solar wind (the distance between the last two flow lines to intersect the merging region) that is much less than the width of the magnetosphere [Burke et al., 1999; Lopez et al., 2010]. As the solar wind magnetic field increases, β_{ms} approaches 1. At that point the $\mathbf{j} \times \mathbf{B}$ force is of comparable magnitude to the gradient of the plasma pressure, and any increase of the magnetic field in the solar wind increases the $\mathbf{j} \times \mathbf{B}$ force in the magnetosheath causing a proportionally greater diversion of the flow around the magnetopause [Lavraud and Borovsky, 2008; Lopez et al., 2010].

This greater diversion of the magnetosheath flow decreases the geoeffective length in the solar wind [Lopez et al., 2010]. The projection of the IEF on the extent of the solar wind flow that intersects the dayside merging line is the reconnection potential. Thus, the reconnection potential is limited even as the IMF increases because the extent of the solar wind flow that intersects the dayside merging line decreases as the IMF increases [Lopez et al., 2010]. Thus for the MFB model to be valid, the reconnection potential must transition to saturation as β_{ms} approaches 1 in the nose of the magnetosheath regardless of the orientation of the IMF.

1.4 Outline for Dissertation

Having laid out the background material above, the following 2 chapters describe the tools used for this research. Chapter 2 describes the ideal MHD equations, the LFM global MHD simulation, the CRCM simulation, and the work done to one-way couple the LFM to the

CRCM. Chapter 3 describes the data products used to complete this study. The results of this research are presented and discussed in Chapter 4. The conclusions and future work are discussed in Chapter 5.

CHAPTER 2

SIMULATIONS

In the exploration of the Sun-Earth system, *in situ* measurements are sparse and limited in comparison to the vast domain being studied. To make-up the lack of measurements and the inability to control conditions, several models of the whole, or partial, system have been created. Models may be based on fits to measurements (empirical), a mixture of physics and measurements (semi-empirical), or purely physics (physics-based). Semi-empirical and physics-based models use a combination of kinetic theory and fluid dynamics to explain the motion of the plasma within the model. This chapter focuses on the use of fluid dynamics in a physics-based model called the Lyon-Fedder-Mobarry global Magneto-Hydrodynamic (MHD) simulation [Fedder et al., 1995 a&b; Lyon et al., 2004], and on the use of kinetic theory in a physics-based model called the Comprehensive Ring Current Model (CRCM) [Fok et al., 2001].

2.1 Ideal MHD Equations

Magneto-hydrodynamics (MHD) is the study of the motion of an electromagnetic fluid (e.g., space plasma). The MHD equations are derived mathematically from the Vlasov equation, or more intuitively using the laws of conservation of mass, momentum, and energy along with Maxwell's equations and the ideal gas law [e.g., Kivelson and Russell, 1995]. Several basic assumptions are made about the plasma: it is electrically neutral; it is made of two species of particles (ions and electrons); the periods of cyclotron motion and inverse plasma frequency are very small compared to the time scales being examined; and, the Debye length is much smaller than the spatial scales being examined. Under these assumptions, the ideal MHD equations are

$$\frac{\partial \rho}{\partial t} + \nabla \cdot \rho \mathbf{u} = 0 \quad (\text{continuity equation}) \quad (9)$$

$$\rho \left(\frac{\partial \mathbf{u}}{\partial t} + \mathbf{u} \cdot \nabla \mathbf{u} \right) = -\nabla \cdot \mathbf{p} + \mathbf{j} \times \mathbf{B} \quad (\text{momentum equation}) \quad (10)$$

$$\nabla \times \mathbf{B} = \mu_0 \mathbf{j} \quad (\text{Ampere's Law in MHD limit}) \quad (11)$$

$$\frac{\partial \mathbf{B}}{\partial t} = -\nabla \times \mathbf{E} \quad (\text{Faraday's Law}) \quad (12)$$

$$\mathbf{E} + \mathbf{u} \times \mathbf{B} = 0 \quad (\text{frozen-in flux condition}) \quad (13)$$

where ρ is the mass density, \mathbf{u} is the center of mass velocity, \mathbf{p} is the plasma pressure tensor, \mathbf{j} is the current density, \mathbf{B} is the magnetic induction (though its referred to as the magnetic field by convention), and μ_0 is the permeability of free space ($4\pi \times 10^{-7}$ N A²). The frozen-in flux condition (13) is derived from Ohm's Law, assuming collisionless plasma with extremely large conductivity. The pressure tensor (\mathbf{p}) in the momentum equation can be simplified to a scalar (p) under the assumption of an isotropic distribution. Combining the momentum equation (10) and Ampere's Law (11) as well as Faraday's Law (12) and the frozen-in flux condition (13), these equations can be reduced to three of the four familiar ideal MHD equations.

$$\frac{\partial \rho}{\partial t} + \nabla \cdot \rho \mathbf{u} = 0 \quad (9)$$

$$\rho \left(\frac{\partial \mathbf{u}}{\partial t} + \mathbf{u} \cdot \nabla \mathbf{u} \right) = -\nabla p - \frac{1}{2\mu_0} \nabla B^2 + \frac{1}{\mu_0} (\mathbf{B} \cdot \nabla) \mathbf{B} \quad (10')$$

$$\frac{\partial \mathbf{B}}{\partial t} = \nabla \times (\mathbf{u} \times \mathbf{B}) \quad (12')$$

At this point, there are seven equations and eight unknowns in this system of equations. To close the system of equations, an equation of state relating pressure and density is needed. Assuming the plasma changes adiabatically, the equation of state is,

$$\frac{d}{dt} (p\rho^{-\gamma}) = 0 \quad (\text{adiabatic condition}) \quad (14)$$

where γ is the ratio of the specific heat at constant pressure to the specific heat at constant volume. These four equations are termed the ideal MHD equations. The LFM global MHD simulation modifies these equations slightly in order to handle some numerical issues [Lyon et al., 2004].

2.2 The Lyon-Fedder-Mobarry Global Magneto-Hydro-Dynamic Simulation

2.2.1 An Overview of the LFM

John Lyon, Joel Fedder, and Clark Mobarry began building the LFM global MHD simulation in 1985 [Lyon et al., 2004]. Along with many others over the years, Lyon, Fedder, and Mobarry have created a 3-dimensional code which simulates the solar wind-magnetosphere-ionosphere interactions from 30 Earth Radii (R_E) upstream to -300 R_E downstream and 100 R_E radially outward in all directions from the x-axis, which points upstream and is perpendicular to the dipole (SM coordinates). The LFM simulation can take either real or idealized solar wind conditions (as discussed below) and propagate them through the system. The simulation output includes the density, velocity, pressure, magnetic field, and energy for all locations within the solar wind and magnetosphere, as well as the ionospheric potentials, currents, Pedersen and Hall conductances, and particle fluxes and energies. With visualization software [Wiltberger et al., 2005], the output shows the simulation resolves the Bowshock, magnetopause, and many details within the magnetosphere (see Figure 9).

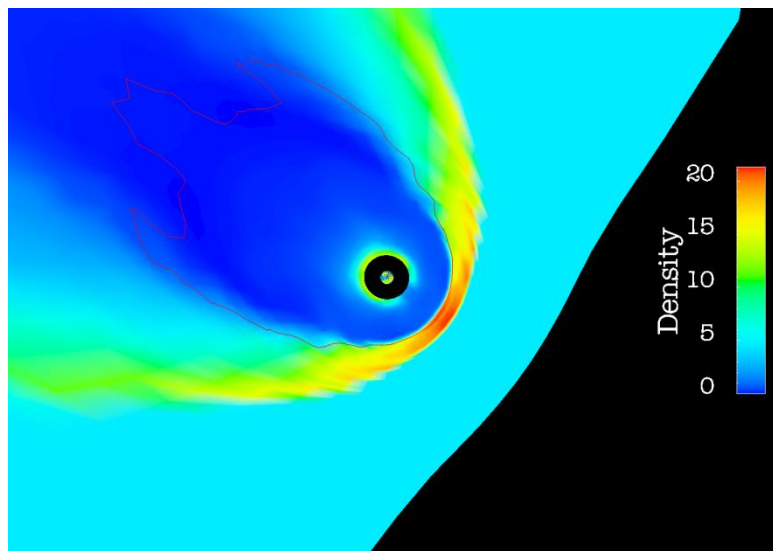


Figure 9. Equatorial plane for LFM simulation run with a density of 5 cm⁻³. The bow shock and magnetosheath are visible as the high density region. The red line marks the $B_z=0$ contour.

2.2.2 Six Considerations of Modelers in Creating LFM

When the modelers first decided to create the LFM simulation, six issues drew special attention and planning: resolution of features due to propagating scheme; resolution of features due to grid size; requirement that $\nabla \cdot \mathbf{B} = 0$; length of the time step; truncation errors causing unphysical values; and, realistic ionospheric conditions. Lyon et al. [2004] and Fedder et al. [1995 a&b] outline the features of the LFM global MHD simulation which address these issues. The following sections reference these works almost exclusively.

2.2.2.1 Resolution of Features

To solve a system of equations, such as the MHD equations, an algorithm is needed in which the solution is done self-consistently and simultaneously. Propagating the plasma from one grid cell to the next, the algorithm also needs to be able to resolve sharp boundary conditions, such as the bow shock. To resolve such features, a modeler has two possible choices: use an algorithm with high spatial order derivatives and/or add more grid cells to the areas of interest *a priori*. The problem with high spatial order algorithms is that they require large computational resources compared to first order schemes, and first order schemes are usually enough for the propagation of plasma.

LFM uses a total variation diminishing (TVD) algorithm with the partial donor cell method as its limiter [Lyon et al., 2004 & references therein] to propagate plasma through its grid. The TVD algorithm chooses when propagation can be done with a first order scheme and when it needs the more computationally intensive high-order scheme to resolve greater detail. The partial donor cell method is the high order scheme used. It is an 8th spatial order scheme, which Lyon et al. [2004] showed to be the best choice to balance computational resources and resolution of features.

The LFM grid is also modified for better resolution of features. The LFM grid is a non-orthogonal distorted spherical grid (see Figure 10). The SM x-axis is the line from which θ is

measured and around which Φ is rotated. The distortion is along the r and θ directions. The grid is calculated “by minimizing a weighted smoothness integral” [Lyon et al., 2004]. This allows more cells to be clustered in the bow shock, magnetopause, and magnetotail regions, which aides in resolving these regions.

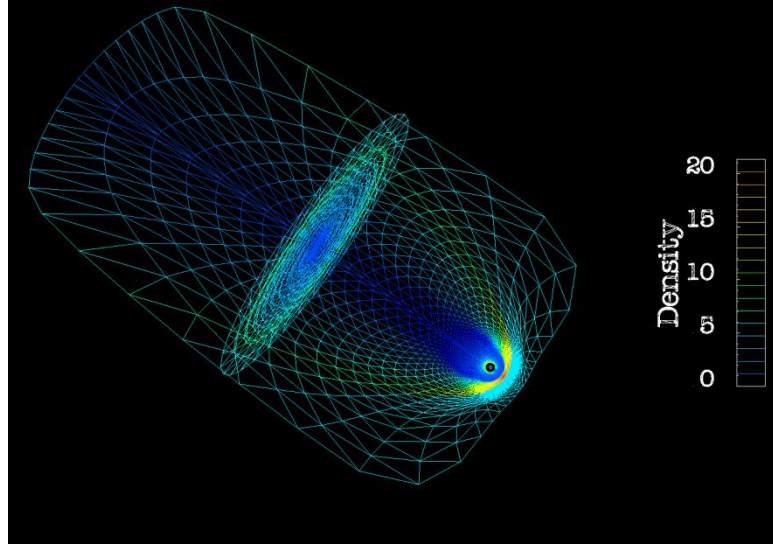


Figure 10. The equatorial and cross-sectional planes of the LFM simulation grid. The grid is a cylinder with higher density of cells near the Earth.

Between the specialized grid and the TVD algorithm, the LFM is capable of resolving the bow shock within one or two cells as well as resolving the density drop at the magnetopause.

2.2.2.2 $\nabla \cdot \mathbf{B} = 0$

While Maxwell’s equations clearly state $\nabla \cdot \mathbf{B} = 0$, the MHD equations can be formulated to allow a finite $\nabla \cdot \mathbf{B}$ which arises from numerical error. But, a finite $\nabla \cdot \mathbf{B}$ means the magnetic field lines do not have to close on themselves and magnetic helicity ($\int \mathbf{A} \cdot \mathbf{B} d^3r$, where \mathbf{A} is the vector potential of \mathbf{B}) is not conserved. As discussed in Chapter 1, the cycle of opening and closing field lines defines a large part of the study of the transfer of energy between the solar wind and magnetosphere-ionosphere. Thus, the conservation of magnetic helicity is an important feature in a global MHD simulation.

The TVD algorithm used in LFM creates cell-centered plasma quantities; conservation of magnetic helicity cannot be done using cell-centered quantities. Thus, the insight by Klaus Hain, John Lyon, and Steve Zalesak in the late 1970s, that a TVD scheme applied on a Yee [1966] grid will allow $\nabla \cdot \mathbf{B} = 0$, is used [Lyon et al., 2004]. The Yee grid staggers the magnetic field variables from the plasma quantities, calculating the total flux through a cell-surface. Then, using Faraday's Law, the local electric field is modified to conserve $\nabla \cdot \mathbf{B} = 0$ at the surfaces of the cell. To calculate the plasma quantities, the magnetic field is derived at the cell-center from the total flux through the surfaces of the cell. This allows the conservation of magnetic helicity as well as the propagation of the plasma quantities in the LFM simulation.

2.2.2.3 Time Step

The Courant condition [Courant et al., 1928] requires the time step in a numerical simulation to be less than the time it takes a wave to travel between two adjacent grid points. Under this condition, the LFM time step is restricted by the Alfvén speed, the higher the Alfvén speed the smaller the time step. Near the Earth in the inner magnetosphere and in the tail lobes, the Alfvén speed reaches extremely high values, making the time step too small to be practical. Near Earth, the issue is fixed by setting the inner boundary of the simulation at $\sim 3 R_E$. It is not so simple in the tail lobes.

Several techniques are available to lengthen in the time step, but the easiest to implement is the Boris (Alfvén) correction [Boris, 1970]. The Alfvén speed is limited by the displacement current to the speed of light, as seen in Ampere's Law. Thus, if the displacement current is included in Ampere's Law when it is substituted into the momentum equation, the resulting momentum will restrict the Alfvén speed to the speed of light specified in Ampere's law [Lyon et al., 2004]. By decreasing the speed of light in the simulation, the time step in lobes may be lengthened to a practical value. Thus, most LFM simulation runs set the speed of light to 1.1×10^8 cm/s.

2.2.2.4 Truncation Errors

LFM modelers considered two places where truncation errors could lead to unphysical results from the model: regions of low β (ratio of plasma pressure to magnetic pressure); and, regions of high magnetic field. The regions of low β produce truncation errors in the plasma energy when the total energy equation is used to close the MHD equations. The plasma energy is the difference in the total energy and magnetic energy. The regions of high magnetic field produce truncation errors in the magnetic field derivatives used to find field-aligned currents.

The solution to the low β issue is to use a different equation to close the MHD equations. The LFM modelers chose to use the plasma energy equation, even though it is not conservative, to close the MHD equations. Lyon et al. [2004] outlines the logic of this choice, showing that while not conservative, the plasma energy equation creates the same conditions as the total energy equation in most important places. The one place the plasma energy equation does not perform well is at the reconnection sites. Because the energy is plasma only, no provision is made for the creation of Joule heating, instead the energy which would have created Joule heating just disappears. These errors are local though, and do not seem to affect the global energy budget much [Lyon et al., 2004]. The modified MHD equations are presented in section 2.2.3.

The solution to the high magnetic field issue is to subtract a fictitious magnetic field from the true magnetic field [Lyon et al., 2004]. The fictitious field equals a dipole magnetic field in the inner magnetosphere and drops to zero farther out. The removal of the field allows the derivatives to be calculated without truncation.

2.2.2.5 Ionosphere

The ionosphere dissipates a large amount of energy from the solar wind and from the magnetosphere. Though LFM considers the ionosphere a boundary condition, the importance of this boundary condition suggests the use of a model, which can return values in a self-consistent way. The current stand-alone LFM simulation has two simple models with self-

consistent electrodynamic coupling to the magnetosphere. The simpler of the two uses a uniform height-integrated conductance and maps the field-aligned currents (FACs) from the inner boundary to the ionosphere. Calculating the convection electric field, the model maps the resulting field back to the inner boundary and computes the necessary boundary conditions for the magnetic field and plasma momentum. The second model uses a conductance model with solar extreme ultraviolet (EUV) irradiance and auroral precipitation input. The solar EUV is fixed in time, and can vary in space with respect to the solar zenith angle and observed solar radio flux at the 10.7 cm line. The auroral precipitation is calculated in two steps using the plasma and field values at the inner boundary of the LFM simulation. The first step calculates the energy and number flux of the electron precipitation at the inner boundary. The second step adjusts for the presences of a field-aligned electric field. Each input provides a Pedersen and Hall conductance, the total Pedersen and Hall conductance are calculated by taking the square root of the sum of the square of the EUV contribution and the square of the auroral contribution. The resulting Pedersen and Hall conductance are used to map the FACs to the ionosphere, calculate the convection electric field, and map the resulting electric field back to the inner boundary. Again the necessary boundary conditions for the magnetic field and plasma momentum are calculated, and the simulation can continue.

While the simpler model of the ionosphere is not completely physical, it does provide knowledge of the interaction of FACs with the ionosphere for given solar wind conditions. The ionosphere model based on solar EUV provides a more accurate picture of the ionosphere, but does not give the control of system variables in quite the same way. Depending on the experiments being conducted with the simulation, the ionospheric models are switched to provide the best experimental set-up.

2.2.3 Modifications of Ideal MHD Equations

The ideal MHD equations use the conservation of energy or an equation of state to close the system of equations, as outlined in section 2.1. The LFM simulation modified the ideal

MHD equations to use the plasma energy equation instead of the total energy equation, as outlined in section 2.2.2.4. To obtain the plasma energy equation, the momentum equation (10') is dotted with the velocity, giving the total energy equation (15).

$$\frac{\partial}{\partial t} \left(\frac{\rho u^2}{2} + \frac{p}{\gamma-1} + \frac{B^2}{2\mu_0} \right) + \nabla \cdot \left(\frac{\rho u^2}{2} \mathbf{u} + \frac{\gamma}{\gamma-1} p \mathbf{u} + \frac{\mathbf{E} \times \mathbf{B}}{\mu_0} \right) = 0 \quad (\text{total energy eqn.}) \quad (15)$$

From this expanded version of the total energy equation, the plasma energy terms are separated out, leaving the magnetic energy terms to be condensed into the $\mathbf{j} \cdot \mathbf{E}$ term on the right hand side of (16).

$$\frac{\partial}{\partial t} \left(\frac{\rho u^2}{2} + \frac{p}{\gamma-1} \right) = -\nabla \cdot \left(\frac{\rho u^2}{2} \mathbf{u} + \frac{\gamma}{\gamma-1} p \mathbf{u} \right) + \mathbf{j} \cdot \mathbf{E} \quad (\text{plasma energy eqn.}) \quad (16)$$

The $\mathbf{j} \cdot \mathbf{E}$ term is then replaced with the dot product of the velocity and magnetic force, giving the four MHD equations used in the LFM simulation (written in cgs units here) [Lyon et al., 2004].

$$\frac{\partial \rho}{\partial t} = -\nabla \cdot \rho \mathbf{u} \quad (\text{continuity eqn.}) \quad (9')$$

$$\frac{\partial \rho \mathbf{u}}{\partial t} = -\nabla \cdot (\rho \mathbf{u} \mathbf{u} + \mathbf{I} P) - \nabla \cdot \left(\mathbf{I} \frac{B^2}{8\pi} - \frac{\mathbf{B}\mathbf{B}}{4\pi} \right) \quad (\text{momentum eqn.}) \quad (10'')$$

$$\frac{\partial E_p}{\partial t} = -\nabla \cdot \left(\mathbf{u} \left(\frac{\rho u^2}{2} + \frac{\gamma}{\gamma-1} P \right) \right) - \mathbf{u} \cdot \nabla \cdot \left(\mathbf{I} \frac{B^2}{8\pi} - \frac{\mathbf{B}\mathbf{B}}{4\pi} \right) \quad (\text{plasma energy eqn.}) \quad (16')$$

$$\frac{\partial \mathbf{B}}{\partial t} = \nabla \times (\mathbf{u} \times \mathbf{B}) \quad (\text{Faraday's Law}) \quad (12'')$$

where $E_p = \frac{\rho u^2}{2} + \frac{P}{\gamma-1}$.

2.2.4 Boundary Conditions of Simulation

The LFM simulation has two boundaries: the inner boundary at $\sim 3 R_E$; and, the outer surface of the grid. The inner boundary is a sphere and was discussed in section 2.2.2.5. The outer surface of the grid is a cylinder, as seen in Figure 10. This allows the boundaries in the θ and Φ directions to be periodic [Lyon et al., 2004].

In LFM, the axis of the cylinder always lies in the magnetic equatorial plane and the dipole is always at a 90 degree angle to this plane [Lyon et al., 2004]. This means the input solar wind must be in solar magnetic coordinates. The front end of the cylinder is $\sim 30 R_E$

upstream of the Earth, while the back end of the cylinder is $\sim 300 R_E$ downstream of the Earth. The side of the cylinder is $\sim 100 R_E$ from the long axis in all directions. The front end and frontal side cells use the solar wind input for boundary conditions. The back side and end cells use the supersonic outflow for boundary conditions. If the transverse magnetic field of the boundary conditions does not match the transverse magnetic field of the outside cells, a diffusive electric field is maintained to avoid magnetic “hang ups” on the boundary [Lyon et al., 2004].

The magnetic field and plasma conditions are propagated to the boundary by subtracting the time it would take for the plasma to reach the cell from the simulation time and extracting the input data with the same time stamp. This procedure is known as ballistic propagation, and works well for uniform or slowly varying solar wind speeds. If the solar wind velocity has large variations, this method causes a loss of data, but maintains the single value per boundary cell condition, as needed by LFM.

2.2.5 Format of Input and Output of Simulation

The user may set a variety of conditions in the LFM. Solar wind input may be either ideal or real solar wind conditions. The ionosphere may have uniform conductance or use the solar EUV irradiance to calculate the conductance. The dipole may be tilted or not. The exact conditions under which the simulation is run are described in the section where the corresponding results are discussed.

When the particular LFM run is created, the user may also choose how often the simulation outputs data. This work has the simulation “dump” data every 250 steps, which is roughly 1.25 minutes of simulation time. The LFM simulation outputs data from the solar wind, magnetosphere, and ionosphere in hierachal data format (HDF) files. The HDF files contain the fictitious magnetic field (section 2.2.2.4) and the LFM grid, which remain the same for all time steps. The HDF files also contain the density, velocity, sound speed, and magnetic field at the cell centers as well as the magnetic fluxes and electric fields on the cell surfaces for each “dumped” time step. The ionospheric potential, field-aligned currents, Pedersen and Hall

conductances, particle fluxes, and particle energies are also stored for each hemisphere and each “dumped” time step.

2.2.6 Method of Visualization of Simulation Results

The HDF files require some special programming to access and visualize. Currently, the results of LFM runs are visualized using CISIM-DX, a modified version of Open-DX [Wiltberger et al., 2005]. Open-DX was created by IBM and then made open source. Figure 9 is an example of the CISIM-DX imaging.

2.3 The Comprehensive Ring Current Model

The Comprehensive Ring Current Model (CRCM) is a physics-based model. It uses the self-consistent electric field of the Rice Convection Model (RCM), and solves the Boltzmann transport equation for the phase space density of the energetic (> 1 keV) inner magnetosphere plasma [Fok et al., 2001]. Accounting for anisotropic pitch angle distributions, the CRCM balances the input from the plasma sheet with the loss through charge exchange and the loss cone. Numerous studies have used the CRCM in conjunction with a magnetic field model to examine the ring current response to geomagnetic storms and substorms [e.g., Fok et al., 2001; Ebihara et al., 2005; Fok et al., 2006].

2.3.1 An Overview of CRCM

As discussed in Chapter 1, the ring current is a transient torus of energetic particles in the inner magnetosphere. When modeling the ring current, the sources and sinks of particles in the inner magnetosphere need to be taken into account, including convection from the plasma sheet, charge exchange, and particles removed through the loss cone. Along with the sources and sinks, the particles may be constrained by three adiabatic invariants in which the integral $\oint p dq$ in systems with periodic motion is a constant of the motion under certain circumstances [Goldstein, 1980].

The first and second adiabatic invariants relate to the gyromotion of the particle in a magnetic field and the bounce motion of the particle along a field line, respectively. The third

adiabatic invariant pertains to the drift of particles on trajectories within the magnetosphere. For the adiabatic invariant to be conserved, the magnetic field must change slower than the time scale associated with the adiabatic invariant. Thus, for the first adiabatic invariant, changes in the magnetic field must occur slower than the gyroperiod. CRCM conserves the first and second adiabatic invariants. The period of the third adiabatic invariant is too long to assume its invariance in the model.

Along with the first two adiabatic invariants, CRCM uses the ionospheric foot points, instead of its equatorial crossing point, to label the phase space distribution on each field line [Fok et al., 2001]. Beginning in the ionosphere, CRCM uses a modified RCM to calculate the field-aligned currents with an arbitrary pitch angle distribution. The CRCM and RCM assume the polar regions of the ionosphere are symmetric, and thus they need only solve equations for one hemisphere.

Using specified height-integrated conductance, the modified RCM calculates the ionospheric electric potential from the field-aligned currents [Fok et al., 2001]. Then, the CRCM calculates the bounce-averaged drift velocities (the gradient-curvature drift, convection, and corotation) associated with each field line. Finally, CRCM uses the bounce-averaged Boltzmann transport equation (17) to calculate the new phase space density, accounting for the bounce-averaged drift velocities as well as losses due to the loss cone and charge exchange with neutral hydrogen [Fok et al., 2001].

$$\frac{\partial \bar{f}_s}{\partial t} + \langle \dot{l}_i \rangle \frac{\partial \bar{f}_s}{\partial l_i} + \langle \dot{\varphi}_i \rangle \frac{\partial \bar{f}_s}{\partial \varphi_i} = -v \sigma_s \langle n_H \rangle \bar{f}_s - \left(\frac{\bar{f}_s}{0.5 \tau_b} \right)_{loss \ cone} \quad (17)$$

where $\bar{f}_s = \bar{f}_s(t, l_i, \varphi_i, M, K)$ is the average distribution function, l_i is the magnetic latitude, φ_i is the local time, M is the first adiabatic invariant, $K = J/\sqrt{8m_o M}$ where J is the second adiabatic invariant, $\langle \dot{l}_i \rangle$ and $\langle \dot{\varphi}_i \rangle$ are the bounce-averaged drift velocities, σ_s is the cross section for the charge exchange of species s with the neutral hydrogen, n_H is the hydrogen density, and τ_b is the bounce period.

2.3.2 Coupling the LFM and CRCM

The CRCM takes an initial distribution of particles and their energies as well as a time-dependent magnetic field with corresponding time-dependent ionospheric height-integrated conductance to execute. After the initial set-up, the CRCM updates the particle densities and energies in the equatorial plane, as well as the magnetic field and height-integrated conductance at specified intervals. To one-way couple the LFM to the CRCM, the same conditions are needed along with the polar cap potential for each update.

Two issues must be addressed when one-way coupling LFM to CRCM: the models are on different grids; and, CRCM assumes symmetric ionospheric polar regions. To handle the differences in grids, the LFM magnetic field is mapped from the distorted spherical grid to a regular spherical grid. The LFM density and temperature are mapped to the equatorial plane. The LFM northern ionospheric conductance and northern polar cap potential are mapped to an evenly space grid of ionospheric magnetic latitudes and local times. Each of these transformations is handled in separate programs.

The initial coupling of LFM and CRCM was done by Fok et al. [2006]. The author used the work by Fok et al. [2006] and redesigned the transformation programs. Under the Fok et al. [2006] coupling, the LFM data were written to unformatted binary files, the author recoded the transformation programs to use the LFM *hdftake* routine to access the LFM data. Then the author streamlined the creation of the new CRCM regular 3-D grid, to which the magnetic field is mapped. This change allows the coupling of any resolution of LFM to CRCM. Finally, the author provided for the automatic creation of every file needed to couple the LFM to the CRCM, removing any operator error issues. The author has considered the symmetry issues, but was unable to complete any definitive work on those issues prior to the writing of this document.

The assumption of symmetric ionospheric polar regions has not yet been addressed. When there is no dipole tilt, only radial solar wind velocities, and the interplanetary magnetic field is parallel-anti-parallel to the magnetic field of Earth, the assumption of symmetry is close.

Thus, under these conditions, the CRCM should be able to reproduce accurate results. When the solar wind velocity differs from radial or the interplanetary magnetic field has a dawn-dusk component, the ionospheric polar regions are no longer symmetric and the assumption has the potential to cause problems. This issue will be discussed further in Chapters 4 and 5, where the CRCM results are discussed with respect to the lack of ring current response.

CHAPTER 3

OBSERVATION-BASED DATA

3.1 Solar Wind Data

Solar wind data were obtained from NASA Goddard Space Flight Center's Space Physics Data Facility – OMNIWeb (http://omniweb.gsfc.nasa.gov/ow_min.html). As outlined in the “About OMNIWeb Data” section, the solar wind data are a collection of magnetic field and plasma data from several satellites (IMP-8, Wind, ACE, and Geotail) (http://omniweb.gsfc.nasa.gov/html/omni_min_data.html). The data are time shifted from the observing spacecraft to the nose of the bow shock, providing a database for solar wind-magnetosphere coupling studies.

The time shifting is based on the assumption that the solar wind observation at the spacecraft is part of a flat plane (called a phase front) that convects at the solar wind speed. The normal (\mathbf{n}) to the phase front is calculated using the magnetic field. Then the solar wind data are propagated by calculating the time (Δt) for the data to move from the satellite to the bow shock nose (see equation (18)) and adding that time to the timestamp of the data.

$$\Delta t = \frac{\mathbf{n} \cdot (\mathbf{R}_d - \mathbf{R}_o)}{\mathbf{n} \cdot \mathbf{v}} \quad (\text{time shift}) \quad (18)$$

where \mathbf{n} is the normal to the phase front, \mathbf{R}_o is the location of the spacecraft, \mathbf{R}_d is the location of the bow shock nose [Farris and Russell, 1994; Shue et al., 1997], and \mathbf{v} is the solar wind velocity.

Once the data are time shifted to the nose of the bow shock, the data are averaged over one-minute bins. This method disregards the fact that some data move faster and overtake other data before the nose of the bow shock. Thus, sharp shocks can be smeared during propagation. This problem has not yet been resolved, and should be considered by any data

users. Overall, though, this method does a consistent and reliable job of solar wind propagation.

Solar wind data downloaded from OMNIWeb include each interplanetary magnetic field component, the magnitude of the solar wind velocity and each of its components, the solar wind density, the Alfvén Mach number, and the sym-H index. The Alfvén Mach number is solar wind speed multiplied by the square root of the solar wind density and divided by the product of twenty and the magnitude of the IMF (http://omniweb.gsfc.nasa.gov/html/omni_min_data.html).

3.2 DMSP Data

The Defense Meteorological Satellite Program (DMSP) has several satellites in polar orbits. The satellites orbit at an altitude of 840 km with an orbital period of about 105 minutes (<http://cindispace.utdallas.edu/DMSP/faq.htm>). The orbits have 96 degree inclinations, which cause the satellites to precess through 360 degrees in a year. The precession of the satellites means the orbits are locked in local time, thus an individual satellite roughly orbits over the same local time in each pass. During 1995 to 2005, the DMSP satellites were F-12, F-13, and F-15 (F-14 did not collect useable data). DMSP F-12 and F-15 orbit through 0930-2130 local time; DMSP F-13 orbits through 0600-1800 local time. For purely southward IMF, the 0600-1800 local time orbit of F-13 allows it to pass close to the expected minimum and maximum polar cap potentials.

On each DMSP satellite is a suite of instruments known as the Special Sensors-Ions, Electrons, and Scintillation (SSIES) thermal plasma analysis package. The SSIES contains a Retarding Potential Analyzer (RPA), an Ion Drift Meter (IDM), a Scintillation meter, and a Langmuir probe (<http://cindispace.utdallas.edu/DMSP/faq.htm>). Each satellite is a 3-axis stabilized spacecraft with the RPA, IDM and Scintillation meter hanging below the satellite pointed in the direction of flight.

The Ion Drift Meter (IDM) is a Faraday cup with a square aperture facing the direction of flight (<http://cindispace.utdallas.edu/DMSP/faq.htm#12>). With a negatively charged repeller grid

to prevent the entrance of electrons, ions enter the IDM and land on one of the four separate plates at the back of the IDM. An imbalance in the number of ions hitting the plates creates a current which can be measured and used with the geometry of the IDM to calculate the cross-track velocities. The IDM can measure cross-track drift velocities of ± 3.0 km/s or less.

Using the cross-track drift velocities (v) and the local magnetic field (B), the electric field (E) due to the plasma motion is calculated ($E = v \times B$). Then the polar cap potential (φ) is the line integral (dl) of the electric field along the spacecraft's trajectory ($\varphi = - \int E \cdot dl$). The University of Texas at Dallas does all the calculations of the cross-track drift velocities, the electric field due to the plasma motion, and the polar cap potential along the spacecraft's trajectory.

The DMSP SSIES data is processed by the University of Texas at Dallas and available on the internet (http://cindispace.utdallas.edu/DMSP/dmsp_data_at_utdallas.html). When accessed, the velocities and polar cap potential of each orbital pass are plotted. Each plot is labeled with the minimum and maximum polar cap potential. For 0600-1800 satellite passes which cross through the 80 degree or higher magnetic latitude, the difference of the reported maximum and minimum polar cap potential provides a good estimate of the total polar cap potential.

3.3 AMIE Data

The Assimilative Mapping of Ionospheric Electrodynamics (AMIE) procedure takes multiple types and sources of ionospheric data and, using statistical information for preconditioning, maps the values for the polar cap potential, ionospheric conductances, ionospheric currents, ionospheric electric fields, Joule heating, and other ionospheric quantities. The AMIE procedure uses ground magnetometer data, electric fields from satellites and radar, currents recorded by radars, and magnetic perturbations as seen by spacecraft [Richmond and Kamide, 1988]. AMIE also uses statistical models of the ionosphere. Once all the data are gathered, AMIE generates an internally consistent pattern of the polar cap potential, electric

field, field-aligned current density, and height-integrated horizontal ionospheric current density at ~110 km altitude as well as height-dependent magnetic perturbations from the data and estimated conductances [Richmond and Kamide, 1988].

Data from AMIE provide a detailed map of the electrodynamics of the ionosphere along with the estimated errors for the maps. The amount of error depends on the type and quality of the data provided along with the statistical model used. When the data are all from ground magnetometers, areas of low conductance cause the electric fields to have large uncertainty, due to the lack of influence the electric fields have on the magnetic perturbations [Richmond and Kamide, 1988]. Thus, AMIE data provides a useful picture of the electrodynamics of the ionosphere. However, sources of data used to generate the AMIE maps limit the quality of the maps.

The AMIE data used in this research are generated by Aaron Ridley at the University of Michigan (<http://amie.engin.umich.edu/>). Ridley's AMIE data are only based on magnetometer readings in the northern hemisphere. When the data were gathered, only 1999-2003 were available, thus those are the years used in this study.

3.4 Ground-based Magnetometer Data

There are many ground-based magnetometers spread over the surface of the Earth. From these magnetometers, indices of magnetic perturbations are calculated for high and mid latitudes as well as at the equator. The sym-H index is a mid-latitude index, which measures the symmetric perturbation of the horizontal component of the Earth's magnetic field (<http://wdc.kugi.kyoto-u.ac.jp/aeasy/asy.pdf>).

The sym-H index is made from 6 ground-based magnetometers. The six stations vary monthly depending on which ones have the best data and where the stations are located. To calculate the sym-H index (<http://wdc.kugi.kyoto-u.ac.jp/aeasy/asy.pdf>), the data from each station has the main geomagnetic field and solar quiet daily variations removed. The variations are removed by using the original data for the international five quiet days in a given month, and

averaging it to a one-minute cadence and fitting it with B-spline functions. Then the B-spline functions are subtracted from the station's original data to leave only the perturbed magnetic field. If data are missing from some of the international five quiet days, the top five acceptable quiet days from the international 10 quiet days are used instead. Once the perturbed field is found, the local station coordinates are transformed to the dipole coordinate system at the location of the station. Finally, the six stations are averaged to a one-minute cadence, and a latitudinal correction is made by dividing the averaged value by the average cosine of the dipole latitude of each station.

The final sym-H index is the symmetric magnetic field perturbations from the ring current, tail current, and dynamic pressure on a one-minute cadence. This index may be used to calculate the rate of energy injection into the ring current once it has been pressure corrected.

3.5 Pressure Correction

To remove the magnetic perturbations caused by sudden changes in the magnetosphere-solar wind pressure balance, the sym-H index is pressure corrected and called sym-H*. Equation (19) is the pressure correction equation for the sym-H index as described by Burton et al. [1975] with constants from O'Brien and McPherron [2000].

$$sym - H^* = sym - H - 7.26\sqrt{10^{21}m_p n u^2} + 11 \quad (19)$$

where m_p is the mass of a proton in kilograms, n is the number density of the solar wind in particles per cubic centimeter, and u is the solar wind speed in kilometers per second. Sym-H* is considered to be made from mostly ring current energy and thus can be used to calculate the rate at which energy is injected into the ring current (ring current injection rate).

3.6 Ring Current Injection Rate

The ring current injection rate (RCIR) is based on the Dessler-Parker-Sckopke (DPS) relation [Dessler and Parker, 1959; Sckopke, 1966], which equates the magnetic perturbation

seen at the center of the Earth to the kinetic energy of the particles of the ring current (see equation (20)).

$$\frac{\Delta B}{B_o} = \frac{-2E}{3E_m} \quad (\text{Dessler-Parker-Sckopke relation}) \quad (20)$$

where ΔB is the magnetic perturbation at the center of the Earth, B_o is the magnetic field at the surface of the Earth, E is the kinetic energy of the particles of the ring current, and E_m is the magnetic energy in the Earth's field above the surface of the Earth [Dessler and Parker, 1959; Sckopke, 1966; Burton et al., 1975; O'Brien and McPherron, 2000]. The pressure-corrected sym-H (sym-H*) is the negative magnetic perturbation at the center of the Earth, thus the DPS relation can be rewritten, equating the sym-H* to the kinetic energy of the particles.

The RCIR is the rate of change of the sym-H*, or the rate at which energy is added to the ring current minus the rate at which energy is lost from the ring current. The main energy loss process in the ring current is charge exchange. As high energy particles drift around the Earth in the inner magnetosphere, atomic hydrogen (low energy) from the upper atmosphere collides with the energetic particles, exchanging charge. The exchange of charge causes the high energy particle to become neutral, which releases it from the magnetic field line on a specific trajectory. The charge exchange also causes the low energy hydrogen to become an ion, trapped on the magnetic field. The release of energy from the charge exchange is an exponential decay and proportional to the density of hydrogen and to the energy of the particle population. Assuming the atomic hydrogen is abundant in the inner magnetosphere (which is most often the case), the rate of energy loss is an exponential decay of the kinetic energy ($E(t) \sim K.E.* e^{-t/\tau}$, where $K.E.$ is the kinetic energy and τ is the decay time).

Thus, to find the RCIR, the perturbation of the magnetic field is sym-H* and taking its time derivative in the DPS relation, equation (21) becomes

$$\frac{dsym - H^*}{dt} = \frac{d}{dt} \left(\frac{2B_o}{3E_m} E(t) \right) = \left(\frac{2B_o}{3E_m} \right) \left(e^{-t/\tau} \frac{dK.E.}{dt} - \frac{E(t)}{\tau} \right) = Q(t) - \frac{sym - H^*}{\tau} \quad (21)$$

$$Q(t) = \frac{dsym - H^*}{dt} + \frac{sym - H^*}{\tau} \quad (\text{Ring Current Injection Rate}) \quad (21')$$

where B_o is the magnetic field at the surface of the Earth, E_m is the magnetic energy above the surface of the Earth, $Q(t)$ represents all the sources for the sym-H*, and τ is the decay time [Burton et al., 1975; O'Brien and McPherron, 2000].

Several studies have shown that $Q(t)$ is proportional to the dawn-dusk interplanetary electric field (IEF) [e.g., Burton et al., 1975; O'Brien and McPherron, 2000]. For this work, $Q(t) = \alpha(\mathbf{v}(t) \times \mathbf{B}(t))$, where $\mathbf{v}(t)$ is the velocity of the solar wind at the time specified, $\mathbf{B}(t)$ is the IMF at the time specified, and α quantifies the geoeffectiveness of the IEF and is determined by finding the slope of the RCIR as a function of IEF.

CHAPTER 4

RESULTS AND DISCUSSION

This work examines two aspects of the interaction of the dawn-dusk component of the interplanetary magnetic field (IMF B_y) with Earth's magnetosphere-ionosphere system. The first section of this chapter discusses the response of the transpolar potential to a B_y -dominant IMF. The second section of this chapter discusses the response of the ring current to a B_y -dominant IMF. Each section discusses the pertinent methodology for the results discussed within that section. An article substantially identical to Section 4.1 has been published in the Journal of Geophysical Research [Mitchell et al., 2010]. Section 4.2 is being prepared and submitted for publication to the same journal at this time.

4.1 Saturation of the Transpolar Potential

The LFM simulation was used to model the transpolar potential as a function of exclusively southward IMF (B_z) and as a function of exclusively dawn-dusk IMF (B_y). The LFM simulation was run with $u_x = -400.0$ km/s, $n = 5.0$ cm⁻³, a sound speed of 40.00 km/s, zero dipole tilt, and a uniform ionosphere with no Hall conductivity. The Pedersen conductivity was uniform and fixed at 5.0, 10.0, or 20.0 mhos. The transpolar potential was calculated by averaging the total potential difference in the northern polar cap of the ionosphere from 1400 Simulation Time (ST) to 1600 ST. The standard deviation was calculated for the total potential difference from 1400 ST to 1600 ST and used to estimate error in the reported values of the transpolar potential. The standard deviations were on the order of 0.0 to 6.0 kV; thus they are difficult to see on some of the plots. The viscous potential was calculated by a linear regression fit for 0.4 to 1.6 mV/m IEF in exclusively negative B_z simulation runs. The reconnection potential was calculated by subtracting the viscous potential from the transpolar potential.

4.1.1 Simulated Response to Large B_z

Simulated transpolar potentials as a function of the magnitude of the Interplanetary Electric Field (IEF) for exclusively southward IMF are plotted in Figure 11. Because the solar wind velocity is held constant in the simulation, increasing the magnitude of the IEF is tantamount to increasing the magnitude of the southward magnetic field. The LFM simulated transpolar potential saturates for large, negative B_z .

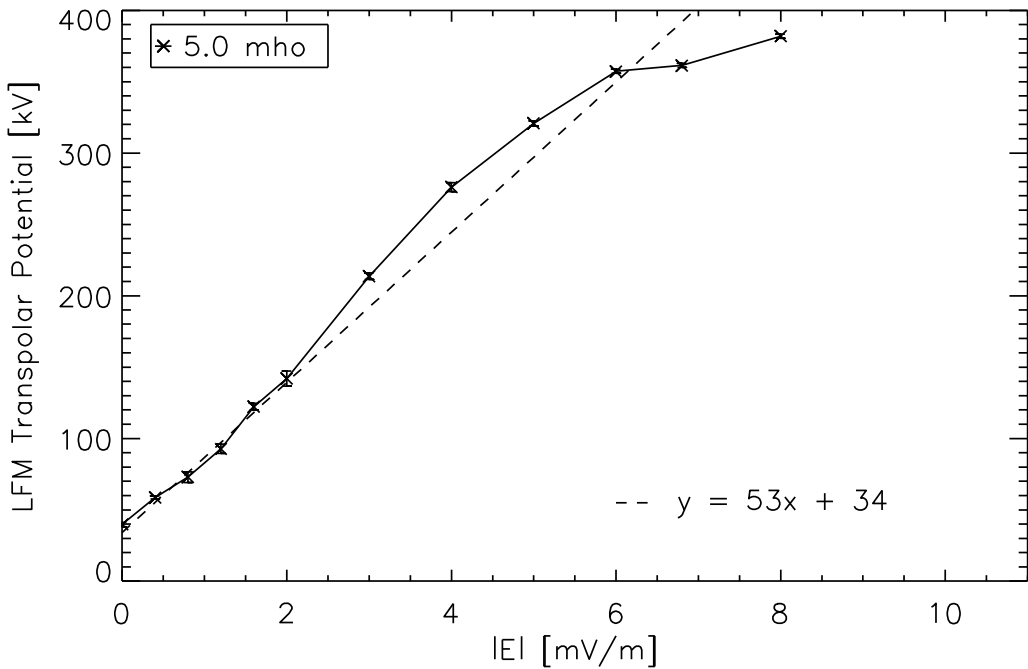


Figure 11. LFM simulated transpolar potential versus IEF (for exclusively southward IMF) for 5.0 mho conductivity. The dash line is an extrapolation of the linear regression calculated between 0.4 and 1.6 mV/m.

Most literature discusses the transpolar potential response as either linear or saturated. For better understanding in this discussion, the transpolar potential is split into 3 regions to allow consideration of the transition. The linear region is between 0.0 and 3.0 mV/m. The transition region, where the slope begins to flatten out and the potential becomes less sensitive

to increases in the IMF, is between 3.0 and 6.0 mV/m. The saturation region is above 6.0 mV/m.

In the low IEF regime (the linear region), the data are fitted using linear regression. The slope of the line has units of length with a value of 53×10^6 m $\sim 8.3 R_E$. Following Lopez et al. [2010], we identify this length as the geoeffective length, that is to say the extent of the solar wind flow that intersects the dayside merging line in the simulation (see section 1.3.3). Burke et al. [1999] determined a geoeffective length using DE 2 electric field observations and found it to be 4.38 to 4.62 R_E in the low IEF regime, while the DMSP drift meter data give a geoeffective length of about $7.4 R_E$ [Lopez et al., 2010]. The smaller observed geoeffective lengths compared to the simulated geoeffective lengths are consistent with the smaller observed transpolar potential compared to the simulated transpolar potential [e.g., Lopez et al., 2009]. The y-intercept of the line ($B_y=B_z=0$) is interpreted to be the viscous potential for these simulated conditions [Lopez et al., 2010]. The simulated viscous potential is ~ 34 kV for a solar wind density of 5.0 cm^{-3} and a speed of 400.0 km/s.

In the transition region (3.0 to 6.0 mV/m), the potential begins to respond nonlinearly to the IEF. Above 4.0 mV/m, the simulated transpolar potential has a decreasing response to the IEF. This is seen through the decrease in the slope between 4.0 and 5.0 mV/m. From 3.0 to 4.0 mV/m, the simulated transpolar potential increases by ~ 62 kV while from 4.0 to 5.0 mV/m it only increases by ~ 45 kV. The transition in the simulated transpolar potential occurs when the potential is between 280 and 320 kV at an IEF between 4.0 and 5.0 mV/m.

In the saturation region (> 6.0 mV/m), the simulated transpolar potential reaches a maximum value of ~ 380 kV. The maximum simulated transpolar potential is large compared to observations of the potential [e.g., Lopez et al., 2009; Lopez et al., 2010]. While the LFM simulation is known to over-predict the transpolar potential by 1.5 to 2 times, it provides accurate trends.

4.1.2 Simulated Response to Large B_y

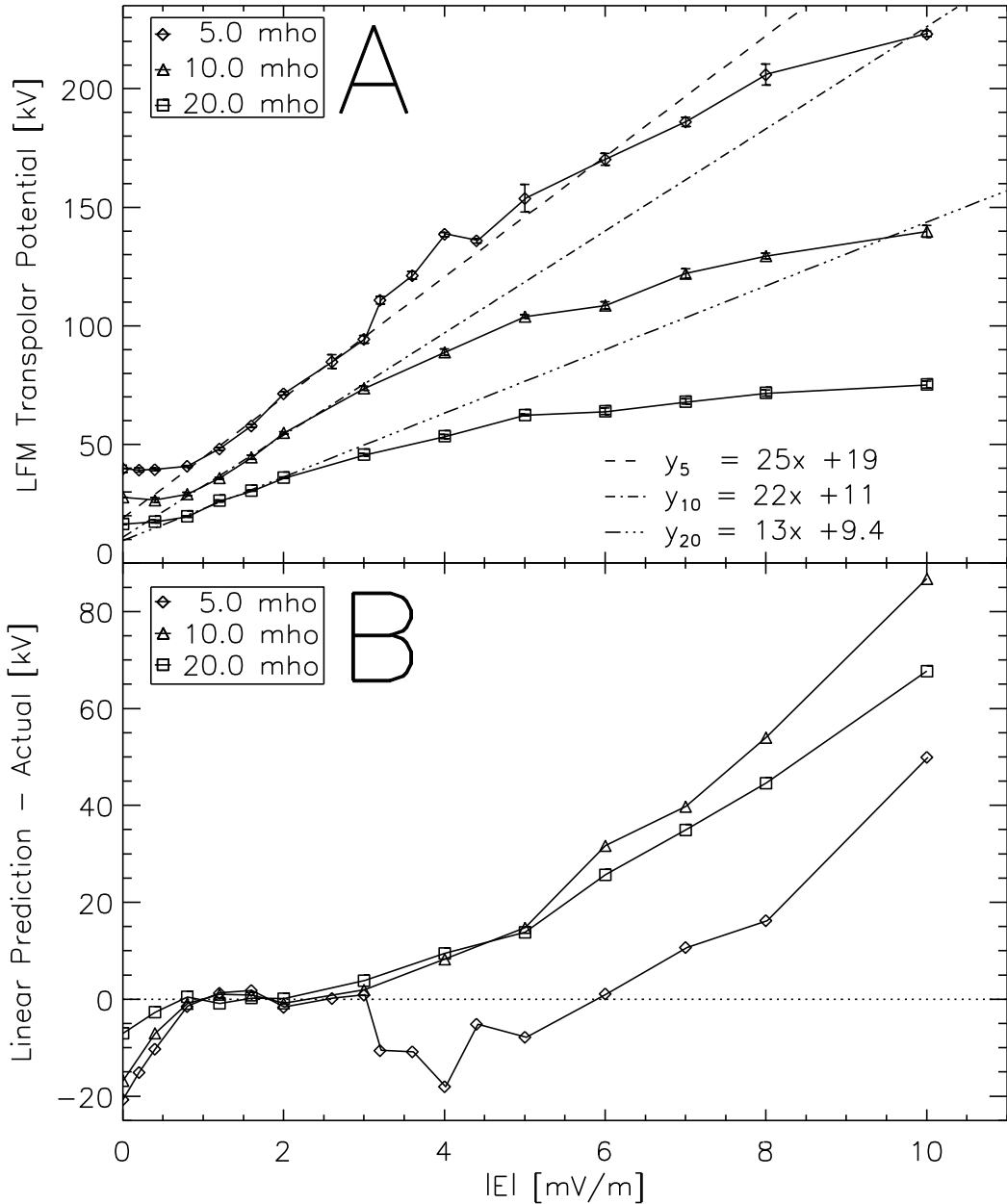


Figure 12. Panel A is LFM simulated transpolar potential versus IEF (for exclusively dawn-dusk IMF) for 5.0, 10.0, and 20.0 mho conductivities. The three broken lines are extrapolations of the linear regressions calculated for each run between 0.8 and 2.0 mV/m. Panel B is the difference between the prediction from the linear fit and the actual LFM simulated transpolar potential versus IEF (for exclusively dawn-dusk IMF) for 5.0, 10.0, and 20.0 mho conductivities.

Simulated transpolar potentials as a function of the magnitude of the IEF for exclusively dawn-dusk IMF are plotted in Panel A of Figure 12. Three different values of ionosphere Pedersen conductivity were used, but for all of the simulation runs, the solar wind speed was held to a constant 400.0 km/s in the negative x -direction, the solar wind density was a constant 5.0 cm^{-3} , and B_z was held constant at zero. Again, because the solar wind velocity is held constant in the simulation, increasing the magnitude of the IEF is tantamount to increasing the magnitude of the magnetic field. The simulation results presented in Figure 12 are computed with varying B_y . It can be seen that the LFM simulated transpolar potential saturates for large $|B_y|$.

As before, the simulated transpolar potential response may be split into three regions. Each conductivity has a slightly different range for the three regions. For 5.0 mho conductivity, the linear region is between 0.0 and 3.0 mV/m, the transition region is between 3.0 and 6.0 mV/m, and the saturation region is above 6.0 mV/m. For 10.0 mho conductivity, the linear region is between 0.0 and 2.0 mV/m, the transition region is between 2.0 and 6.0 mV/m, and the saturation region is above 6.0 mV/m. For 20.0 mho conductivity, the linear region is between 0.0 and 2.0 mV/m, the transition region is between 2.0 and 5.0 mV/m, and the saturation region is above 5.0 mV/m. Saturation occurs for all three conductivities shown.

In the linear region, the data are fitted using linear regression between an IEF of 0.8 mV/m and 2.0 mV/m. The slope of each line has units of length (10^6 m). As before, the slope indicates the extent of the solar wind flow that intersects the dayside merging line in the simulation, although now the projection of the applied electric field to the tilted merging line must be considered using the formula of Kan and Lee [1979] and a 90° clock-angle, which has been shown to be valid in a (different) global MHD simulation [Hu et al., 2009]. Therefore the simulated geoeffective length in the solar wind for 5.0 mho ionospheric conductivity is $25 \times 10^6 \text{ m}/\sin^2(\theta/2)$, $\sim 7.8 R_E$. This is essentially the same simulated geoeffective length in the solar wind that was determined for large, negative B_z .

The y-intercept for each linear regression in B_y , which might be interpreted to be the viscous potential, are significantly smaller than the simulated transpolar potential for zero magnetic field in the solar wind or the viscous potentials reported by Lopez et al. [2010]. It is not clear what the origin of this discrepancy is. Figure 12-A illustrates that the simulated transpolar potential becomes asymptotic for smaller values of B_y -dominated IEF ($< 1.0 \text{ mV/m}$) for all conductivities. The effect of the reconnection potential is only evident when it exceeds the viscous potential. This is in marked contrast to the exclusively southward IMF cases where the viscous potential and the reconnection potential seem to add directly to give the transpolar potential.

In the transition region, the simulated transpolar potential responds nonlinearly to the IEF. Above 4.0 mV/m for 5.0 mho conductivity (3.0 mV/m for 10.0 and 20.0 mho conductivity), the simulated transpolar potential has a decreased response to an increase in the IMF magnitude. This is seen in Panel B of Figure 12, where the difference between the linear prediction and actual simulated transpolar potential versus IEF is plotted. Clearly, all of the simulated transpolar potentials are deviating from the linear response. The transition in the simulated transpolar potential with 5.0 mho ionospheric conductivity occurs when the potential is between 140 and 150 kV at an IEF between 4.0 and 5.0 mV/m . The transitions in the simulated transpolar potentials with 10.0 and 20.0 mho ionospheric conductivities occur when the potentials are between 74 and 89 mV/m and 46 and 53 mV/m , respectively, and the IEF is between 3.0 and 4.0 mV/m .

In the saturation region, the simulated transpolar potential reaches a maximum value of $\sim 210 \text{ kV}$ for 5.0 mho conductivity, $\sim 130 \text{ kV}$ for 10.0 mho conductivity, and $\sim 72 \text{ kV}$ for 20.0 mho conductivity. Both exclusively B_y IEF and exclusively B_z IEF cause the transpolar potential to saturate in the LFM simulation.

4.1.3 Observational Estimates of the Potential During Periods of Large B_y

Observations of the transpolar potential saturation for intervals of B_z -dominated IMF have been confirmed in several studies [e.g., Russell et al., 2001; Hairston et al., 2003; MacDougall & Jayachandran, 2006; Lopez et al., 2009]. The largest values for saturation seen in the DMSP data were ~230 kV [Lopez et al., 2009]. No previous study has come to light which investigates whether the observed transpolar potential also saturates for large B_y -dominated IMF.

For this study, 98 intervals were identified between January 1999 and December 2003. Intervals were selected if: the magnitude of B_y was larger than 5.00 nT; B_z was between -1.00 and +4.00 nT with a majority of it being positive; and, the B_z was mainly positive for the preceding 4 hours. The criteria limiting B_z guarantee that the intervals are ones in which the ionosphere is stable prior to the IMF becoming B_y -dominant.

DMSP transpolar potentials were obtained for each interval. The differences between the maximum and minimum reported values were used to calculate the transpolar potentials along the DMSP orbital track. For each selected solar wind interval, any DMSP satellite pass occurring during the interval was recorded. For each pass, the IEF is averaged over the pass interval. However, how well the DMSP spacecraft potential represents the actual potential depends on how close the spacecraft came to the actual maximum and minimum of the ionospheric potential during the pass.

Figure 13 contains three Super Dual Auroral Radar Network (SuperDARN) plots illustrating plasma convection in the polar region. Each plot has one or two DMSP satellite trajectories superimposed in black. The approximate location of the satellite during the 2-minute interval during which the data for the convection map was collected is shown in yellow. The SuperDARN plots give approximate locations of the maximum (+) and minimum (x) polar cap potentials, and one can see that in these DMSP passes during these periods the estimates of the polar cap potential should be good. Table 1 lists the values of the DMSP maximum and

minimum potentials and the transpolar potential as well as the average AMIE transpolar potential, B_y , and transverse IEF for the same interval.

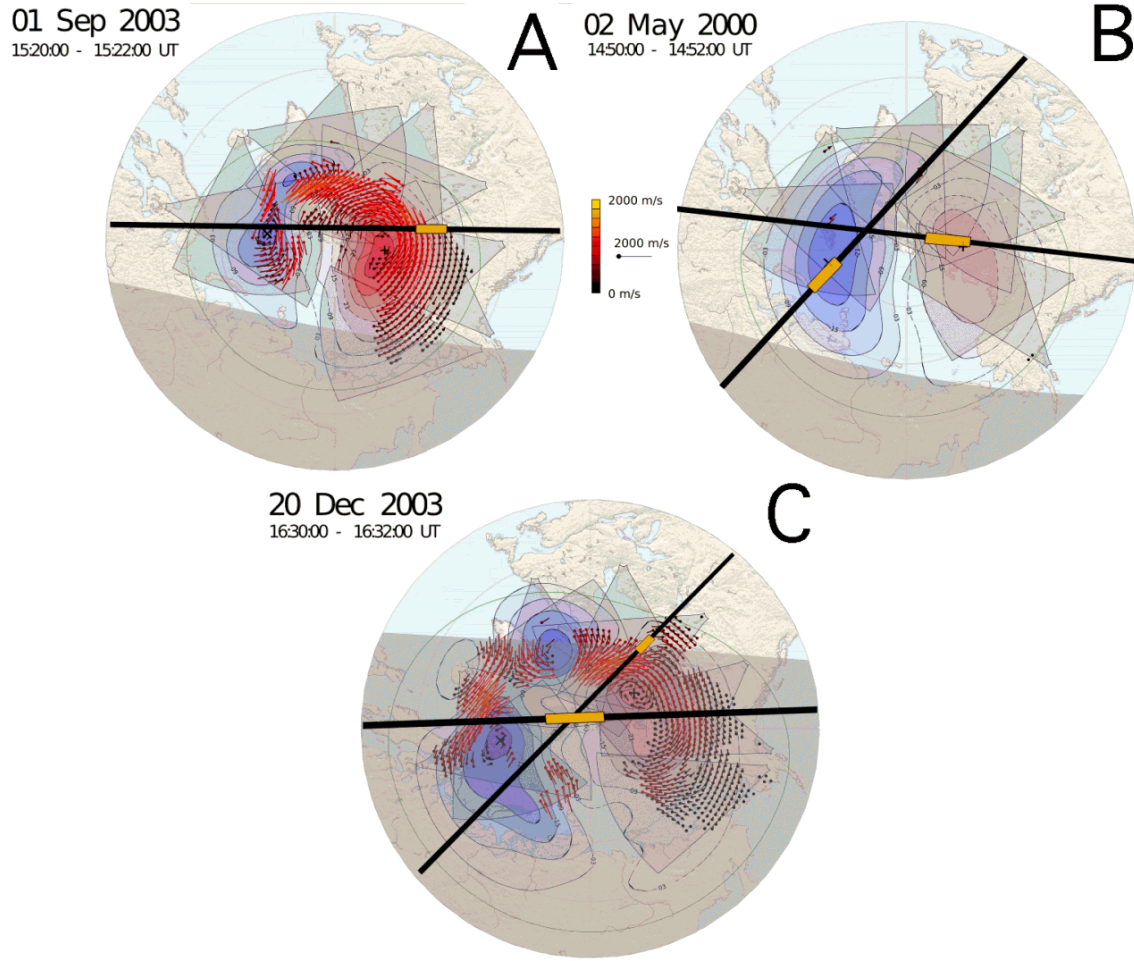


Figure 13. Three SuperDARN convection maps with DMSP satellite passes superimposed. The maximum (+) and minimum (-) polar cap potentials are marked on each map. Panel A is the SuperDARN convection map for September 1, 2003, between 1520 and 1522. It has an F-13 pass superimposed, with its position between 1520 and 1522 marked in yellow. Panel B is the SuperDARN convection map for May 2, 2000, between 1450 and 1452. It has an F-13 and an F-15 pass superimposed, with each satellite position between 1450 and 1452 marked in yellow. Panel C is the SuperDARN convection map for December 20, 2003, between 1630 and 1632. It has an F-13 and an F-15 pass superimposed, with each satellite position between 1630 and 1632 marked in yellow.

Table 1. Measurements by DMSP satellites during selected intervals of B_y -dominant IMF. Average AMIE, B_y , and $|E_t|$ for the same selected intervals.

Year	Month	Day	Sat.	Start Time	End Time	Max. Pot.	Min. Pot.	DMSP Trans. Pot.	Avg. AMIE Trans. Pot.	Avg. B_y	Avg. $ E_t $
2003	9	1	F13	1506	1530	43.0	-32.4	75.5	77.7	-8.37	3.95
2000	5	2	F13	1439	1503	70.1	-32.6	103	92.4	-11.27	7.27
2000	5	2	F15	1443	1509	7.6	-38.7	46.3	93.2	-11.23	7.23
2003	12	20	F15	1616	1642	57.8	-41.3	99.2	82.4	-14.96	6.97
2003	12	20	F13	1619	1643	49.0	-51.6	101	85.1	-14.39	6.72

For September 1, 2003, the DMSP F-13 satellite passes near both the maximum and minimum potentials as given by SuperDARN (Figure 13-A). The DMSP transpolar potential for this pass is 75.5 kV. For May 2, 2000, the DMSP F-13 satellite passes over the reported maximum potential (DMSP maximum = 70.1 kV) while the DMSP F-15 satellite passes over the reported minimum potential (DMSP minimum = -38.7 kV) (Figure 13-B). The DMSP F-13 transpolar potential for this pass is 103 kV. For December 20, 2003, the DMSP F-13 and F-15 satellites pass near both the maximum and minimum potentials (Figure 13-C). For this pass, the DMSP F-13 transpolar potential is 101 kV and the DMSP F-15 transpolar potential is 99.2 kV. Comparing the DMSP transpolar potentials and their average B_y , the change from 75.5 kV to 103 kV corresponds to a change in the average solar wind B_y from -8.37 nT to ~ -11.25 nT. So comparing the September 1, 2003 pass to the May 2, 2000 pass there is a 27 kV difference in ionospheric potential corresponding to a 2.88 nT difference in the average solar wind B_y . In contrast, comparing the May 2, 2000 pass (103 kV) to the December 20, 2003 pass (101 kV), there is a -2 kV difference in potential for a 3.43 nT difference in the average B_y . These three cases suggest saturation of the potential for large B_y . Other reasons might be suggested for these changes if the incidents were isolated.

These incidents are not isolated though, when a larger sample size is considered. The larger sample of DMSP transpolar potentials are plotted as a function of the transverse IEF and maximum AMIE transpolar potentials are plotted as a function of 1 mV/m bins of transverse IEF in Figure 14. The 10,301 minutes of AMIE data are sorted by corresponding transverse IEF and

separated into 1 mV/m bins. The diamonds in Figure 14 indicate the maximum AMIE transpolar potentials as a function of their transverse IEF bins. Clearly, the maximum AMIE transpolar potentials saturate. The bars in Figure 14 plot the 105 DMSP F-13 transpolar potentials as a function of their average transverse IEF. The DMSP transpolar potential stays within the envelope of maximum AMIE transpolar potential. The low potential values in the DMSP data are from passes where the satellites did not enter the regions of highest or lowest potential due to the skewing of the polar cap by B_y -dominated IMF [Heppner, 1977]. The DMSP transpolar potentials also show a trend for saturation, though the number of passes at the higher transverse IEF is low.

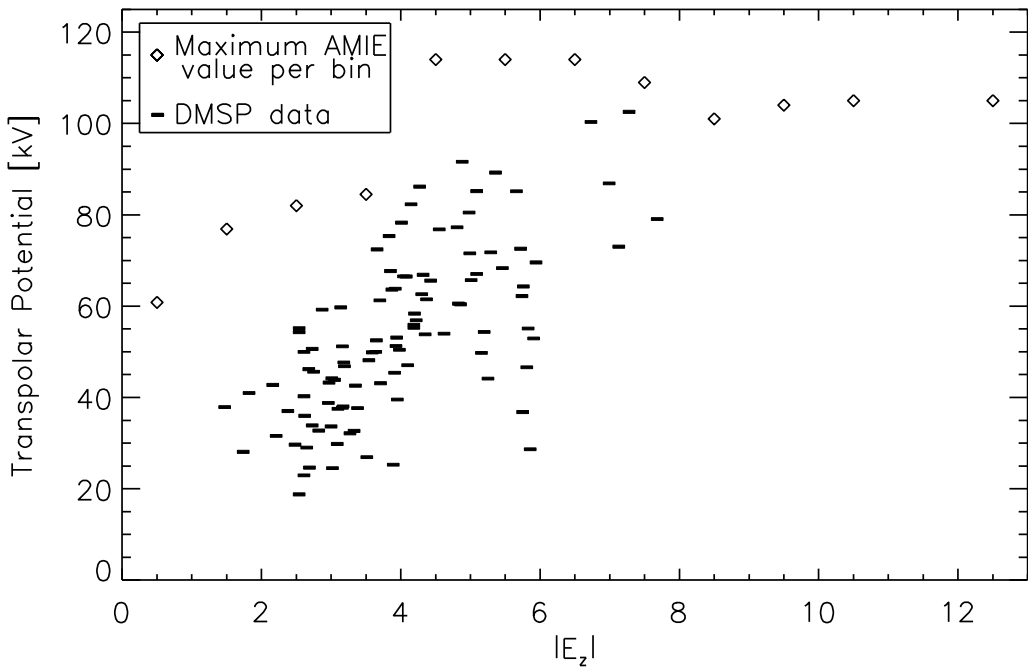


Figure 14. Maximum AMIE transpolar potential (diamonds) for each 1 mV/m bin versus 1 mV/m bins of B_y -dominant transverse IEF and DMSP transpolar potentials (dashes) versus B_y -dominant transverse IEF.

The transpolar potential saturates for sufficiently large magnitude B_y -dominated IEF. The transition from a linear dependence on transverse IEF to a saturated potential occurs

between 4 and 5 mV/m, as seen in Figure 14. The maximum transpolar potential is 114 kV for AMIE data and 103 kV for DMSP data. Both values are between half and two-thirds the simulated transpolar potential for 5.0 mho conductivity, which is the approximate scaling between the LFM potentials and observed potentials for dominantly southward IMF.

4.1.4 Discussion

Transpolar potential saturation has been shown in each of the three cases above: simulated B_z -dominated IEF; simulated B_y -dominated IEF; and, observed B_y -dominated IEF. Returning to the explanations of transpolar potential saturation, the results are considered with respect to the Region 1 current (R1) model [Siscoe et al., 2002 a&b], Alfvén Wing (AW) model [Ridley, 2007; Kivelson & Ridley, 2008], and Magnetosheath Force Balance (MFB) model [Lopez et al., 2010].

The R1 model predicts the saturation of the transpolar potential to occur at the same potential value for any given IEF, if the conductivity, solar wind density, and solar wind velocity all have the same value. This prediction may be verified using the LFM simulation results with 5.0 mho conductivity. In the exclusively B_z IEF case, the simulated transpolar potential becomes nonlinear between 4.0 and 5.0 mV/m at 280 to 320 kV. In the exclusively B_y IEF case, the simulated transpolar potential becomes nonlinear between 4.0 and 5.0 mV/m at 140 to 150 kV. Therefore, according to Ohm's law, the current generated in one case is different from the other case. It cannot be the current that limits the transpolar potential since these examples represent significantly different values of the Region 1 current.

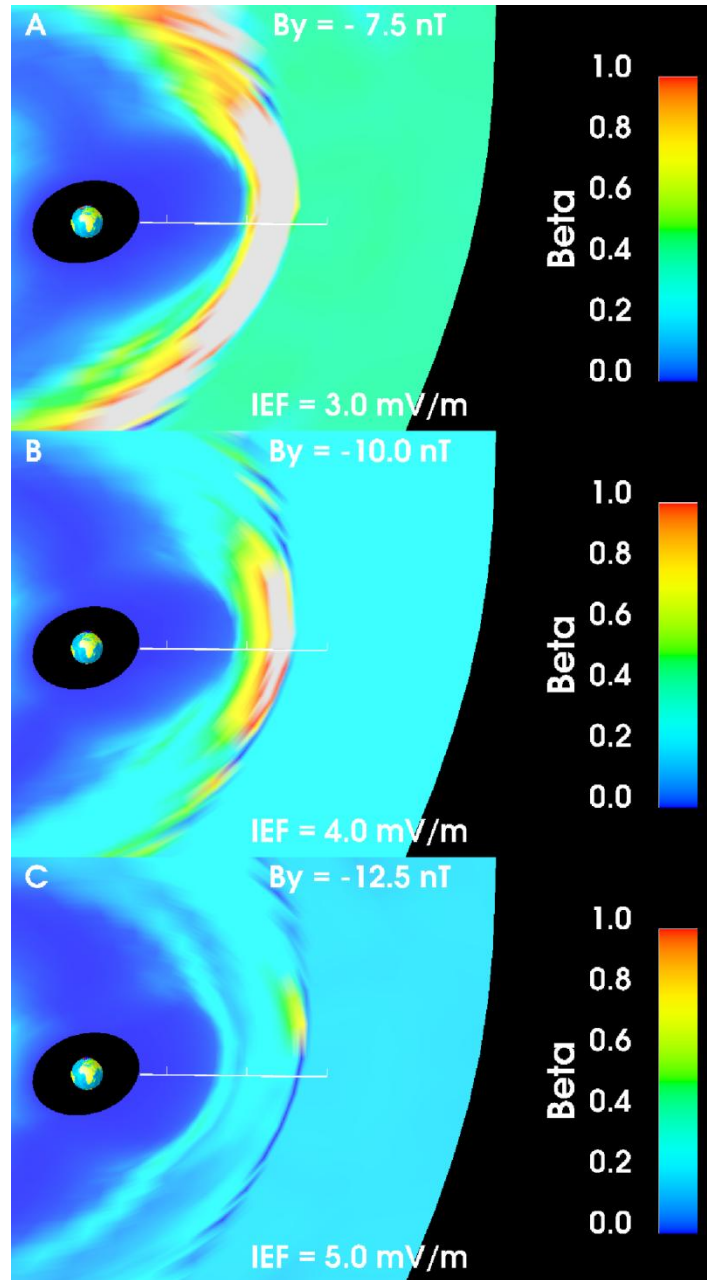


Figure 15. LFM simulated β for 5.0 mho conductivity mapped to a plane tilted 45 degrees from the North Pole toward dusk and perpendicular to the expected merging line. The scale is from 0 to 1; gray indicates β greater than 1. Panel A has solar wind $B_y = -7.5 \text{ nT}$ and IEF = 3.0 mV/m. Panel B has solar wind $B_y = -10.0 \text{ nT}$ and IEF = 4.0 mV/m. Panel C has solar wind $B_y = -12.5 \text{ nT}$ and IEF = 5.0 mV/m.

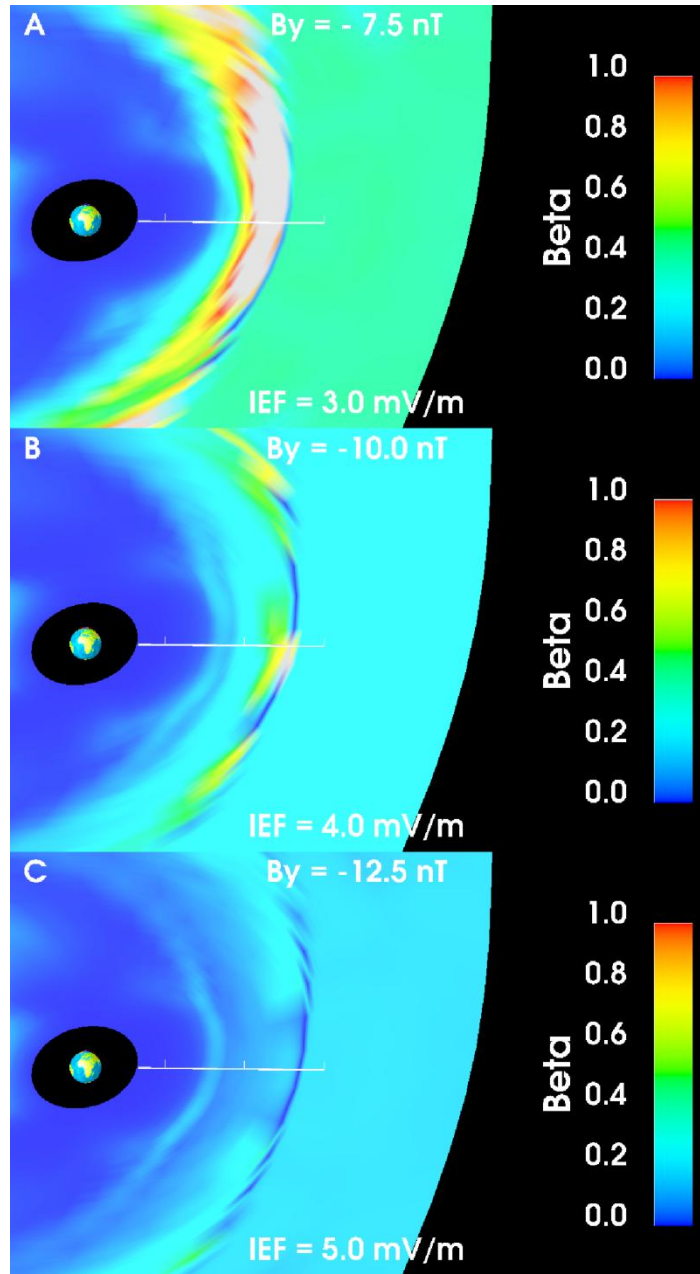


Figure 16. LFM simulated β for 20 mho conductivity mapped to a plane tilted 45 degrees from the North Pole toward dusk and perpendicular to the expected merging line. The scale is from 0 to 1; gray indicates β greater than 1. Panel A has solar wind $B_y = -7.5$ nT and IEF = 3.0 mV/m. Panel B has solar wind $B_y = -10.0$ nT and IEF = 4.0 mV/m. Panel C has solar wind $B_y = -12.5$ nT and IEF = 5.0 mV/m.

This is not to say the Region 1 current does not affect the reconnection potential. The Region 1 current does affect the shape of the magnetopause and the thickness of the

magnetosheath. Figures 15 and 16 depict a plane of the magnetosheath tilted 45 degrees from the North Pole toward the dusk side of the Earth for the 5.0 and 20.0 mho conductivity cases, respectively. Examining the C panels, the magnetosheath for the 20.0 mho case (Figure 16) is thicker and blunter than the 5.0 mho case (Figure 15). This thickening and blunting occurs through erosion of the magnetic field on the day side. The increased conductivity, even with slightly smaller transpolar potentials, provides an increased current, which erodes the dayside magnetic field as suggested by Siscoe et al. [2004]. Merkin et al [2005] and Lopez et al. [2010] suggest that greater erosion provides a larger region of magnetosheath over which the plasma flow may be diverted, thereby shortening the extent of the solar wind flow that intersects with the merging line.

The AW model predicts the saturation of the transpolar potential to occur after an hour of low Alfvén mach number (<4) while the Alfvén Mach number remains less than 4. An Alfvén Mach number of 4 occurs for a solar wind velocity of 400 km/s, a solar wind density of 5 cm^{-3} , and an IMF of 10 nT. The concurrent IEF is 4 mV/m, which is close to the value where the simulated transpolar potentials begin to respond nonlinearly. However for the event on December 20, 2003 presented in Figure 13, the average Alfvén Mach number (5.2) was greater than four, and the solar wind was not steady for an hour to allow the formation of the Alfvén wing. Yet the event is an example of a saturated potential. Thus this study finds no strong evidence in favor of the AW model. Moreover, the AW model does not explain why only a fraction of the electric field in the Alfvén wing is actually communicated to the ionosphere. Ridley [2007] suggests that only 10% of the length of the dayside magnetopause is undergoing reconnection, but Borovsky et al. [2008] presents evidence that dayside merging occurs in the BATSRUS simulation code over a much greater extent.

The MFB model predicts the saturation of the transpolar potential to occur as β_{ms} approaches 1 at the nose of the magnetosheath, and it also explains why even for small IMF values the total potential drop across the width of the magnetosphere is not imposed on the

ionosphere. In the simulations using exclusively dawn-dusk IEF, the 5.0 mho conductivity simulated transpolar potential becomes nonlinear between 4.0 and 5.0 mV/m, or 10.0 and 12.5 nT. Figure 15 depicts 3 planes tilted 45 degrees from the North Pole toward dusk in which β_{ms} has been plotted. These planes are normal to the expected merging line [Moore et al., 2002]. All three images are from the same simulation time in the runs of 5.0 mho conductivity; only the magnitude of B_y has changed in each. The color bar is set between 0 and 1; the gray areas are β_{ms} greater than 1. Panel A of Figure 15 has a B_y of -7.5 nT corresponding to an IEF of 3.0 mV/m. β_{ms} is clearly greater than 1 for a large area of the magnetosheath. Panel B of Figure 15 has a B_y of -10.0 nT corresponding to an IEF of 4.0 mV/m. β_{ms} is greater than 1 at the nose of the magnetosheath but does not extend into the flanks. Panel C of Figure 15 has a B_y of -12.5 nT corresponding to an IEF of 5.0 mV/m. β_{ms} is less than 1 throughout the magnetosheath. These results support the MFB prediction of magnetosheath behavior during the transition from linear to nonlinear responses in the transpolar potential. Figure 16 follows the same structure as Figure 15 for the 20.0 mho conductivity case and provides additional support to the MFB model. In the exclusively B_y IEF simulated cases, the 20.0 mho conductivity simulated transpolar potential becomes nonlinear between 3.0 and 4.0 mV/m, or 7.5 and 10.0 nT. Again, the β_{ms} is greater than 1 for -7.5 nT (3.0 mV/m), but it reaches 1 at approximately -10.0 nT (4.0 mV/m) and is much less than 1 by -12.5 nT (5.0 mV/m).

The MFB model appears to be predictive for both B_y -dominant IEF and B_z -dominant IEF. The difference in the two IEF cases is in the geometry of the dayside merging line. The geometry of the B_y -dominant IMF dayside merging region is more complex than the geometry of the B_z -dominant IMF dayside merging region [Moore et al., 2002]. Bent crossing the bow shock, the B_y -dominant IMF merges with the magnetosphere at a 45 degree angle to the X-Y plane at the nose of magnetopause, and goes from pole to pole, partially encircling the cusp regions. The effects of this geometry are captured by the Kan and Lee [1979] clock-angle dependence, which has been shown to correctly predict the reconnection potential in other

simulations [Hu et al., 2009]. Incorporating this factor, the simulated geoeffective length in the solar wind is the same for exclusively southward as well as dawn-dusk orientations for the same solar wind conditions. This adds support to the argument that the geoeffective length is established by the forces in the magnetosheath diverting flow from the dayside merging line.

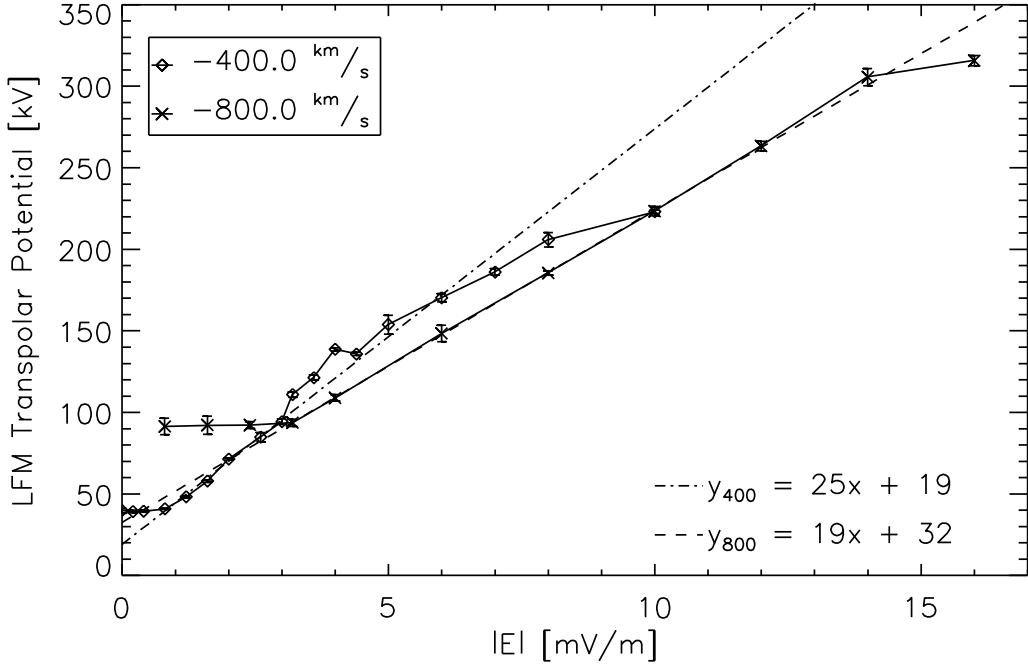


Figure 17. LFM simulated transpolar potential versus exclusively B_y -dominant IEF for 5.0 mho conductivity and solar wind $u_x = -400.0 \text{ km/s}$ and -800.0 km/s . The broken lines are extrapolations of the linear regression calculated between 0.4 and 1.6 mV/m for $u_x = -400.0 \text{ km/s}$ and between 3.2 and 8.0 mV/m for $u_x = -800.0 \text{ km/s}$.

In addition, a brief examination of the role of solar wind speed in establishing the potential lends strong support to the MFB model. Figure 17 is a plot of the simulated transpolar potential for solar wind speeds of 400.0 km/s and 800.0 km/s. Doubling the solar wind speed changes the asymptotic behavior in the linear regime. The total potential does not rise above the viscous value until the reconnection portion of the potential is larger than the viscous value. This behavior merits further investigation, but that is beyond the scope of the current investigation.

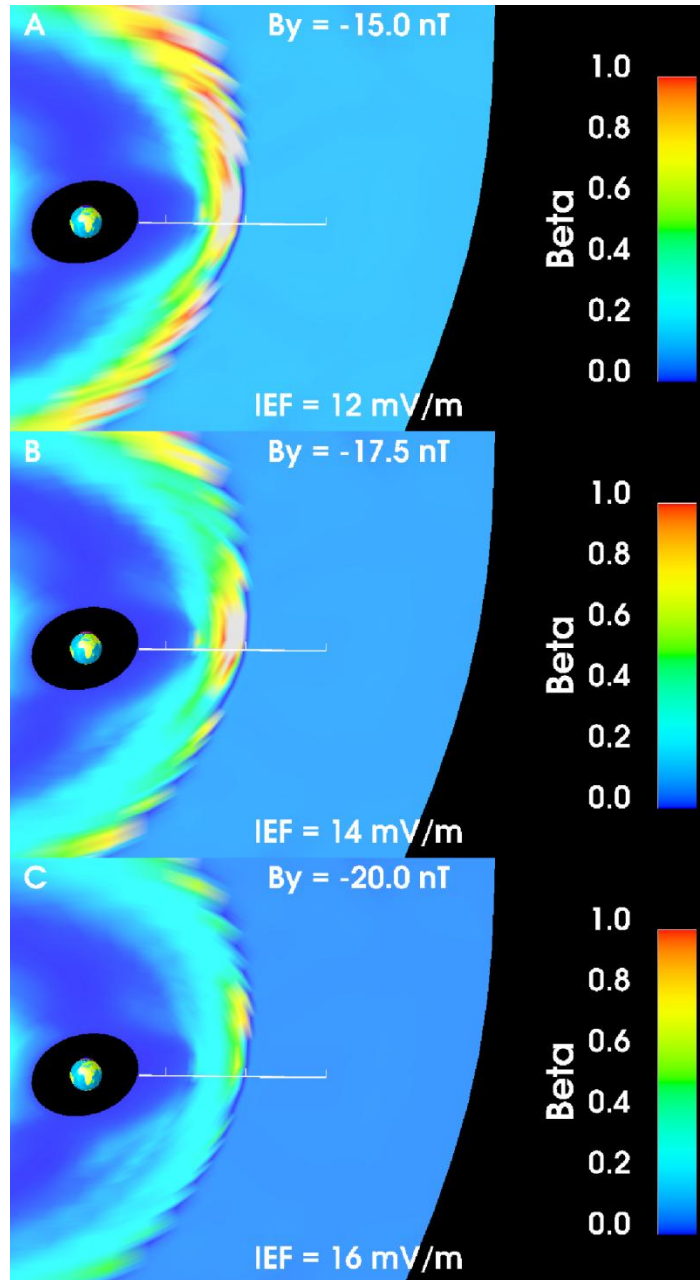


Figure 18. LFM simulated β for 5.0 mho conductivity and solar wind $u_x = -800.0$ km/s mapped to a plane tilted 45 degrees from the North Pole toward dusk and perpendicular to the expected merging line. The scale is from 0 to 1; gray indicates β greater than 1. Panel A has solar wind $B_y = -15.0$ nT and IEF = 12.0 mV/m. Panel B has solar wind $B_y = -17.5$ nT and IEF = 14.0 mV/m. Panel C has solar wind $B_y = -20.0$ nT and IEF = 16.0 mV/m.

While the viscous potential increases with increasing solar wind speed, the simulated geoeffective length ($19 \times 10^6 \text{ m}/\sin^2(\theta/2)$, $\sim 6.0 R_E$) in the linear regime decreases so that the reconnection potential is fairly independent of velocity. It has been shown to be consistent with the MFB model since a larger solar wind velocity produces larger magnetosheath plasma pressures and gradient, thus producing a greater diversion of the magnetosheath flow and a smaller geoeffective length in the solar wind. Doubling the solar wind speed also extends the linear regime due to the increase in the magnetosheath plasma pressure. Figure 18 presents the β for the 800.0 km/s case in Figure 17. As can be seen, β across the magnetosheath is larger for larger solar wind speed, and the behavior of the potential (not saturating until a larger IMF is reached) is consistent with the larger β .

4.1.5 Conclusions about Transpolar Potential Saturation

This study examined the response of the transpolar potential to B_y -dominant IEF. Saturation of the transpolar potential was found in both simulation results and observations. The DMSP data and AMIE results confirm the LFM simulation prediction. The transpolar potential saturates for B_y -dominant IEF. The value of the saturation potential is consistent with the Kan and Lee [1979] reconnection electric field and the same simulated geoeffective length found for exclusively southward IMF by Lopez et al [2009a]. Of the models examined, the results seem to be most consistent with the Magnetosheath Force Balance model.

4.2 Lack of Ring Current Response

4.2.1 Observational Estimates of Ring Current Injection Rate During Periods of Large B_z

Observations of linear response of the ring current injection rate (RCIR) have been discussed in several studies [e.g., Russell et al., 2001; Lopez et al., 2009], but to give a reference point to discussions about the RCIR, the RCIR for intervals of B_z -dominant IMF is plotted against the dawn-dusk interplanetary electric field (IEF E_y) in Figure 19. To make Figure 19, 31 B_z -dominant IMF intervals are identified between January 1999 and December 2003.

The interval selection criteria are: $|B_z| \geq 1.5 * |B_y|$; $|B_y| < 5$ nT; and, B_z had to be negative. The 31 intervals are a sample of the data, not an exhaustive list (see appendix A).

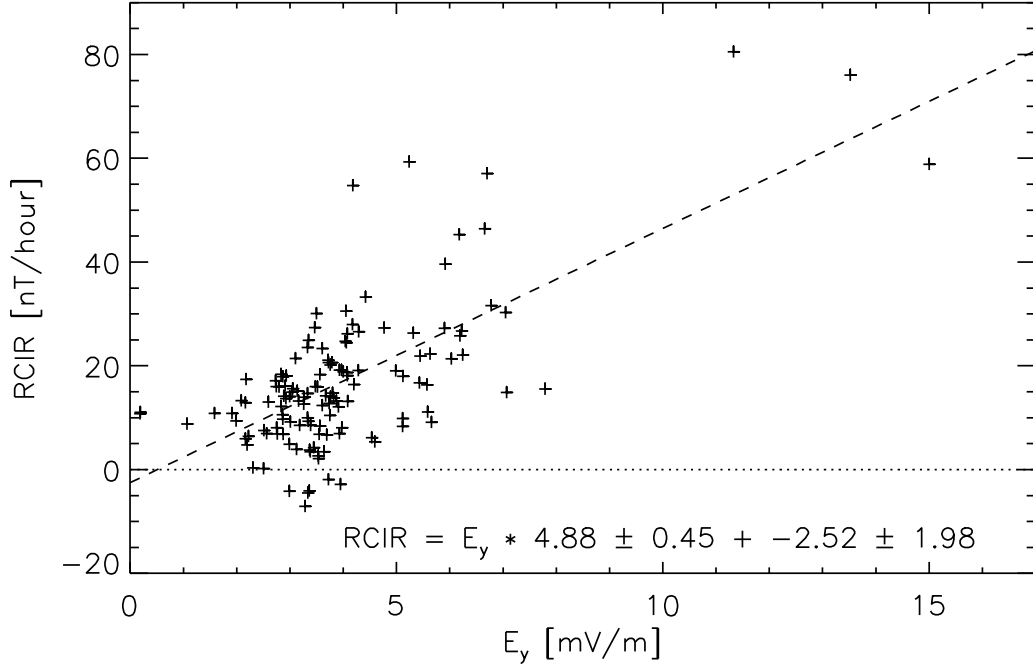


Figure 19. The RCIR for periods of B_z -dominant IMF versus the IEF E_y . The least-square fit is plotted in the dashed line with the equation in the bottom right hand corner of the plot.

While the transpolar potential saturates for these intervals (not shown), the RCIR does not saturate, but continues to grow linearly with the B_z -dominant IEF. The lack of saturation in the RCIR even after the transpolar potential saturated had been a conundrum for several years [Russell et al., 2001]. The conundrum was resolved by Lopez et al. [2009], when they discussed the mechanisms for the continued growth of the RCIR. They showed that the interchange instability and the location of reconnection in the magnetotail allow low PV^Y flux tubes to continue to energize the ring current when magnetospheric convection is saturated.

The measurement of the effect the IEF has on the inner magnetosphere is known as geoeffectiveness. The slope of the linear fit between the IEF and RCIR is a measure of geoeffectiveness. The larger the slope the more geoeffective the coupling is and the greater

the amount of energy that is transferred into the inner magnetosphere. For B_z -dominant IMF, the slope of the linear fit is found to be $4.88 (3.6 \times 10^9 \text{ m})^{-1}$.

4.2.2 Simulated Ring Current Response to Large B_z

The use of simulations provides a method for studying a part of the magnetosphere even when data are unavailable for the location. Before a simulation is deemed reliable for new investigations, it needs to be confirmed through known phenomena. Thus, the LFM-CRCM one-way coupled simulation (see Chapter 2 for background) is run using the 5.0 mho conductivity LFM simulation runs discussed in section 4.1. The CRCM is initialized and updated with the LFM simulated magnetic field, equatorial temperatures and densities, ionospheric potentials, and ionospheric conductivities every 5 minutes of simulation time (ST).

The initialization of the CRCM run occurs at 6:38 ST in the LFM simulation. The CRCM simulation then runs another 9 hours and 6 minutes of ST with updates every 5 minutes. Every 20 seconds, the CRCM reports the amount of energy inside the $6.6 R_E$ boundary. The simulated sym-H index is calculated from this energy. Taking one hour averages of the simulated sym-H centered on the half hour and pressure correcting the resulting simulated Dst, the simulated RCIR is calculated using the Burton et al. [1975] equation.

The simulated RCIR for exclusively southward B_z is plotted against the dawn-dusk IEF in Figure 20. Each column of symbols (+) is a single CRCM simulation run, where the spread of the symbols comes from the different slopes of the simulated Dst throughout the CRCM run. The smallest values in the columns correspond to the period between when the IMF has turned southward and when the ring current response is first seen, and the period toward the end of the simulation run when the Dst index is flattening (see Figure 22).

The simulated RCIR grows with the B_z -dominant IEF, and does not saturate even though the transpolar potential does saturate for the same simulation runs (Figure 11). The slope of the linear fit is $2.63 (3.6 \times 10^9 \text{ m})^{-1}$, 54% as geoeffective as the observational data. While the slopes are different, the trends are similar between the observations and the simulations.

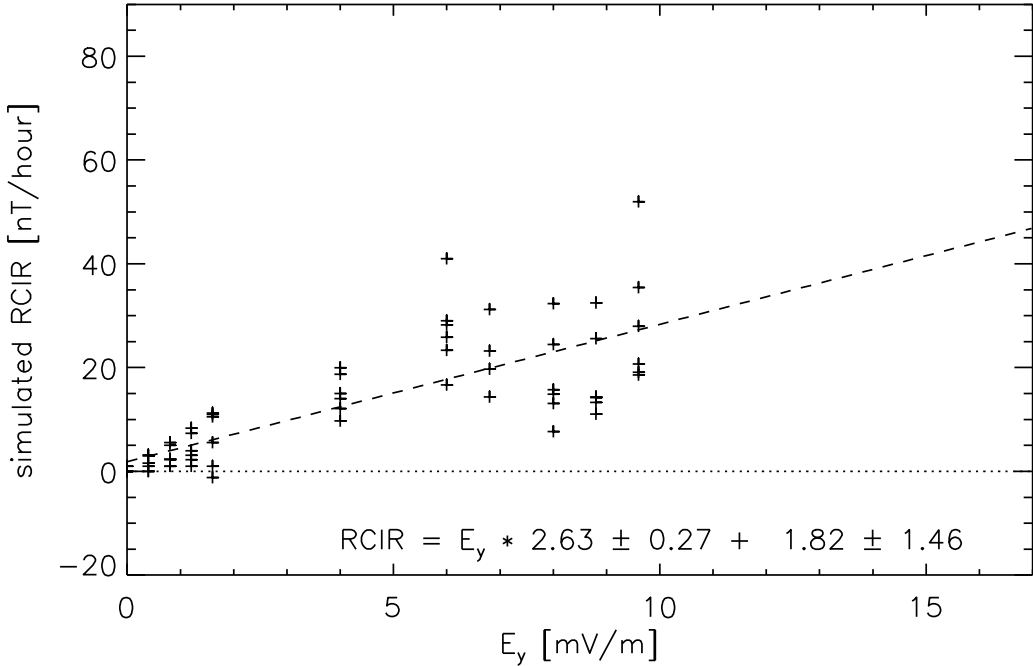


Figure 20. CRCM simulated RCIR versus IEF E_y for exclusively southward B_z LFM simulations. The least-square fit is plotted in the dashed line with the equation in the bottom right hand corner of the plot.

To further confirm that the simulation provides qualitatively similar results to observations, an observational case study and an idealized simulation run are compared in Figures 21 and 22. The observational data have an average B_y of 0 nT, B_z of -18 nT, solar wind speed of 392 km/s, and solar wind density of 5.6 cm^{-3} . The average AMIE transpolar potential is 104 kV. The sym-H is decreasing most of the time, reaching -164 nT. The RCIR ranges from -14.9 to -31.6 nT/hour between 10:00 and 14:00 UT. The idealized LFM-CRCM simulation run had a B_y of 0 nT, B_z of -20 nT after 8:00 ST, a solar wind speed of 400 km/s, and a solar wind density of 5 cm^{-3} . The simulated sym-H decreases during the southward IMF, reaching -80 nT. The RCIR ranges from -7.7 to 32.3 nT/hour between 9:00 and 14:00 ST. While the observed sym-H and simulated sym-H are not the same strength, they have similar trends, and the RCIR have similar ranges for both cases.

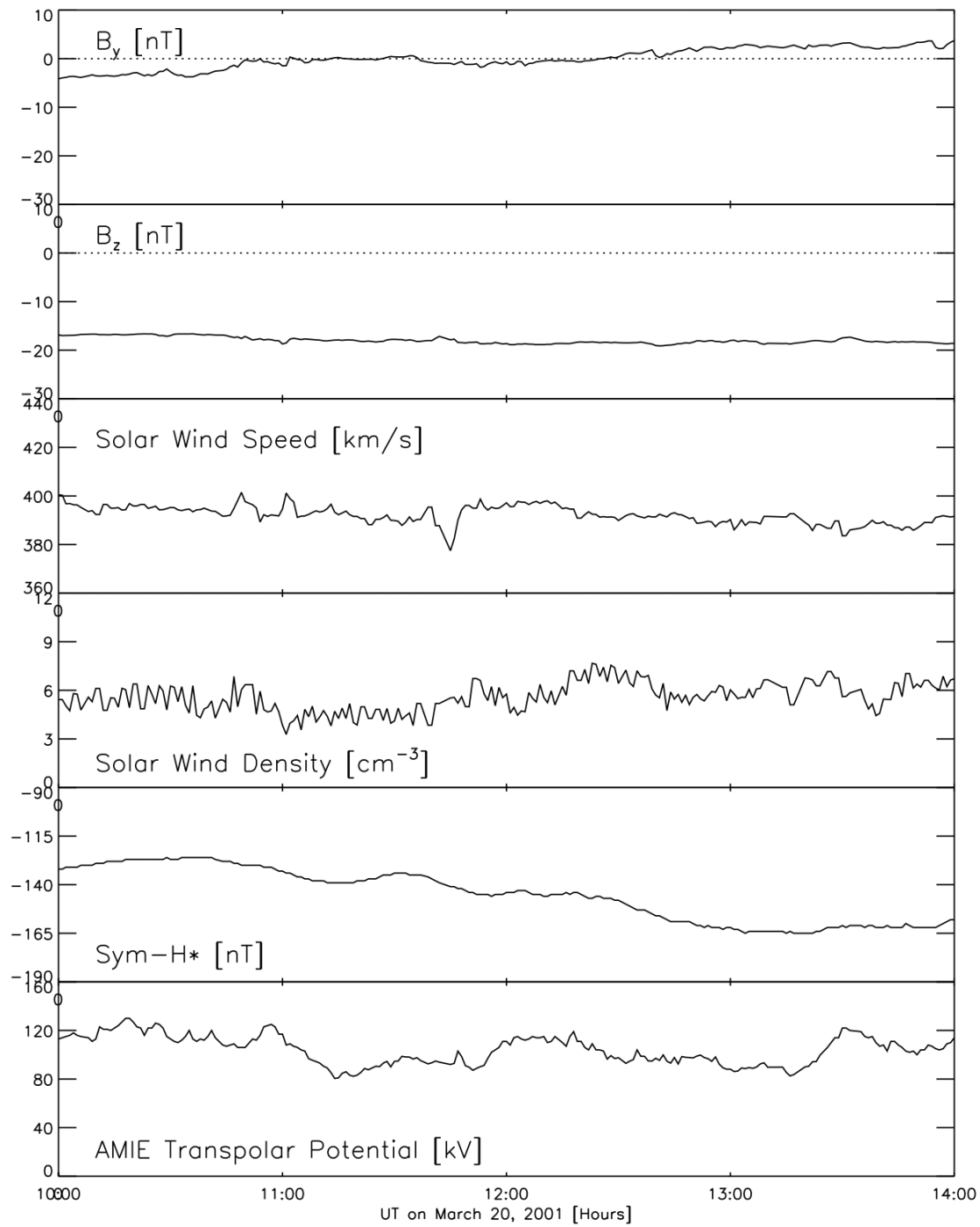


Figure 21. Solar Wind data, Sym-H*, and AMIE transpolar potential on March 20, 2001

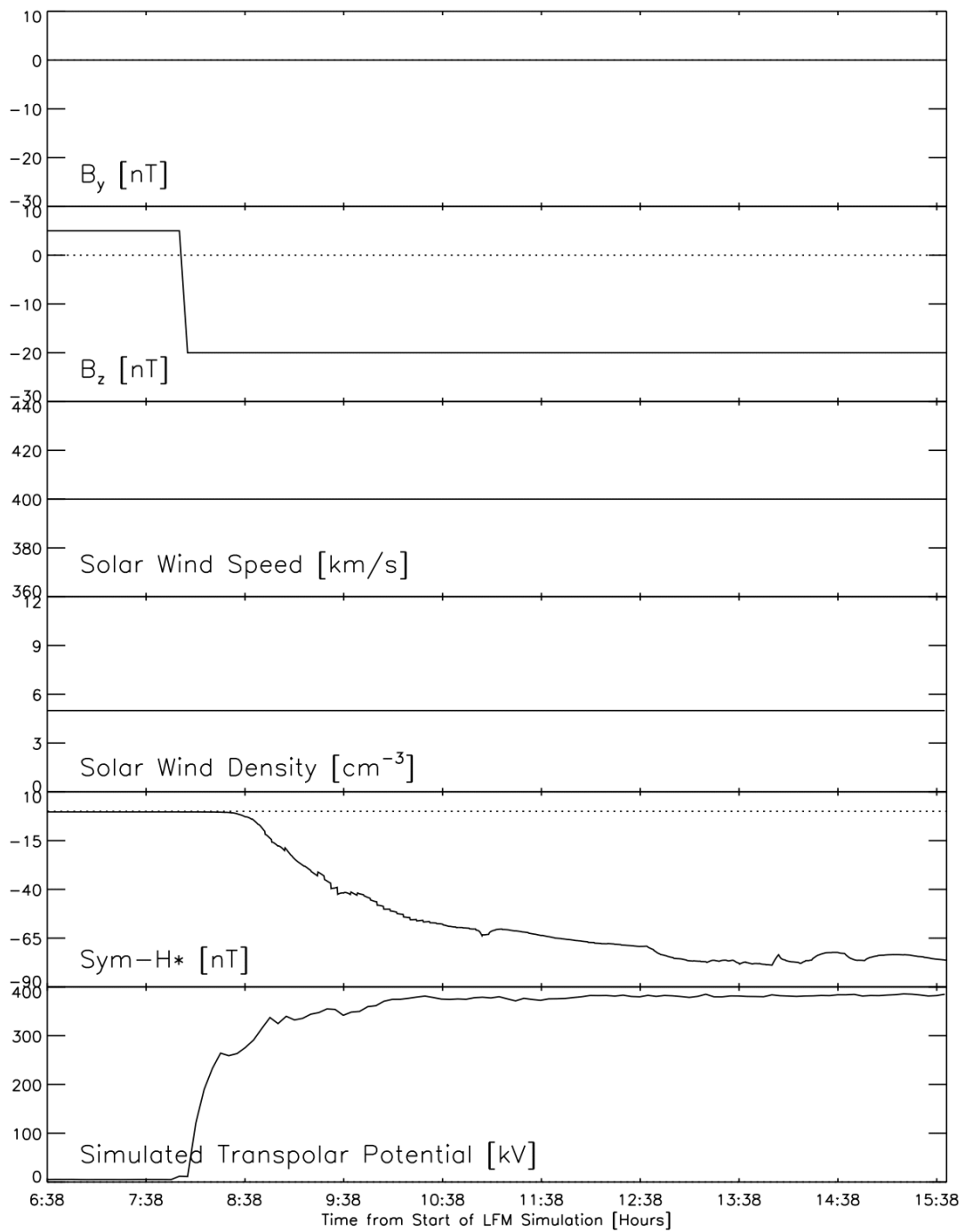


Figure 22. Idealized Solar Wind used as LFM input, CRCM simulated Sym-H, and simulated Transpolar Potential for $B_z = -20$ nT

These results confirm the ability of simulation to model the trends of the ring current for large B_z . They also suggest some examination of large B_y effects on the ring current may be possible with the LFM-CRCM simulation.

4.2.3 Observational Estimates of Ring Current Injection Rate During Periods of Large B_y

Using the 98 intervals identified in section 4.1.3, the one minute OMNI data are hourly averaged and the RCIR are calculated from the pressure-corrected, one-hour-averaged sym-H data. The RCIR for B_y -dominant IMF versus the magnitude of the north-south IEF ($|E_z|$) are plotted in Figure 23.

B_y -dominant IMF is significantly less geoeffective. The slope of the linear fit is 0.69 $(3.6 \times 10^9 \text{ m})^{-1}$, one-seventh the slope of the B_z -dominant intervals. This decrease in the ring current response indicates almost no energy is being transferred from the solar wind into the inner magnetosphere. But the transpolar potential is still saturating for these data (Figure 14).

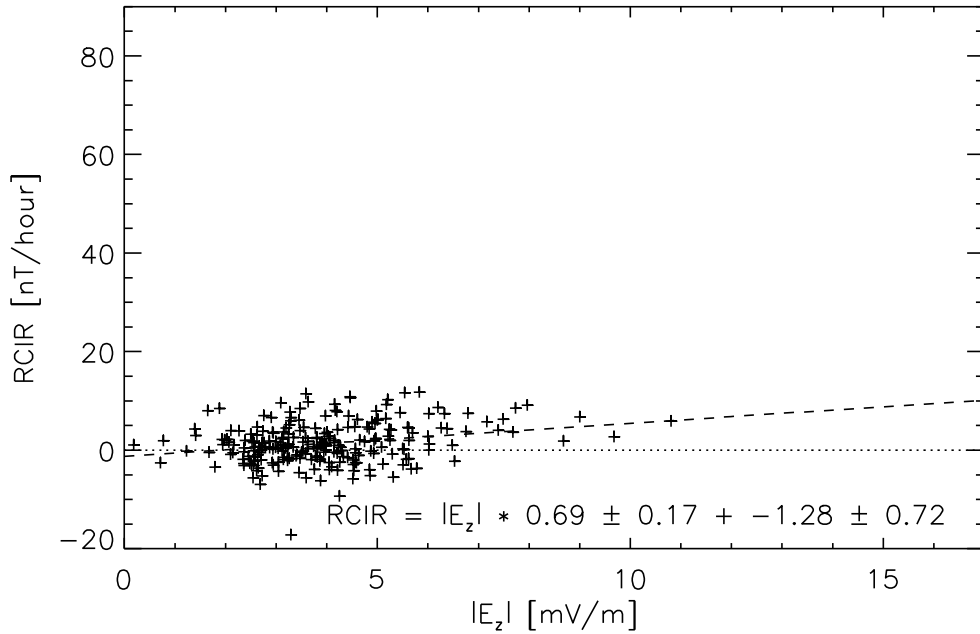


Figure 23. The RCIR for periods of B_y -dominant IMF versus the IEF $|E_z|$. The least-square fit is plotted in the dashed line with the equation in the bottom right hand corner of the plot.

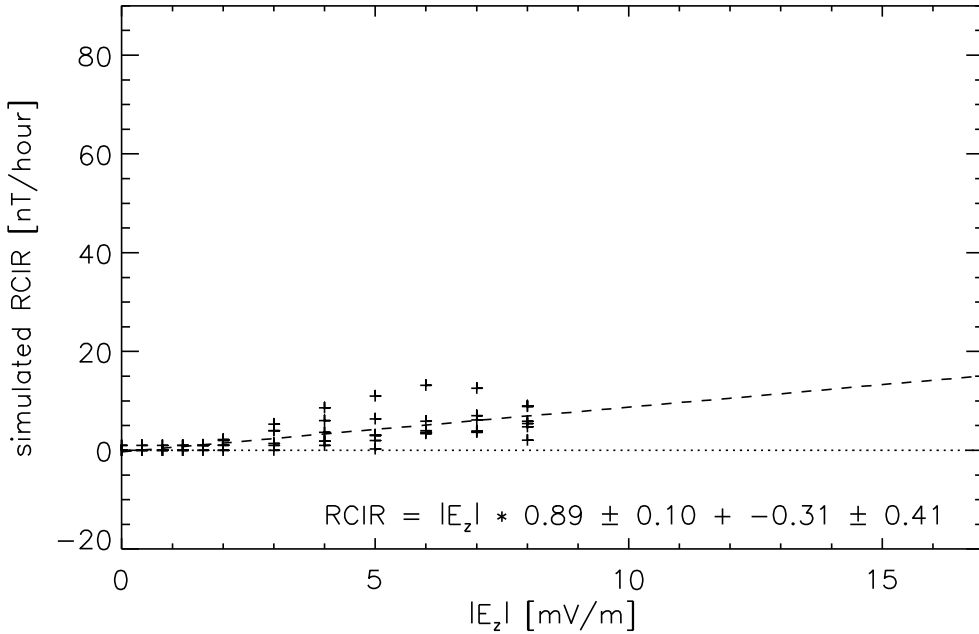


Figure 24. CRCM simulated RCIR versus IEF $|E_z|$ for exclusively dawn-dusk IMF LFM simulations. The least-square fit is plotted in the dashed line with the equation in the bottom right hand corner of the plot.

4.2.4 Simulated Ring Current Response to Large B_y

The simulated RCIR for exclusively dawn-dusk IMF is plotted against the north-south IEF in Figure 24. Each column of symbols (+) is a single CRCM simulation run, where the spread of the symbols comes from the different slopes of the simulated Dst throughout the CRCM run. The smallest values in the columns correspond to the period between when the IMF has turned southward and when the ring current response is first seen, and the period toward the end of the simulation run when the Dst index is flattening.

Exclusively dawn-dusk IMF is significantly less geoeffective. The slope of linear fit is $0.89 (3.6 \times 10^9 \text{ m})^{-1}$, which is a third of the slope for the exclusively southward IMF simulation results. There is a pronounced decrease and possibly a lack of ring current response to the IEF.

There is also a pronounced difference in the qualitative similarities between the observation and simulation data for B_y -dominant IMF compared to those for B_z -dominant IMF. The observational data show less of a response to the north-south IEF than the simulation data do. To compare the observations and simulations for B_y -dominant IMF in greater depth, solar wind and sym-H data for two observational cases and a simulation case are plotted in Figures 25, 26, and 27, respectively.

4.2.5 Three Case Studies

Figure 25 presents the dawn-dusk and north-south IMF, the solar wind speed and density, sym-H*, and the AMIE transpolar potential for August 1-2, 2002. At the end of August 1 the IMF turned strongly southward. As can be seen, sym-H* responded and decreased steadily until just before 0500 UT on August 2. At that point B_z increased to zero and, just after 0600 UT, B_z turned solidly northward and pretty much stayed that way throughout the time presented in Figure 25. Coincident with the northward turning of the IMF, the ring current (as reflected by sym-H*) began to recover. This, of course, is the expected response and so rather unremarkable. What is of interest is that throughout the period of northward IMF, B_y was steadily large and negative, and there seems to be little evidence of it driving the ring current. At approximately 1230 UT there was a sudden decrease in the solar wind density which produced a step change in sym-H*, but the ring current seems to have continued its smooth recovery, despite the -11 nT IMF B_y and a polar cap potential estimated from AIME to be close to 100 KV. This is consistent with data from DMSP F13 (not shown), which indicate that northern transpolar potential was at least 85 kV and stable from 1402 UT to 1428 UT.

The second case occurred on October 21-22, 1999, and Figure 26 presents the dawn-dusk and north-south IMF, the solar wind speed and density, sym-H*, and the AMIE transpolar potential. At about 0220 UT, a shock arrived with a large positive B_y field that by 0500 UT had rotated to a strongly negative B_y field. This strong, negative B_y field persisted for the next 17 hours, during which the IMF was mostly northward. The AIME data indicate that the

ionospheric potential was large and generally near the saturation value of 120 kV reported above [Mitchell et al., 2009]. However, during this period of significant ionospheric convection by an intense IMF, there was no ring current response as determined from sym-H*. On the other hand, the three brief southward periods in the IMF from 0600 UT to 2300 UT each produced a noticeable and equally brief negative deflection in sym-H*. And at 2330 UT, the sudden southward turn of the IMF produced an equally pronounced intensification of the ring current.

The third case study is a 5 mho conductivity LFM-CRCM simulation run for a solar wind speed of 400 km/s and a solar wind density of 5 cm^{-3} , as seen in Figure 27. The simulation begins with the dawn-dusk IMF at 0 nT and the north-south IMF at +5 nT. At 0800 ST, the IMF turns such that the north-south IMF goes to 0 nT and the dawn-dusk IMF becomes -17.5 nT. All input is then held steady for the rest of the simulation, ~7.5 hours. Forty minutes after the magnetic field turns, the CRCM simulated sym-H begins to decrease, reaching ~ -20 nT at 1540 ST. The response of the simulation to the dawn-dusk IMF is directly opposed to what is observed. While the ring current does fluctuate during periods of dawn-dusk IMF, the fluctuations follow changes in the north-south IMF and solar wind speed and density, not changes in the dawn-dusk IMF. Thus, conclusions based on the simulation of dawn-dusk IMF must be considered suspect until the disparities can be explained.

The tracking of the sym-H* with changes in the solar wind speed and pressure also indicates that the pressure-correction algorithm is not removing all of the changes in the ring current due to solar wind dynamic pressure fluctuations. This may account for some of the spread in the RCIR versus north-south IEF plot in Figure 23. Further investigations of the pressure correcting algorithm may be of some use to the community, though it does not hold a high priority at this time.

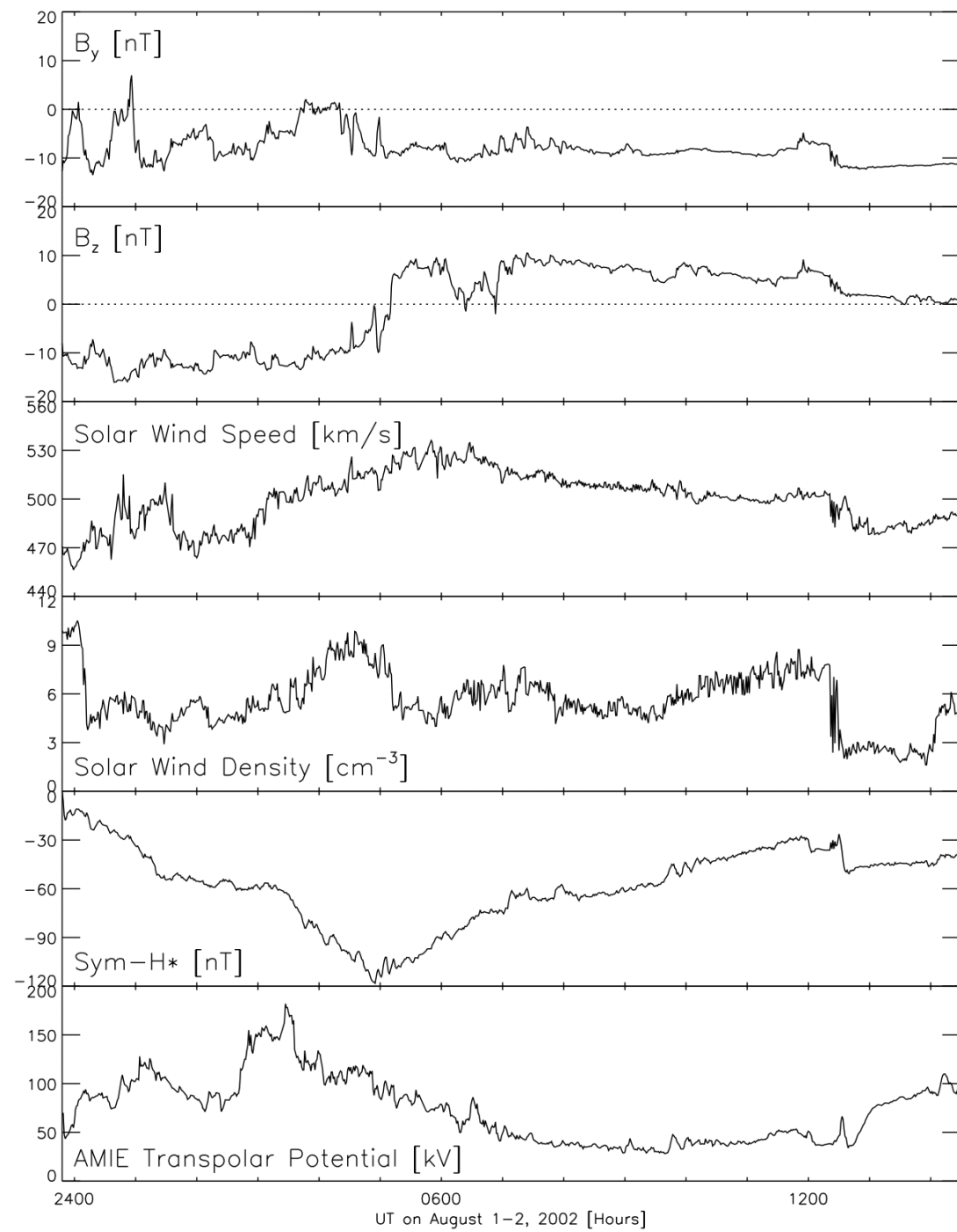


Figure 25. Solar wind data, Sym-H*, and AMIE transpolar potential on August 1-2, 2002

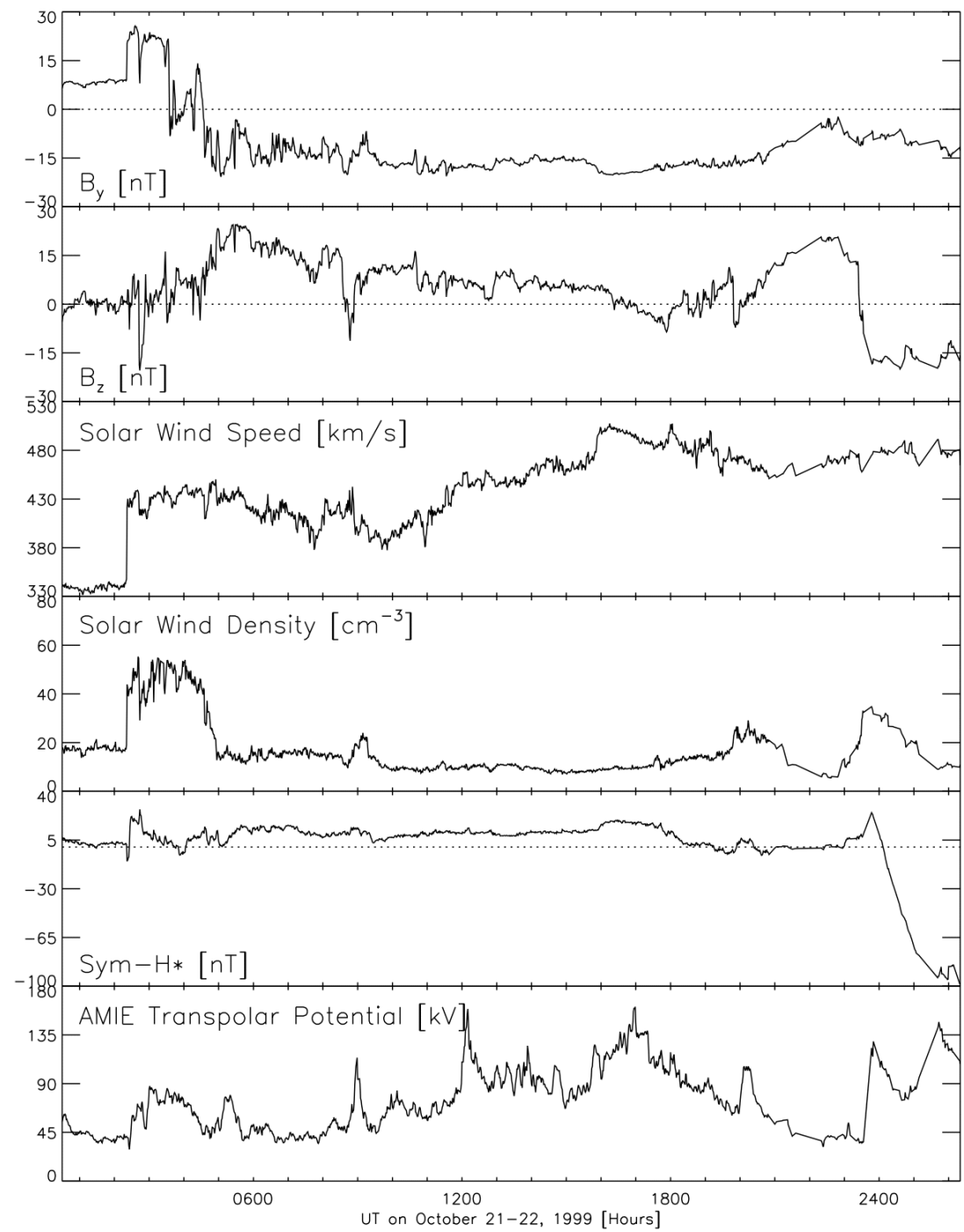


Figure 26. Solar wind data, Sym-H*, and AMIE transpolar potential on October 21-22, 1999

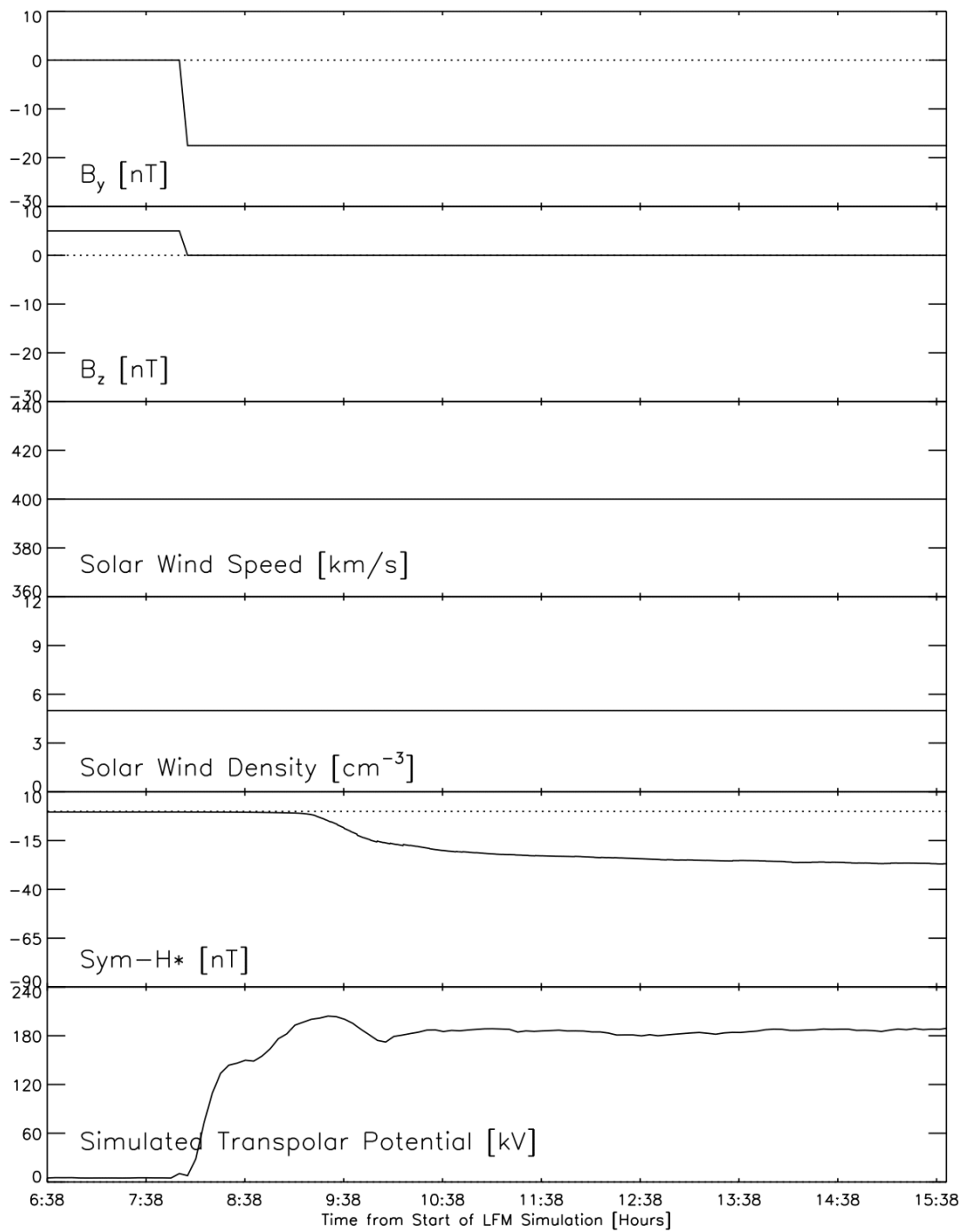


Figure 27. Idealized Solar Wind used as LFM input, CRCM simulated Sym-H, and simulated Transpolar Potential for $B_y = -17.5$ nT

4.2.6 Discussion

The data presented above show that B_y -dominant IMF does not lead to significant, or even detectable, ring current injection. The statistical evidence showed almost no dependence of the ring current injection rate on the dawn-dusk IMF, and the two observational case studies presented both showed that the ring current did not respond to B_y -dominant IMF, even though the response to even transient southward IMF was evident. On the other hand, significant ionospheric convection is present for B_y -dominant IMF, with a total transpolar potential of around 100 kV at times. Thus not all ionospheric convection driven by the solar wind will produce inner magnetospheric convection.

B_y -dominant IMF-driven convection produces lobe cell convection (see section 1.2.3). This results in ionospheric convective cells that have some closed convection entirely within the open field line regions [e.g., Eriksson et al., 2003]. While there are theoretical arguments to question whether ionospheric sunward convection is actually possible on open field lines [Hill, 1994], MHD simulations [Crooker et al., 1998] suggest that this is the case. The MHD simulations suggest sunward ionospheric convection is decoupled from anti-sunward, high-altitude flow as the field lines nominally connecting the two regions encounter the merging line diffusion region and lose their identity (see section 1.2.3). Thus one might hypothesize lobe cell convection driven by the solar wind with the sunward component having no inner magnetospheric counterpart. This hypothesis would warrant further investigation.

Another feature of ionospheric convection driven by B_y -dominant IMF is asymmetric convection cells with the potential across one cell being larger than the potential across the other (see section 1.2.3). Crooker et al. [1998] showed that this potential disparity was located in the lobe cell. The convection represented by this potential is then entirely on open field lines, producing no inner magnetospheric convection. One can evaluate the reliability of this statement and the MHD simulations by examining the event on August 1-2, 2002. The DMSP

F13 data show that in the 20 minutes centered on 1414 UT, during which the polar cap was traversed, the observed potential maximum was 65.3 kV, and the potential minimum was -20.1 kV. This yields about 45 kV of asymmetric potential which by Crooker et al. [1998] is located in the lobe cell. This leaves about 40 kV of symmetric potential which is attributed to the combined merging and viscous cells. But the viscous potential is about 20 kV [e.g., Lopez et al., 2010] (see section 1.2.1), leaving a merging potential of 20 kV to drive convection in the inner magnetosphere. Given that each mV/m of electric field (for southward IMF) in the solar wind produces 49 kV of potential in the ionosphere from reconnection [Lopez et al., 2010], this implies that the convection in the closed field line region was being driven with the equivalent of 0.5 mV/m in the solar wind, or a IMF B_z of -1 nT for a solar wind speed of 500 km/s, as was recorded on August 1-2, 2002. This explains the lack of a significant ring current response.

The kind of flux circulation driven by merging with the dawn-dusk IMF is quite different from the Dungey cycle. Crooker et al. [1998] noted that the reconnection line in the tail was along the flanks, not the center of the tail. Such geometry is unlikely to produce the low PV^γ flux tubes that are essential to the transport of plasma into the inner magnetosphere to energize the ring current. Combined with the relative lack of convection in the closed field line region in the inner magnetosphere, there should be no significant ring current response to large dawn-dusk IMF, even if there is a significant amount of ionospheric convection. Thus space weather applications that use sym-H or Dst as an indicator of activity may miss periods when there is significant energy deposition into the ionosphere, but no ring current response.

4.2.7 Conclusions about the Lack of Ring Current Response

Large dawn-dusk IMF does not lead to any significant or detectable changes in the ring current. The ring current response for purely dawn-dusk IMF does not seem to match its response for purely southward IMF in any form. From a basic understanding of magnetic storms, this leads to the conclusion that the lack of ring current response to large dawn-dusk IMF is due to the lack of strong magnetospheric convection in the inner magnetosphere. Yet,

large dawn-dusk IMF drives significant ionospheric convection. The large transpolar potential produced by large dawn-dusk IMF is generated mostly by lobe cell convection. The remaining ionospheric convection does not seem to be enough to generate a ring current, either through overall enhanced convection, or through the creation of a reconnection region that creates low PV^Y flux tubes that can inject ring current particles into the inner magnetosphere. Thus using ionospheric convection as a measure of magnetospheric convection is not accurate during large dawn-dusk IMF. The decoupling of the ionospheric and inner magnetospheric convection during large dawn-dusk IMF posits several new questions, including where energy deposition is occurring and how one can determine the geoeffectiveness of such events. These results could have significant impact for the prediction of space weather.

CHAPTER 5

CONCLUSIONS AND FUTURE WORK

Energy is transferred into the magnetosphere of Earth through merging of magnetic fields (Dungey cycle and lobe cell convection) and through momentum transfer across the magnetopause (viscous interactions). The interactions of the interplanetary magnetic field (IMF) with the magnetic field of Earth have been studied extensively with regard to the role of the north-south component of the IMF. The role of the dawn-dusk IMF is less well known.

The role of the dawn-dusk IMF with respect to the responses of the transpolar potential and the ring current have been the focus of this work. The saturation of the transpolar potential and the lack of ring current response for the dawn-dusk IMF have been shown in chapter 4. The initial conclusions were presented with the proof. Broader conclusions and implications for the space physics community are discussed below. Areas of further research are also reviewed as dictated by the results of the current study.

The transpolar potential saturates for dawn-dusk IMF. It saturates at the same interplanetary electric field strength (IEF) for dawn-dusk IMF as it does for southward IMF. For dawn-dusk IMF, the geoeffective length in the solar wind in the linear regime is the same as for southward IMF, taking into account the projection of the merging field as described by Kan and Lee [1979]. For dawn-dusk IMF, the value at which transpolar potential saturates is approximately half the value at which north-south IMF saturates. For dawn-dusk IMF, if all other conditions are held constant, the region 1 current is approximately half the region 1 current for north-south IMF. Thus, the Region 1 current model (see section 4.1.4) seems unlikely to be the explanation of transpolar potential saturation.

The Magnetosheath Force Balance (MFB) model offers a different explanation of transpolar potential saturation, accounting for the saturation occurring at both the same IEF and the same geoeffective length. By explaining both the linear and non-linear transpolar potential responses in terms of the momentum equation, the MFB model shifts the focus from the ionosphere and field-aligned currents back to the solar wind. In the future, the jump conditions across the bow shock and the effects of turbulence in the magnetosheath will need to be better understood to predict the amount of possible transpolar potential. A better evaluation of the ionospheric conductivity is also needed.

The one-way coupled LFM-CRCM simulation captures the qualitative trends of the ring current in response to the north-south IMF. When the symmetry of the system is broken by adding a dawn-dusk IMF, the LFM-CRCM no longer accurately captures the trends of the ring current. The CRCM assumes symmetric polar region responses and the self-consistent electric fields in the CRCM are calculated on the basis of this symmetry. An understanding of the issues raised by the asymmetry in the polar regions of the ionosphere will require extensive work in the future. Currently, the Rice Convection Model group has been examining parts of this problem, but no solution has been made known to the community at large.

Almost no detectable energy is injected into the ring current for dawn-dusk-dominant IMF. This means almost no inner magnetospheric convection is occurring for dawn-dusk IMF, nor are low PV^γ flux tubes being formed through reconnection in the magnetotail. A study of the topology of the magnetotail during periods of dawn-dusk IMF is needed to better understand this lack of energy injection.

While there is almost no detectable ring current injection, the transpolar potential is still growing and saturating for dawn-dusk IMF. Thus, ionospheric convection and inner magnetospheric convection are no longer coupled. The ionosphere is driven on open field lines. These results have far reaching implications for the space plasma community and the space weather prediction community. Under these conditions, flux circulation is no longer

following the Dungey cycle for dawn-dusk IMF. How the flux is circulating (the cycle of opening the magnetic field through merging with the IMF and the subsequent closing of the magnetic field through reconnection, returning flux to a closed topology) is not yet known. The examination of flux circulation is warrants significant focused effort. Some aspects of that circulation will come to light in examining the geometry of the magnetotail for dawn-dusk IMF.

Finally, it is now known that the magnetosphere interacts differently with north-south IMF and dawn-dusk IMF, but at what values the interactions switch from being primarily north-south IMF and Dungey cycle dominant to being primarily dawn-dusk IMF dominant is unknown. The clock angle is a measure of the angle between the magnetic field of the Earth and the transverse component of IMF. When the clock angle is near 0 or 180 degrees, the IMF is primarily north-south; when the clock angle is near 90 degrees, the IMF is primarily dawn-dusk. A study of the clock angle and the ring current injection rate might provide some insight as to when the flux circulation is Dungey-like and when it is not. This research is currently underway in the Lopez Research Group at the University of Texas at Arlington.

APPENDIX A
LIST OF EVENTS FOR LARGE B_y AND B_z

Table 2. Date, Start Time, and End Time of Large By Events in 1999 and 2000.

Year	Month	Day	Start	End
1999	4	1	1015	1415
1999	4	1	2015	2215
1999	4	21	0600	0645
1999	6	3	0940	1040
1999	6	15	1400	1500
1999	7	6	2025	2105
1999	7	8	0800	0900
1999	8	10	2100	2300
1999	10	21	0030	0220
1999	11	24	0415	0515
1999	11	30	1740	1940
1999	12	3	1900	2100
1999	12	15	1615	1800
1999	12	30	1750	1830
2000	1	11	0700	0755
2000	2	21	1200	1400
2000	3	17	0745	0855
2000	4	19	0015	0130
2000	4	19	1700	1750
2000	5	2	1400	1530
2000	5	12	2115	2300
2000	5	18	2345	0200
2000	5	29	1115	1245
2000	6	5	2315	0020
2000	6	15	0700	0830
2000	7	4	0915	1015
2000	7	4	1100	1200
2000	7	11	0300	0400
2000	7	25	0915	1245
2000	8	1	0200	0300
2000	10	4	0230	0400
2000	10	13	1415	1615
2000	10	22	0930	1100
2000	11	11	1040	1300
2000	11	27	1110	1245
2000	12	27	0745	1130

Table 3. Date, Start Time, and End Time of Large B_y Events in 2001 and First Half of 2002.

Year	Month	Day	Start	End
2001	3	27	0610	0740
2001	4	8	1515	1615
2001	5	3	1935	2200
2001	5	22	2130	2400
2001	5	24	0300	0815
2001	5	28	0015	0130
2001	5	28	0645	0800
2001	6	19	0315	0815
2001	6	19	1155	1340
2001	7	12	0500	0600
2001	8	3	1245	1430
2001	8	27	2200	2300
2001	8	28	0325	0445
2001	9	13	0100	0200
2001	9	30	2307	2342
2001	10	3	0400	0530
2001	11	16	0245	0430
2001	12	16	1215	1815
2001	12	31	0845	1030
2002	2	17	0910	1010
2002	2	20	1750	2040
2002	3	2	1900	2300
2002	3	3	0010	0310
2002	3	24	2245	0145
2002	3	31	1330	1430
2002	5	19	0205	0300
2002	5	23	0515	0630
2002	6	19	0000	0100

Table 4. Date, Start Time, and End Time for Large B_y Events in Second Half of 2002 and 2003.

Year	Month	Day	Start	End
2002	7	16	0915	1030
2002	8	2	1230	1430
2002	8	16	0945	1100
2002	8	19	1630	1730
2002	8	21	1800	2120
2002	8	23	0430	0530
2002	9	21	1045	1200
2002	9	27	1605	1700
2002	9	27	1845	2130
2002	11	17	1300	1500
2002	12	17	1415	2045
2002	12	22	2330	0130
2002	12	25	0700	0900
2003	1	13	1000	1100
2003	1	17	1600	1900
2003	2	13	1115	1530
2003	4	28	2015	2200
2003	5	9	1915	2145
2003	6	15	2100	2345
2003	7	25	2340	0050
2003	7	27	0035	0115
2003	8	5	1945	2200
2003	9	1	1300	1400
2003	9	1	1500	1600
2003	9	8	1745	1900
2003	9	16	2200	2400
2003	10	2	0015	0145
2003	10	2	0220	0320
2003	10	2	1000	1430
2003	10	22	0000	0230
2003	10	25	2000	2300
2003	10	28	0520	0700
2003	12	20	0640	0740

Table 5. Date, Start Time, and End Time for Large B_z Events for 1999 to 2003.

Year	Month	Day	Start	End
1999	2	28	1800	2130
1999	10	22	315	500
2000	1	11	2000	2130
2000	1	22	2300	100
2000	4	6	1750	1825
2000	4	6	2055	2140
2000	7	20	600	1000
2000	8	10	2100	200
2000	8	12	215	300
2000	10	14	600	1000
2000	10	28	2300	2400
2000	10	29	100	200
2001	3	20	1000	1400
2001	4	22	1200	1600
2001	5	9	1100	300
2001	9	30	1545	1645
2001	10	2	1500	2100
2001	11	1	300	1000
2002	2	2	300	745
2002	3	24	400	600
2002	4	18	130	530
2002	4	19	1715	1800
2002	8	20	1800	600
2002	9	4	145	345
2003	3	28	1830	2230
2003	3	29	200	415
2003	3	31	1330	1515
2003	5	10	30	400
2003	6	16	1000	1400
2003	7	11	715	1400
2003	10	14	445	600

REFERENCES

- Axford, W. I., and C. O. Hines (1961), A unifying theory of high-latitude geophysical phenomena and geomagnetic storms, *Can. J. Phys.*, 39, 1433–1464.
- Bochsler, P. (2000), Abundances and charge states of particles in the solar wind, *Rev. Geophys.*, 38(2), 247–266.
- Boris, J. P. (1970), A physically motivated solution of the Alfvén problem, *Technical Report 2167, NRL Memorandum Report*, Naval Research Laboratory, Washington, D.C.
- Borovsky, J. E., M. Hesse, J. Birn, and M. M. Kuznetsova (2008), What determines the reconnection rate at the dayside magnetosphere?, *J. Geophys. Res.*, 113, A07210, doi:10.1029/2007JA012645.
- Boyle, C. B., P. H. Reiff, and M. R. Hairston (1997), Empirical polar cap potentials, *J. Geophys. Res.*, 102(A1), 111–125.
- Burgess, D. (1995), Collisionless shocks, in *Introduction to Space Physics*, edited by M. G. Kivelson and C. T. Russell, pp. 129–163, Cambridge University Press, New York, NY.
- Burke, W. J., D. R. Weimer, and N. C. Maynard (1999), Geoeffective interplanetary scale sizes derived from regression analysis of polar cap potentials, *J. Geophys. Res.*, 104(A5), 9989–9994.
- Burton, R. K., R. L. McPherron, and C. T. Russell (1975), An empirical relationship between interplanetary conditions and Dst, *J. Geophys. Res.*, 80, 4204–4214.
- Courant, R., K. Friedrichs and H. Lewy (1928), Über die partiellen Differentialgleichungen der mathematischen Physik, *Math. Ann.* 100, 32–74. See also the translation, On the partial difference equations of mathematical physics, *IBM J. Res. Develop.* 2 (1967)
- Cowley, S. W. H. (1982), The Causes of Convection in the Earth's Magnetosphere: A Review of Developments During the IMS, *Rev. Geophys.*, 20(3), 531–565.

Crooker, N. U., J. G. Lyon, and J. A. Fedder (1998), MHD model merging with IMF By: Lobe cells, sunward polar cap convection, and overdraped lobes, *J. Geophys. Res.*, 103(A5), 9143-9151.

Daglis, I. A., R. M. Thorne, W. Baumjohann, and S. Orsini (1999), The terrestrial ring current: origin, formation, and decay, *Rev. Geophys.*, 37(4), 407-438.

Dessler, A. J., and E. N. Parker (1959), Hydromagnetic theory of geomagnetic storms, *J. Geophys. Res.*, 24, 2239– 2252.

Dungey, J. W. (1961), Interplanetary Magnetic Field and the Auroral Zones, *Phys. Rev. Lett.*, 6, 47-49.

Ehibara, Y., M.-C. Fok, R. A. Wolf, M. F. Thomsen, and T. E. Moore (2005), Nonlinear impact of plasma sheet density on the storm-time ring current, *J. Geophys. Res.*, 110, A02208, doi:10.1029/2004JA010435

Eriksson, S., W. J. Peria, J. W. Bonnell, Y.-J. Su, R. E. Ergun, Y.-K. Tung, G. K. Parks, and C. W. Carlson (2003), Lobe cell convection and polar cap precipitation, *J. Geophys. Res.*, 108(A5), 1198, doi:10.1029/2002JA009725.

Farris, M., and C. Russell (1994), Determining the standoff distance of the bow shock: mach number dependence and use of models, *J. Geophys. Res.*, 99(A9), 17681-17689.

Fedder, J. A., J.G. Lyon, S. P. Slinker, and C. M. Mobarry (1995a), Topological structure of the magnetotail as a function of interplanetary magnetic field direction, *J. Geophys. Res.*, 100(A3), 3613-3621, doi:10.1029/94JA02577.

Fedder, J. A., S. P. Slinker, J. G. Lyon, and R. D. Elphinstone (1995b), Global numerical simulation of the growth phase and the expansion onset for a substorm observed by Viking, *J. Geophys. Res.*, 100(A10), 19083-19093, doi:10.1029/95JA01524.

Fok, M.-C., R. Wolf, R. Spiro, and T. Moore (2001), Comprehensive computational model of Earth's ring current, *J. Geophys. Res.*, 106(A5), 8417-8424.

Fok, M.-C., T. E. Moore, P. C. Brandt, D. C. Delcourt, S. P. Slinker, and J. A. Fedder (2006), Impulsive enhancements of oxygen ions during substorms, *J. Geophys. Res.*, 111, A10222, doi:10.1029/2006JA011839.

Goldstein, H.(1980), *Classical Mechanics*, Addison-Wesley Publishing Company, Inc., Reading, MA.

Hairston, M. R., T. W. Hill, and R. A. Heelis (2003), Observed saturation of the ionospheric polar cap potential during the 31 March 2001 storm, *Geophys. Res. Lett.*, 30(6), 1325, doi:10.1029/2002GL015894.

Heppner, J. P. (1977), Empirical Models of High-Latitude Electric Fields, *J. Geophys. Res.*, 82(7), 1115–1125.

Hill, T. W. (1994), Theoretical models of polar-cap convection under the influence of a northward interplanetary magnetic field, *J. Atmos. Terr. Phys.*, 56, 185–194.

Hu, Y. Q., Z. Peng, C. Wang, and J. R. Kan (2009), Magnetic merging line and reconnection voltage versus IMF clock angle: Results from global MHD simulations, *J. Geophys. Res.*, 114, A08220, doi:10.1029/2009JA014118.

Hundhausen, A. J. (1995), The Solar Wind, in *Introduction to Space Physics*, edited by M. G. Kivelson and C. T. Russell, pp. 91–128, Cambridge University Press, New York, NY.

Kan, J. R., and L. C. Lee (1979), Energy coupling function and solar wind magnetosphere dynamo, *Geophys. Res. Lett.*, 6, 577–580.

Kivelson, M. G. (1995), Physics of space plasmas, in *Introduction to Space Physics*, edited by M. G. Kivelson and C. T. Russell, pp. 27–57, Cambridge University Press, New York, NY.

Kivelson, M. G., and A. J. Ridley (2008), Saturation of the polar cap potential: Inference from Alfvén wing arguments, *J. Geophys. Res.*, 113, A05214, doi:10.1029/2007JA012302.

Lavraud, B. and J. E. Borovsky (2008), Altered solar wind-magnetosphere interaction at low Mach numbers: Coronal mass ejections, *J. Geophys. Res.*, 113, A00B08, doi:10.1029/2008JA013192.

Lemon, C., R. A. Wolf, T. W. Hill, S. Sazykin, R. W. Spiro, F. R. Toffoletto, J. Birn, and M. Hesse (2004), Magnetic storm ring current injection modeled with the Rice Convection Model and a self-consistent magnetic field, *Geophys. Res. Lett.*, 31, L21801, doi:10.1029/2004GL020914.

Lopez, R. E., M. Wiltberger, S. Hernandez, and J. G. Lyon (2004), Solar wind density control of energy transfer to the magnetosphere, *Geophys. Res. Lett.*, 31, L08804, doi:10.1029/2003GL018780.

Lopez, R. E., J. G. Lyon, E. Mitchell, R. Bruntz, V. G. Merkin, S. Brogl, F. Toffoletto, and M. Wiltberger (2009), Why doesn't the ring current injection rate saturate?, *J. Geophys. Res.*, 114, A02204, doi:10.1029/2008JA013141.

Lopez, R. E., R. J. Bruntz, E. J. Mitchell, M. Wiltberger, and J. G. Lyon (2010), The role of magnetosheath force balance in regulating the dayside reconnection potential, submitted to *J. Geophys. Res.*

Lyon, J. G., J. A. Fedder, and C. M. Mobarry (2004), The Lyon-Fedder-Mobarry (LFM) global MHD magnetospheric simulation code, *J. Atmos. Sol. Terr. Phys.*, 66, 1333-1350, doi:10.1016/j.jastp.2004.03.020.

MacDougall, J. W., and P. T. Jayachandran (2006), Polar cap voltage saturation, *J. Geophys. Res.*, 111, A12306, doi:10.1029/2006JA011741.

Merkin, V. G., A. S. Sharma, K. Papadopoulos, G. Milikh, J. Lyon, and C. Goodrich (2005), Global MHD simulations of the strongly driven magnetosphere: Modeling of the transpolar potential saturation, *J. Geophys. Res.*, 110, A09203, doi:10.1029/2004JA010993.

Mitchell, E. J., R. E. Lopez, R. J. Bruntz, M. J. Wiltberger, J. G. Lyon, R. C. Allen, S. J. Cockrell, and P. L. Whittlesey (2010), Saturation of transpolar potential for large Y-component interplanetary magnetic field, *J. Geophys. Res.*, doi:10.1029/2009JA015119, in press.

Moore, T. E., M.-C. Fok, and M. O. Chandler (2002), The dayside reconnection X line, *J. Geophys. Res.*, 107(A10), 1332, doi:10.1029/2002JA009381.

Newell, P. T., T. Sotirelis, K. Liou, and F. J. Rich (2008), Pairs of solar wind-magnetosphere coupling functions: Combining a merging term with a viscous term works best, *J. Geophys. Res.*, 113, A04218, doi:10.1029/2007JA012825.

Ober, D. M., N. C. Maynard, and W. J. Burke (2003), Testing the Hill model of transpolar potential saturation, *J. Geophys. Res.*, 108(A12), 1467, doi:10.1029/2003JA010154.

O'Brien, T. P., and R. L. McPherron (2000), An empirical phase space analysis of ring current dynamics: Solar wind control of injection and decay, *J. Geophys. Res.*, 105(A4), 7707–7720.

Parker, E. N. (1958), Dynamics of the interplanetary gas and magnetic fields, *Astrophys. J.*, 128, 664-676.

Priest, E. R. (1995), The Sun and Its Magnetohydrodynamics, in *Introduction to Space Physics*, edited by M. G. Kivelson and C. T. Russell, pp. 58-90, Cambridge University Press, New York, NY.

Reiff, P. H., and J. G. Luhmann (1986), Solar wind control of the polar-cap voltage, in *Solar Wind-Magnetosphere Coupling*, edited by Y. Kamide and J. A. Slavin, pp. 453-476, Terra Sci., Tokyo.

Reiff, P. H., R. W. Spiro, and T. W. Hill (1981), Dependence of Polar Cap Potential Drop on Interplanetary Parameters, *J. Geophys. Res.*, 86(A9), 7639–7648.

Richmond, A., and Y. Kamide (1988), Mapping electrodynamic features of the high-latitude ionosphere from localized observations: technique, *J. Geophys. Res.*, 93(A6), 5741-5759.

Ridley, A. J. (2007), Alfvén wings at Earth's magnetosphere under strong interplanetary magnetic field, *Ann. Geophys.*, 25, 533-542.

Russell, C. T., J. G. Luhmann, and G. Lu (2001), Nonlinear response of the polar ionosphere to large values of the interplanetary electric field, *J. Geophys. Res.*, 106(A9), 18,495–18,504.

Sckopke, N. (1966), A general relation between the energy of trapped particles and the disturbance field near the Earth, *J. Geophys. Res.*, 71, 3125–3130.

Shue, J.-H., J. Chao, H. Fu, C. Russell, P. Song, K. Khurana, and H. Singer (1997), A new functional form to study the solar wind control of the magnetopause size and shape, *J. Geophys. Res.*, 102(A5), 9497-9511.

Sibeck, D. G., R. E. Lopez, and E. C. Roelof (1991), Solar Wind Control of the Magnetopause Shape, Location, and Motion, *J. Geophys. Res.*, 96(A4), 5489–5495.

Siscoe, G. L., G. M. Erickson, B. U. Ö. Sonnerup, N. C. Maynard, J. A. Schoendorf, K. D. Siebert, D. R. Weimer, W. W. White, and G. R. Wilson (2002a), Hill model of transpolar potential saturation: Comparisons with MHD simulations, *J. Geophys. Res.*, 107(A6), 1075, doi:10.1029/2001JA000109.

Siscoe, G. L., N. U. Crooker, and K. D. Siebert (2002b), Transpolar potential saturation: Roles of region 1 current system and solar wind ram pressure, *J. Geophys. Res.*, 107(A10), 1321, doi:10.1029/2001JA009176.

Siscoe, G., J. Raeder, and A. J. Ridley (2004), Transpolar potential saturation models compared, *J. Geophys. Res.*, 109, A09203, doi:10.1029/2003JA010318.

Sonnerup, B. U. Ö., K. D. Siebert, W. W. White, D. R. Weimer, N. C. Maynard, J. A. Schoendorf, G. R. Wilson, G. L. Siscoe, and G. M. Erickson (2001), Simulations of the magnetosphere for zero interplanetary magnetic field: The ground state, *J. Geophys. Res.*, 106(A12), 29,419–29,434.

Thomsen, M. F., J. E. Borovsky, D. J. McComas, R. C. Elphic, and S. Maurice (1998), The magnetospheric response to the CME passage of January 10–11, 1997, as seen at geosynchronous orbit, *Geophys. Res. Lett.*, 25(14), 2545–2548.

Walker, R. J. and C. T. Russell (1995), Solar-wind interactions with magnetized planets, in *Introduction to Space Physics*, edited by M. G. Kivelson and C. T. Russell, pp. 164–182, Cambridge University Press, New York, NY.

Wiltberger, M. J., R. S. Weigel, M. Gehmeyr, and T. Guild (2005), Analysis and visualization of space science model output and data with CISIM-DX, *J. Geophys. Res.*, 110, A09224, doi:10.1029/2004JA010956.

Yee, K. S. (1966), Numerical solution of initial boundary value problems involving Maxwell's equations in isotropic media, *IEEE Transactions on Antennas and Propagation* 14, pp. 302–307.

Zhou, X.-Y., et al., Ring current intensification and convection-driven negative bays: Multisatellite studies, *J. Geophys. Res.*, 108(A11), 1407, doi:10.1029/2003JA009881, 2003.

BIOGRAPHICAL STATEMENT

Elizabeth J. Mitchell graduated high school in 1995 and began to attend Northern Virginia Community College (NVCC). In the spring of 1999, Elizabeth received her Associates of Applied Science in Paramedic Studies from NVCC and continued to work in the medical field in both Virginia and Texas until December 2002.

From September 2001 to May 2005, Elizabeth attended the University of Texas at El Paso (UTEP) for a Bachelors of Science in Physics. Elizabeth did undergraduate research from January 2003 to May 2005 under the guidance of Niescja Turner in space physics, and received funding from the Minority Access to Research Centers (MARC) program. Elizabeth wrote and defended an undergraduate thesis entitled, "Magnetospheric responses to high speed stream-driven and magnetic cloud-driven storms."

From July 2005 to August 2007, Elizabeth attended Florida Institute of Technology (FL Tech) for a Masters of Science in Space Physics. Elizabeth worked under the guidance of Niescja Turner on "The roles of Corotating Interaction Regions, Coronal Mass Ejections, and Shocks in the Transfer of Energy within the Earth's Inner Magnetosphere and Ionosphere During Geomagnetic Storms.". During the fall of 2006, Elizabeth's research was funded by the Integrated Science Teaching Enhancement Partnership (InSTEP) GK-12 Program, where she wrote science curriculum for high school science classes as well as doing her research.

From August 2007 to May 2010, Elizabeth attended the University of Texas at Arlington (UTA) for a Doctorate of Philosophy in Physics. Under the guidance of Ramon E. Lopez, Elizabeth has worked on several different research projects and mentored 6 undergraduates. During her tenor at UTA, Elizabeth has been funded by both the NSF and NASA. Initially a graduate student under NSF STC Center for Integrated Space Weather Modeling (CISM),

Elizabeth wrote and received a NASA GSRP proposal for the 2008-2009 and 2009-2010 school years.

The research preformed by Elizabeth and other members of the Ramon Lopez Research Group has provided Elizabeth with a published co-authored paper ("Why doesn't the ring current injection rate saturate?"), a first authored paper in press ("Saturation of transpolar potential for large Y-component interplanetary magnetic field"), a co-authored paper under review ("The role of magnetosheath force balance in regulating the dayside reconnection potential"), and enough completed research to write at least 3 more papers. Elizabeth defended her dissertation, entitled "The role of the Y-component of the interplanetary magnetic field in transpolar potential saturation and ring current response as found in data and simulation", on April 19, 2010.

After graduation, Elizabeth would like to work at NASA Goddard Space Flight Center, examining the topology of the magnetotail under different orientations of the interplanetary magnetic field.